Title
High-Resolution Localization of Aeroacoustic Sources Using Advanced Phased Array Setups

Author
Morata Carranza, David

Publication Date
2022

UNIVERSITY OF CALIFORNIA,
IRVINE

High-Resolution Localization of Aeroacoustic Sources Using Advanced Phased Array Setups

DISSERTATION

submitted in partial satisfaction of the requirements
for the degree of

DOCTOR OF PHILOSOPHY

in Mechanical and Aerospace Engineering

by

David Morata Carranza

Dissertation Committee:
Professor Dimitri Papamoschou, Chair
Professor Jacqueline Huynh
Professor Perry Johnson

2022

DEDICATION

To my wife, Shail. Always together through the thick and thin.

TABLE OF CONTENTS

Page

LIST OF FIGURES **v**

LIST OF TABLES **x**

ACKNOWLEDGMENTS **xi**

VITA **xii**

ABSTRACT OF THE DISSERTATION **xiv**

1 Introduction **1**
- 1.1 Background and Motivation 1
- 1.2 Review of Jet Noise 7
  - 1.2.1 Principal Components of Jet Noise 8
  - 1.2.2 The Sources of Jet Noise 14
  - 1.2.3 Waves in Supersonic Jets 18
- 1.3 Research Goals 20

2 Beamforming **24**
- 2.1 Model for the Acoustic Source 25
- 2.2 Time Domain Beamforming 27
- 2.3 Frequency Domain Beamforming 28
- 2.4 Microphone Array Performance: the Point Spread Function 31
- 2.5 Continuous-Scan Beamforming 34
  - 2.5.1 Signal Division 35
  - 2.5.2 Signal Non-Stationarity 37
  - 2.5.3 Beamforming using Cross-Spectral Submatrices 44
  - 2.5.4 Matrix Completion Techniques 49
  - 2.5.5 Partial Fields Decomposition 62
- 2.6 Summary of the Continuous-Scan Techniques 67
- 2.7 Deconvolution Methods 69
  - 2.7.1 DAMAS 69
  - 2.7.2 CLEAN-SC 72
  - 2.7.3 Richardson-Lucy 75

3 Signal Processing for Continuous-Scan Microphone Arrays 77
3.1 Upper Bound on Block Size 79
3.2 Minimum Block Size 81
3.3 Maximum block size 83
3.4 Number of blocks and overlap 87
3.5 Optimal signal segmentation 88

4 Experimental Program 90
4.1 Anechoic Facility and Microphone Array 91
4.2 Noise Sources 93
  4.2.1 Impinging Jets Source 93
  4.2.2 Subsonic Jet 94
  4.2.3 Supersonic Jet 95
4.3 Signal division and Array Layouts 96
4.4 Tracking and Synchronization of the Scanning Sensor 98

5 Results 102
5.1 Expected Performance of the Beamforming Methods 103
  5.1.1 Effect of the Signal Processing 107
5.2 Impinging Jets Source 110
  5.2.1 Sound Pressure Level 110
  5.2.2 Noise Source Distribution 111
5.3 Subsonic Jet Flow 117
  5.3.1 Isolated Subsonic Jet 118
  5.3.2 Subsonic Jet with Installation Effects 123
5.4 Supersonic Jet Flow 127
  5.4.1 Isolated Supersonic Jet 128
  5.4.2 Supersonic Jet with an Upstream Reflector 143

6 Conclusions and Future Considerations 153
6.1 Conclusions 153
6.2 Future Considerations 157

Bibliography 160

LIST OF FIGURES

Page

1.1 Sketch of a convergent nozzle and a far-field observer. 9
1.2 Spark Schlieren image of an overexpanded jet. Extracted from Ref. [1]. . . . 9
1.3 Schematic representation of the screech loop process, with the four stages involved. 10
1.4 Normalized screech wavelength as a function of the fully-expanded jet Mach number of underexpanded round supersonic jets, extracted from Tam *et al.* [2] 12
1.5 Schilieren photographs of the convergent circular jets oscillating in mode A1, A2 (symmetrics), B (lateral) and C (helical). Figure extracted from Umeda and Ishii [3]. 13
1.6 Far-field supersonic jet noise SPL spectrum of an imperfectly-expanded jet experiment performed at UCI. The microphone was located at a polar angle of 70.65°. 14
1.7 Schematic of the different waves supported by a compressible vortex sheet model. Extracted from Ref. [4] 19
1.8 Pressure eigenfunction for the upstream-traveling acoustic modes (k_{TH^-}) of mode (m,n)=(azimuthal,radial) for a jet with $M_j = 1.5$, obtained using a compressible vortex sheet model. Extracted from Ref. [4] 21

2.1 Schematic of a noise source and a microphone array. 25
2.2 Far-field microphone array and the one-dimensional model of the jet noise source. 27
2.3 schematic of a CSM for a generic acoustic experiment that involves three fixed microphones. 30
2.4 Image of the lunar surface. Image affected by the point spread function (left) and real image (right). Image extracted from Ref. [5]. 33
2.5 Illustration of the division of the signal into K quasi-stationary blocks without block overlap. 37
2.6 Line source distribution and far-field microphone array containing fixed microphones and one scanning sensor. 38
2.7 Frequency-dependent windows. (a) Gaussian; (b) Cauchy distribution; and (c) Hyperbolic secant. 43
2.8 Schematic of the Gaussian window width reduction with increasing frequency. 44
2.9 Illustration of the CSSMs for two scanning sensors (1-2) and 5 fixed sensors (3-7). Non-repeated elements are indicated in bold font. 47

2.10 (a) Cross-spectral matrix for an array with three fixed microphones and one scanning sensor whose output is divided into six blocks. The correlations involving fixed sensors only are highlighted in blue, while those involving fixed and scanning sensors are indicated in red. Blank entries indicate missing elements. (b) Submatrix for block 0. (c) Submatrix for block 1. 50
2.11 Wrapped and unwrapped phased between cross-spectral densities of microphones with spacings of (a) 0.06 m and (b) 0.22 m. 52
2.12 Schematic of a data-missing CSM within the continuous-scan paradigm; 3 microphones are fixed and the signal from one scanning sensor is divided into 6 blocks. 55
2.13 Schematic of a completed CSM within the continuous-scan paradigm; 3 microphones are fixed and the signal from one scanning sensor is divided into 6 blocks. 60
2.14 Schematic of the decomposition of the acoustic field emitted by a jet noise source into a partial field on the hologram surface. 63
2.15 Schematic representation involved in the partial field decomposition technique for an array containing 3 fixed sensors and one scanning sensor. Blocks displayed are $k = 1$, 3, and 5. 64

3.1 Distance and angle variations associated with the length of a signal block. . . 79
3.2 ΔSPL computed with consecutive segment increases as a function of the number of segments for $N_{\mathrm{FFT}} = 1024$ for distinct acoustic sources: (a) Impinging jets source; and (b) subsonic jet. 84
3.3 Example of the frequency-dependent Gaussian window (red) and resulting filtering of signal (black). (a) $f = 10$ kHz; (b) $f = 90$ kHz. 85
3.4 Segmentation of signal within a block and Gaussian window at given frequency. 85
3.5 Trends governing the determination of optimal block size. (a) Block-size bounds versus N_{FFT}; (b) N_{FFT} relation with frequency; (c) Block-size bounds and Gaussian window width (in samples) versus frequency. Green regions indicate the allowed block size. 89

4.1 Anechoic chamber and qualitative deployment of the microphones. 91
4.2 Design of the linear traverse system. 92
4.3 Fixed and scanning microphones at their closest spacing of 6 mm, measured from the cartridge centers. 93
4.4 Impinging jets source. 94
4.5 Schematic of convergent nozzle integrated with plate used in the subsonic jet experiments. 95
4.6 Nozzle coordinates on symmetry plane. 96
4.7 Photographs of the nozzle and the reflectors. (a) 90°; and (b) 60°. 96
4.8 Coordinates of array layout P (a) and S (b). Fixed microphones indicated in black and scanned region indicated in red. 98
4.9 Example of the synchronization of the microphone traces with the position. (a) Pressure signal; (b) Synchronization signal. 100
4.10 Scanning microphone trajectory comparison for a given experiment. 101

5.1 Main lobe beamwidth for array layouts S and P. 105
5.2 Normalized point spread function at $x = 0$ for the frequency range of interest obtained using the optimized block schedule. (a) FS; (b) CSSM; (c) CSMC; and (d) PFD. 105
5.3 Normalized point spread function at $x = 0$ at 15 kHz. 106
5.4 Normalized point spread function at $x = 0$ at 50 kHz. 106
5.5 Normalized point spread function at $x = 0$ at 85 kHz for FS, CSSM, CSMC and PFD. 107
5.6 Normalized point spread function at $x = 0$ at 15 kHz with $\mathrm{CS}_{K=120}$. 108
5.7 Normalized point spread function at $x = 0$ at 50 kHz with $\mathrm{CS}_{K=120}$. 108
5.8 Normalized point spread function at $x = 0$ at 85 kHz with $\mathrm{CS}_{K=120}$ for FS, CSSM, CSMC and PFD. 109
5.9 SPL spectra for the impinging jets source at polar angles $\theta =$ (a) 23.5°; (b) 39.7°; and (c) 82.6°. 110
5.10 DAS noise source maps of the IJS obtained using different methods. (a) FS; (b) CSSM; (c) CSMC; and (d) PFD. 112
5.11 Normalized source distribution obtained with DAS at several frequencies: (a) 15 kHz; (b) 50 kHz; and (c) 85 kHz. 113
5.12 Ranked odd singular values (1, 3, 5, etc.) for the IJS. 114
5.13 Deconvolved DAS noise source maps of the IJS obtained with FS using (a) DAMAS; (b) CLEAN-SC; and (c) R-L. 115
5.14 Deconvolved DAS noise source maps of the IJS obtained with CSMC using (a) DAMAS; (b) CLEAN-SC; and (c) R-L. 115
5.15 Deconvolved DAS noise source maps of the IJS obtained with PFD using (a) DAMAS; (b) CLEAN-SC; and (c) R-L. 116
5.16 Normalized source distribution obtained with PFD and the distinct deconvolution algorithms at several frequencies: (a) 15 kHz; (b) 50 kHz; and (c) 85 kHz. 117
5.17 SPL spectra for the isolated jet at various polar angles. (a) $\theta = 23.94°$; (b) $\theta = 41.35°$; (c) $\theta = 87.28°$; and (d) $\theta = 117.52°$. 118
5.18 DAS noise source maps of the isolated subsonic jet obtained using different methods. (a) FS; (b) CSSM; (c) CSMC; and (d) PFD. 120
5.19 Location of the peak noise source for the isolated jet. 121
5.20 Deconvolved noise source maps of the isolated jet obtained with PFD using (a) DAMAS; (b) CLEAN-SC; and (c) R-L. 122
5.21 Ranked odd singular values (1, 3, 5, etc.) for the isolated subsonic jet. 122
5.22 Real part of the complex coherence in the acoustic far-field for two frequencies using PFD and CSMC (in red), and using the raw data (in black). 124
5.23 SPL spectra for the isolated (black lines) and with the shield at different positions. Blue: $L = 2D$; Red: $L = 5D$; and Green: $L = 8D$. (a) $\theta = 23.94°$; (b) $\theta = 41.35°$; (c) $\theta = 87.28°$; and (d) $\theta = 117.52°$. 125
5.24 DAS noise source maps of the isolated jet and the shielding configuration obtained using PFD. (a) Isolated; (b) $L = 2D$; (c) $L = 5D$; and (d) $L = 8D$. 126
5.25 Location of the peak noise source for the isolated jet and the shielding configurations. 127

5.26 SPL spectra for the underexpanded jet at $M_j = 1.18$ various polar angles. (a) $\theta = 62.1°$; and (b) $\theta = 97.8°$. 129
5.27 SPL spectra for the underexpanded jet at $M_j = 1.22$ various polar angles. (a) $\theta = 62.1°$; and (b) $\theta = 97.8°$. 129
5.28 SPL spectra for the underexpanded jet at $M_j = 1.26$ various polar angles. (a) $\theta = 62.1°$; and (b) $\theta = 97.8°$. 130
5.29 SPL spectra for the underexpanded jet at $M_j = 1.30$ various polar angles. (a) $\theta = 62.1°$; and (b) $\theta = 97.8°$. 130
5.30 SPL spectra for the underexpanded jet at $M_j = 1.33$ various polar angles. (a) $\theta = 62.1°$; and (b) $\theta = 97.8°$. 130
5.31 SPL spectra for the underexpanded jet at $M_j = 1.34$ various polar angles. (a) $\theta = 62.1°$; and (b) $\theta = 97.8°$. 131
5.32 SPL spectra for the underexpanded jet at $M_j = 1.36$ various polar angles. (a) $\theta = 62.1°$; and (b) $\theta = 97.8°$. 131
5.33 SPL spectra for the underexpanded jet at $M_j = 1.40$ various polar angles. (a) $\theta = 62.1°$; and (b) $\theta = 97.8°$. 131
5.34 SPL spectra for the underexpanded jet at $M_j = 1.43$ various polar angles. (a) $\theta = 62.1°$; and (b) $\theta = 97.8°$. 132
5.35 SPL spectra for the underexpanded jet at various polar angles. (a) $\theta = 62.1°$; (b) $\theta = 69.1°$; (c) $\theta = 83.8°$; and (d) $\theta = 97.8°$. 133
5.36 Directivity of SPL for the isolated supersonic jet. 134
5.37 DAS noise source maps of the isolated supersonic jet obtained using different methods. (a) FS; (b) CSSM; (c) CSMC; (d) PFD. 135
5.38 Ranked odd-numbered singular values from matrix $\mathbf{\Sigma}_{ff,T}$ for the isolated supersonic jet. Highest to lowest singular value plots are shown from top to bottom. 137
5.39 Real part of the complex coherence in the acoustic far-field for tones $B^{(1)}$ and $B^{(2)}$ using PF decomposition and CSMC (in red), and using the raw data (in black). 138
5.40 Deconvolved noise source maps of the supersonic jet flow obtained with PFD using different algorithms: (a) DAMAS; (b) CLEAN-SC; (c) R-L. 139
5.41 Detail of the shock cell pattern around tone $B^{(4)}$ obtained through deconvolution of the PFD (left column) and CSMC (right column) using R-L (first row), DAMAS (second row) and CLEAN-SC (third row). 140
5.42 SPL spectra for the underexpanded jet with the 90° reflector at various polar angles. (a) $\theta = 62.1°$; (b) $\theta = 69.1°$; (c) $\theta = 83.8°$; and (d) $\theta = 97.8°$. 145
5.43 SPL spectra for the underexpanded jet with the 60° reflector at various polar angles. (a) $\theta = 62.1°$; (b) $\theta = 69.1°$; (c) $\theta = 83.8°$; and (d) $\theta = 97.8°$. 146
5.44 Directivity of SPL for the supersonic jet with the 90° reflector. 147
5.45 Directivity of SPL for the supersonic jet with the 60° reflector. 147
5.46 Deconvolved noise source maps of the supersonic jet flow with the 60° reflector obtained with PFD using different algorithms: (a) DAMAS; (b) CLEAN-SC; and (c) R-L. 150

5.47 Detail of the shock cell pattern around tone $B^{(4)}$ for the 60° reflector case obtained through deconvolution of the PFD (left column) and CSMC (right column) using R-L (first row), DAMAS (second row) and CLEAN-SC (third row). 152

LIST OF TABLES

Page

2.1 Expressions for the frequency-dependent windows. 42
2.2 Summary of the beamforming methods utilized. 68

4.1 Block division for continuous-scan method (CSV). 97
4.2 Array layouts P and S. 98

5.1 Array geometric constants. 104

ACKNOWLEDGMENTS

I would like to start by thanking my Ph.D. advisor, Professor Dimitri Papamoschou, for his mentorship, support, and patience. The present research work was only possible due to his guidance and I could not wish for a better Ph.D. advisor. We have spent many hours together performing experiments and discussing our research approaches, and I have enjoyed and learned in every step of the way.

Secondly, I would like to thank my wife and soulmate, Shail, who has been there for me in the ups and downs, and has always been the reason for my happiness on many rainy days. This work has been possible thanks to her encouragement, support and love. I would also like to thank my parents, Cori and Sisco, and my brother Pau, who have given me the strength to keep pursuing my goals through our infinite number of FaceTime calls. Also, Pareshkumar, Sonalben, and Shardul accepted me as another family member and gave me an indescribable feeling of comfort and belonging that was much needed after long work hours. To them I also wish to express my most sincere grateful words.

I want to thank my California friends: Andres, Irene, Jordi, Marina, Kristen, Miquel, Ana, Marc, Mireia, Clara, Efren, Gerard, and Kyle, for their support through the Ph.D. and the many hours we have spent enjoying outdoors and discussing everything one could possibly imagine. They have made my Ph.D. journey more fun and happy.

I am especially grateful to Prof. Roger Rangel, Pete Balsells and the Balsells Foundation. They gave me the opportunity to pursue my graduate studies at UCI in 2017. I would not be able to be here without their support.

I also want to express my gratitude to my thesis committee members Prof. Jacqueline Huynh and Prof. Perry Johnson.

A special thank you note goes to the co-authors of the publications in which I have participated during these years: Prof. Dimitri Papamoschou, and Dr. Parthiv Shah.

Lastly, I would like to acknowledge the support of the NASA Small Business Innovation and Research (SBIR) program and ATA for funding part of this work, with funding contract numbers 80NSSC20C0089, NNX16CC79P, and NNX17CC18C.

VITA

David Morata Carranza

EDUCATION

Ph.D. in Mechanical and Aerospace Engineering **2022**
University of California, Irvine *Irvine, California*

M.S. in Mechanical and Aerospace Engineering **2019**
University of California, Irvine *Irvine, California*

B.S. in Aerospace Engineering **2017**
Universitat Politecnica de Catalunya *Terrassa, Spain*

RESEARCH EXPERIENCE

Graduate Student Researcher **2017–2022**
University of California, Irvine *Irvine, California*

TEACHING EXPERIENCE

University of California, Irvine
Teaching Assistant for MAE 91 **2019**

Teaching Assistant for MAE 130B **2019**

EDITORIAL EXPERIENCE

Guest Editor **2022**
Noise and Vibration Worldwide

Guest Editor **2022**
International Journal of Aeroacoustics

HONORS AND AWARDS

2022 AIAA/CEAS Aeroacoustics Best Paper Award **2022**
American Institute of Aeronautics and Astronautics

Orville and Wilbur Wright Graduate Award **2019**
American Institute of Aeronautics and Astronautics

Balsells Fellowship **2017**
The Balsells Foundation

REVIEWING EXPERIENCE

Applied Acoustics
Aerospace Science and Technology
Journal of the Acoustical Society of America
International Journal of Aeroacoustics
Journal of Propulsion and Power
Mechanical Systems and Signal Processing
Journal of Vibration and Acoustics
Noise and Vibration Worldwide
Journal of Heat Transfer
Experimental Thermal and Fluid Science
Journal of Low Frequency Noise, Vibration and Active Control

CONFERENCE CHAIRING

AIAA SciTech Forum and Exposition (San Diego, CA) **2022**
Jet Noise session co-chair

REFEREED JOURNAL PUBLICATIONS

Optimized Signal Processing for Continuous-Scan Phased Microphone Arrays (under review) **2022**
Journal of Sound and Vibration

High-Resolution Continuous-Scan Beamforming (under review) **2022**
AIAA Journal

REFEREED CONFERENCE PUBLICATIONS

Extension of Traditional Beamforming Methods to the Continuous-Scan Paradigm **Jan 2022**
2022 AIAA SciTech Forum and Exposition

Effect of Nozzle Geometry on the Space-Time Emission of Screech Tones **Aug 2021**
2021 AIAA Aviation Forum and Exposition

Advances in the Direct Spectral Estimation Methods of Aeroacoustics Sources Using Continuous-Scan Phased Arrays **Jan 2021**
2021 AIAA SciTech Forum and Exposition

ABSTRACT OF THE DISSERTATION

High-Resolution Localization of Aeroacoustic Sources Using Advanced Phased Array Setups

By

David Morata Carranza

Doctor of Philosophy in Mechanical and Aerospace Engineering

University of California, Irvine, 2022

Professor Dimitri Papamoschou, Chair

This work aims at improving the current state-of-the-art in noise source localization techniques and phased array technologies by extending and adapting distinct traditional beamforming and deconvolution techniques to microphone phased arrays that contain continuously-scanning sensors. The continuous-scan approach is capable to attain a high-resolution noise source localization, which is of utmost importance when analyzing certain aeroacoustic sources. Care must be taken when handling the microphone signals from continuously-scanning sensors as these are non-stationary due to the traversing of a spatially-varying acoustic field. Quasi-stationarity is sought by dividing the signals into smaller, quasi-stationary blocks and by applying a frequency-dependent window within each block. The motion of the sensors also requires modification of the steering vectors used in beamforming to include a Doppler-shifted frequency. Optimal block schedules versus frequency are proposed and demonstrated to exploit the benefits of the continuous-scan paradigm by enhancing the spatial resolution of the images while containing the computational cost. Beamforming is carried out using three distinct approaches: application of the classical delay-and-sum technique to the cross-spectral matrix obtained for each blocks, followed by assembly of non-repeated elements of each block; a cross-spectral matrix completion process; and a partial fields decomposition method. The last two approaches result in a unified cross-spectral matrix that enables deconvolution of the array output and the use of advanced beamforming approaches such as orthogonal or functional beamforming. This work features three deconvolution approaches: DAMAS, Clean-SC, and the Richardson-Lucy method. All the beamforming and deconvolution methods are applied in conjunction with the proposed signal processing to the acoustic fields emitted by an impinging-jets source, a subsonic turbulent jet in isolation and integrated with a shielding plate, and a supersonic jet in isolation and with upstream reflector surfaces. Introduction of a single scanning sensor to a far-field array improves dramatically the fidelity of beamforming. The deconvolved images further improve the spatial resolution. The point spread function and the impinging jets source are used to assess the performance of all the techniques. The source distributions obtained with the continuous-scan approaches are compared to those obtained utilizing an array containing fixed sensors only. The techniques are then used to predict the effect of a shielding plate on the subsonic turbulent jet, and discern the location of the peak noise source as a function of frequency. The methods are also applied to the imaging of the supersonic flow issuing from a convergent nozzle that presented the screech phenomenon. The jet oscillated in well-known mode B (lateral). The continuous-scan paradigm is capable of obtaining the location of the screech sources and determination of the fine shock-cell structure of the supersonic jet flow from far-field microphone measurements only, underscoring its potential. Addition of conical reflector surfaces to the supersonic jet gave rise to a new mode E, with tonal components that do not fall into any known category (mode A1, A2, B or C). The source distribution of mode E and mode B is analyzed.

Chapter 1

Introduction

1.1 Background and Motivation

The issue of noise source localization has engaged the research community over the past 8 decades. Noise source localization tools are essential techniques that are used to understand, characterize and model certain acoustic sources of interest. These tools are used in a myriad of fields, finding applications within the automotive industry, high-speed rail, or the aerospace industry, to name a few. Within the aerospace segment, noise source localization techniques are used to describe complex flow patterns such as those associated with subsonic and supersonic turbulent jets or ducted fans. Microphone array techniques are also utilized to predict other phenomena such as noise emanating from propulsion-airframe interactions in blended wing body configurations, or from landing gear or lifting surfaces take-off and landing aircraft procedures, thus becoming critical tools for noise assessment and aircraft certification. Given the complicated nature of the aeroacoustic sources typically found in the context of the aviation industry, high-resolution source localization methods are required to detect and minimize noise sources. The recent years have seen a significant boost on new microphone array techniques aiming to improve the limitation on the spatial resolution that one encounters when using traditional setups and noise source localization techniques. Improvement of the current experimental methodologies, including its applications to describe aeroacoustic sources of interest, poses a complex challenge that must be tackled using novel experimental setups and tailored signal processing techniques. The following paragraphs will briefly describe the history of noise source localization techniques, provide a literature review and an overview of the state-of-the-art, and introduce the reader to the high-resolution beamforming approach developed in this work.

The science and the experimental tools used in noise source localization studies have progressed significantly over the past decades. In the early days, a passive device known as *acoustic telescope* was used. A prominent example of its utilization is found during the World War II, where soldiers used acoustic antennas to localize approaching aircraft by analyzing their far-field noise imprints. This device consisted of a parabolic mirror that redirected and "collimated" acoustic waves to a focal point, increasing the signal to noise ratio significantly, and allowing the detection of aircraft from significantly far distances. This rudimentary setup might be considered the inception of modern noise source localization tools.

These early noise source localization techniques did not allow a high degree of flexibility or a proper quantification or description of the noise sources. As such, significant efforts were invested into developing more sophisticated experimental setups and signal processing tools. The introduction of phased microphone arrays and the modern computer enabled an unprecedented spatial resolution that allowed for an accurate characterization of aeroacoustic sources compared to the use of acoustic mirrors. An example of a pioneering work that utilized microphone techniques is found in the seminal study of Fisher *et al.* [6], which is considered to be one of the first references on the polar correlation technique, published during the 1970s. The authors introduced a new method to localize noise sources that was based on far-field microphone recordings that were distributed over a polar arc centered on the nozzle jet axis (i.e., a phased microphone array). The use of cross-correlations and cross-spectral densities between all the distinct microphones was the essence of the method, allowing very important contributions within the field of aeroacoustics. The technique proved to yield significant improvements to the noise localization process, and the authors were able to disseminate the space-frequency distribution of the main sources of jet noise. Their pioneering work set the foundations for modern and more advanced source localization techniques.

The National Aeronautics and Space Administration (NASA) ambitious noise reduction goals for commercial aviation, introduced during the 1980s and the 1990s, proved to be a significant tailwind for the development of advanced experimental noise localization techniques, which helped researchers understand the main systems contributing to aircraft noise during take-off and landing: the propulsion devices, the landing gear, and the lifting surfaces. Computer-aided simulations were performed in conjunction; however, the computational power required for large high-fidelity simulations was still lacking and tools for computational aeroacoustics (CAA) could still not handle complicated geometries. Microphone phased arrays were broadly adopted during the 1990s, and have become an industry standard for noise source localization studies. The works of Mosher [7] and Humphreys *et al.* [8] are two examples of how microphone phased arrays could be used for localizing and describing aeroacoustic sources of interest in a laboratory scale.

During the 1990s and 2000s, the delay-and-sum (DAS) beamforming algorithm was widely adopted by the aeroacoustics research community. The technique has become a prevalent tool to process microphone data from simultaneously-sampled sensors nowadays, and remains widely used. In this approach, each individual microphone can be electronically “steered” to a region of interest, where significant acoustic sources are expected, by adding time delays that are dependent on the relative position between the source and the microphone. The signals are then summed and normalized and an array response can be obtained for each point of interest. The steering approach involved in the DAS process forms a focused beam (the reason behind its name) to a point of interest to detect if there exists a noise source. The algorithm was quickly adapted to the frequency domain by making use of the Fourier transform, which allowed to characterize noise sources in the space-frequency domain. The utilization of DAS in conjunction with phased microphone arrays was a breakthrough compared to the use of the early acoustic mirrors given that one did not need to physically move the array to focus it on user-defined spatial locations, and the exact frequency and amplitude of the sources could be quantified.

However, one of the main drawbacks of DAS, and in general, traditional phased array techniques, relied on the Point Spread Function (PSF). The PSF models the response of the microphone array to a point source. Given that there is a limit in the number of microphones that can be used for an experiment, the microphone array usually creates artificial sources, resulting in a blurred noise source localization and a penalization of the spatial resolution that is required in many applications. The shape of the PSF is highly dependent on frequency, the focus point, and the array geometry. The shape and width of the main beam are also governed by the geometry of the phased array. In most practical applications, the main beam or lobe, is accompanied by secondary beams (sidelobes), with the latter being prominent at high frequency in many instances. The output of the DAS process is the convolution of the real source distribution and the array PSF. As such, the point spread function might greatly influence the source distribution obtained with DAS and traditional phased arrays. Mitigation of the effects of the PSF is a current topic of research [9, 10, 11]. This blurring effect of the PSF is excellently described by Brooks and Humpreys [12]: "*Traditional presentations of array results involve mapping (contour plotting) of array output over spatial regions. These maps do not truly represent noise source distributions, but ones that are convolved with the array response functions, which depend on array geometry, size (with respect to source position and distributions), and frequency.*". Reduction of the effect of the sidelobes implies reducing the spacings between the microphones, incurring into significant monetary and processing costs, which is deemed impractical in most the application.

Several deconvolution techniques have been developed since the 1970s. These methods aim at separating the contribution from the PSF from the measured DAS source distribution in order to obtain the *real* source distribution. Examples of these methods are the DAMAS [12] (Brooks and Humphreys), DAMAS2 and DAMAS3 [13] (Dougherty), CLEAN-SC [14] (Sijtsma) or the Richardson-Lucy approach [15, 16], to name a few. Other techniques, known as Spectral Estimation Methods (SEM), have also been developed to increase the spatial resolution of the beamformer output. These methods obviate the "steering" approach of the DAS and instead estimate the source distribution by minimizing the difference between the modeled and the measured pressure statistics [17]. SEM and deconvolution methods usually assume an uncorrelated monopole nature about the acoustic source. The inversion of the acoustic problem found in SEM methods can be performed by means of the conjugate gradient minimization of Shanno and Phua [18] or using a Bayesian-based approach [17, 1, 19, 20]. The direct estimation approach has been shown to provide results of higher quality than some deconvolution approaches in the imaging of turbulent jets [1, 17]. However, SEM techniques or deconvolution of the array output can only improve the spatial resolution of the noise source maps up to a certain degree given the limitation on the number of microphones.

During the recent years, there has been an increasing interest in microphone arrays comprising fixed and continuously-scanning sensors. These arrays are an evolution of the early phased arrays introduced during the 1990s within the context of aeroacoustics, and are capable of obtaining highly-resolved noise source images and mitigate the sidelobe effects (i.e., the blurring due to the shape of the PSF). The continuous-scan approach can be considered an extension of the start-and-stop method of Lee and Bolton [21], which prevents damage to the microphones due to impulsive accelerations. These novel experimental techniques can reduce the total experiment time by an order of magnitude [22], compared to using non-synchronous microphone measurements. The continuous-scan technique has found applications in Near-

Field Holography (NAH) [23, 24] and beamforming [1, 25, 26, 27, 28], proving to increase the spatial resolution of the images significantly compared to traditional phased arrays with the same number of microphones and making it an ideal candidate for the study of complex aeroacoustic sources without incurring into increased monetary or computational costs.

The most prominent challenge of the continuous-scan paradigm includes the treatment of non-stationary signals that arise due to the motion of the sensors. Papamochsou *et al.* [1] addressed the issue by dividing the microphone pressure signals into quasi-stationary blocks and by using the Wigner-Ville Spectral estimation to handle the cross-correlations between microphones that had a relative velocity. Their work set the building blocks for the beamforming techniques presented in this work. An additional challenge of the continuous-scan paradigm relies in the signal processing, with new variables such as block length, number of blocks, etc., arising, which might introduce a certain degree of variability in the results if not systematically accounted for.

The present work presents several beamforming methodologies to process the data from microphone arrays that contain continuously-scanning sensors. A detailed study of the signal processing and its effects on the quality of the noise source maps is presented. As it will be demonstrated, the utilization of continuously-scanning microphones, combined with the signal processing guidelines proposed in this work, enables to obtain highly-resolved noise source maps that would only be possible to obtain if using a very large number of microphones. These high-resolution methodologies are applied to propulsion-related noise sources. Specifically, this work features high-fidelity noise source localization studies of subsonic jets, and supersonic jets that presented the screech phenomenon. The supersonic screeching jets are of interest within the context of beamforming given their small flow field features containing the shock-cells and the screech feedback loop process. Several upstream reflector surfaces of different geometries are utilized to change the oscillation dynamics of the screeching supersonic jet, with a new oscillation mode arising. The addition of the reflectors triggers modal interaction, which is manifested with the presence of new tones in the Sound Pressure Level (SPL) spectrum. Given the beamforming techniques of this work are applied to propulsion-related noise sources, a summary of the main components that characterize subsonic and supersonic jet noise is presented next.

1.2 Review of Jet Noise

Before further elaborating and describing the noise components of subsonic and supersonic jets flows, the concept of the acoustic far-field is briefly introduced. This is of particular relevance for the modeling and subsequent results that will be shown in this work, as the microphone measurements have been conducted in the acoustic far-field. The acoustic far-field might be defined as the region far away from the jet flow field where the pressure intensity decays radially as $1/\ell^2$, where ℓ is the distance between the source and the observer, and where the pressure field might be computed using linear approximations. Most microphone surveys used in noise source localization studies are computed in the acoustic far-field, as one avoids damaging the microphones due to the flow-field potentially impinging on them while also ensuring that the max SPL of the microphone is not reached. However, many of the details of the source that generate the observed far-field, such as the turbulence correlation length-scales, time length-scales, etc., are lost. As such, researches usually rely on modeling the acoustic sources, as will be further elaborated in the next lines and in Chapter 2. Numerous far-field and near-field studies on subsonic and supersonic jet flows have been conducted over the past decades, providing experimental evidence behind important physics of the production of noise. These, together with a characterization of the principal components contributing to jet noise, will be elucidated next.

1.2.1 Principal Components of Jet Noise

Jet noise is a branch of aeroacoustics that aims at studying and characterizing the noise generated by the instabilities involving the shear layer on subsonic and supersonic jets. These instabilities might interact with the shock-cell structures in supersonic jets, producing additional and high-intensity noise components, which are not found in their subsonic counterpart.

All turbulent jet flows contain small-scale and large-scale turbulence structures, with both playing a critical role in generating noise [29]. The large-scale structures are usually associated with the production of directional low frequency noise. Small-scale turbulence structures are related to the production of high-frequency uncorrelated noise, usually peaking near the nozzle exit plane [29, 30]. A universal component of noise that is common in all turbulent jet flow fields is the *turbulence mixing noise*, which is produced by the two types of structures introduced previously. These structures are usually correlated over some distances downstream of the nozzle exit, and have been modeled in the past by using amplitude modulated instability waves [31, 32] (i.e., wavepackets), quadrupoles [33], or monopoles [34, 6, 12], among others. The relevant levels of coherence of the large-scale turbulence structures make them an efficient noise generator, usually responsible for the SPL peak in subsonic jets, dominating the emission at angles close to the downstream axis (see Fig. 1.1). High-speed jet flows might also contain large-scale coherence structures that have a supersonic convective Mach number. Such structures produce intense Mach wave radiation that quickly overcome the noise generation, dominating the SPL at polar angles $\theta = cos^{-1}(1/M_c)$, where M_c is the convective Mach number, defined as $M_c = u_c/a_\infty$, with u_c being the convective velocity, and a_∞ the speed of sound.

A second component of jet noise, appearing only on supersonic jet flows, is known as *broadband shock-associated noise*, or using its acronym: *BBSAN*. BBSAN only appears when

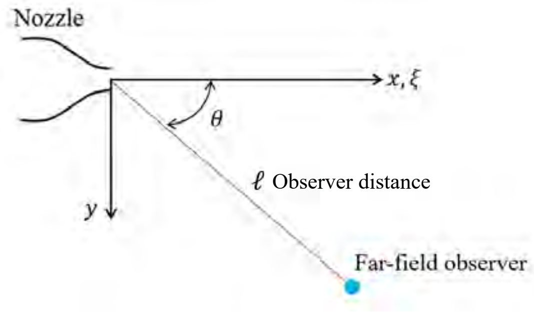

Figure 1.1: Sketch of a convergent nozzle and a far-field observer.

supersonic jets are imperfectly expanded (i.e., there is a pressure unbalance). The pressure miss-match at the nozzle exit requires rapid flow adjustments that are done through discontinuities (i.e., shocks and expansions). These shocks and expansions usually repeat along the jet plume, forming quasi-periodic patterns known as the shock-cell structure that is characteristic in a high number of military jets or the flow field produced by rocket engines. An example of this pattern is displayed in Fig. 1.2. The figure displays a spark Schlieren image of an overexpanded supersonic jet designed using the method of characteristics for $M_j = 1.5$.

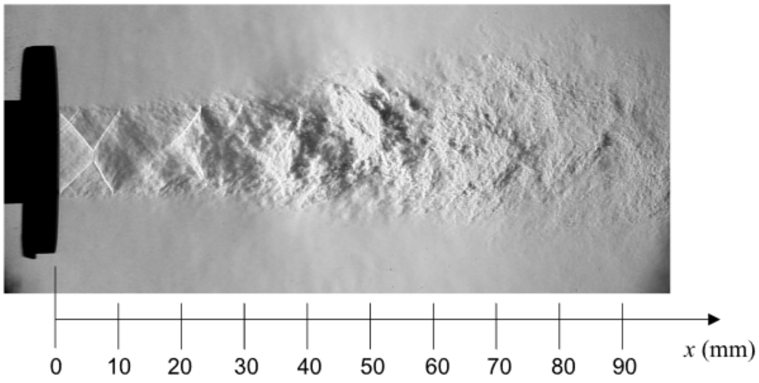

Figure 1.2: Spark Schlieren image of an overexpanded jet. Extracted from Ref. [1].

The third component characterizing jet noise is known as *screech tones*. This component, in parallel with the BBSAN, is only present in supersonic jets. Screech tones arise due to the interaction of the instability wave in the shear layer and the shock-cell structure in the jet plume. These prominent tones were first observed by Powell [35] in 1953, when he correctly pointed out that they were a consequence of a feedback mechanism loop, summarized in the next lines. The shear layer instability (Kelvin-Helmhotz) is convected downstream as it grows, interacting with the shock-cell structure of the jet. Between the 3rd and the 5th shock cell, the interaction leads to the production of upstream-propagating acoustic waves through a mechanism known as shock-cell leakage [36]. These waves interact with the nozzle lip, agitating the mixing layer [31] at the nozzle exit, and producing more downstream-propagating disturbances that close the feedback loop. A schematic of this process is displayed in Fig. 1.3. Jet screech usually shows in the SPL spectra as a combination of a fundamental tone and a multitude of harmonics. Their directivities are all very distinct [2], with some peaking at shallow polar angles and others peaking near $\theta = 90°$. The frequency and amplitude of the tones is strongly dependent on the jet Mach number and the nozzle lip thickness [37, 4], as it has been widely documented. They are also dependent on the existence and shape of reflection surfaces close to the nozzle exit. The high-sensitivity to the experimental boundary conditions will be detailed further in the next lines.

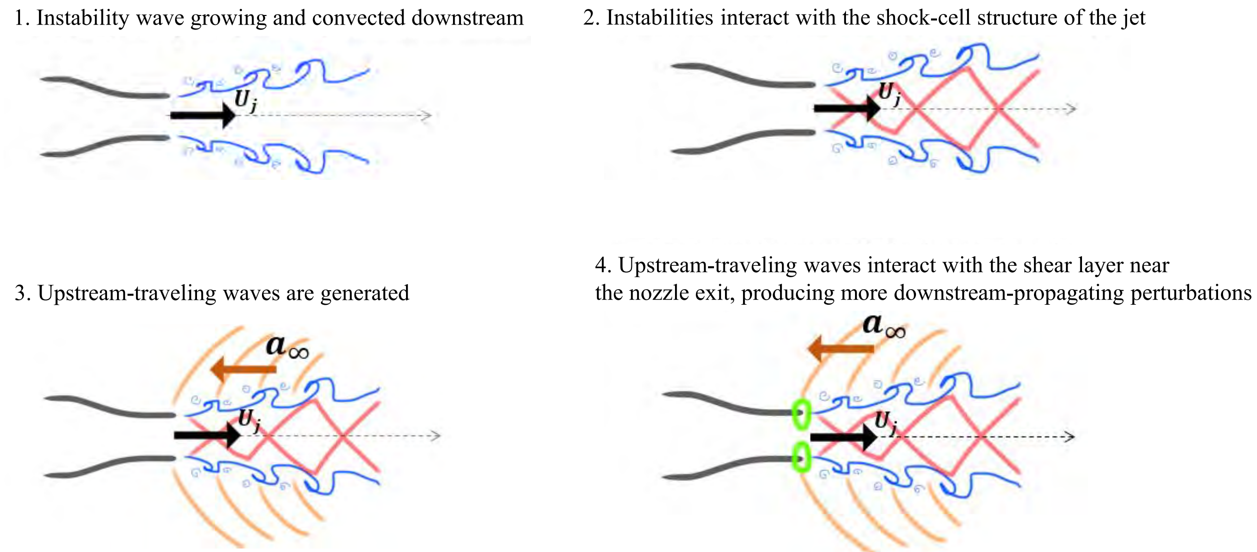

Figure 1.3: Schematic representation of the screech loop process, with the four stages involved.

A prominent feature of resonant flows such as supersonic screeching jets or impinging jets is their staging behavior. Small changes in the jet operating conditions such as total pressure jumps, nozzle lip thickness, the presence of upstream or downstream reflectors or air temperature and humidity might change the oscillation dynamics of the jet flow dramatically, incurring in large jumps of the resonance frequency. Powell [35] originally explained this issue by using a criteria of phase and amplitude. The phase criterion states that the frequency of the screech tone must be selected so that the feedback loop is self-sustaining. Additionally, Powell also stated that screech will only self-sustain in a steady-state fashion if the gain associated with the four stages of the feedback loop is selected such that the amplitude of each new disturbance matches, at least, that of the previous one. The two conditions, which are tightly linked, imply that adjustments on the gain criterion must be accompanied with adjustments on the phase criterion, which creates large frequency jumps and the staging behavior that is observed experimentally. The staging behavior is associated with distinct jet oscillation dynamics [38, 39, 3, 4]. Supersonic jet screech initially manifests as two toroidal or symmetric modes (A1 and A2) as the degree of underexpansion is increased on round jets. As one increases the pressure ratio, the jet transitions into a lateral oscillation (mode B). The jet finally oscillates in a helical fashion (mode C) for higher total pressures and might switch to a lateral oscillation again (mode D, similar to mode B) for very high pressure ratios. The staging behavior can be seen in Fig. 1.4, which has been extracted from the work of Tam *et al.*, "*Harmonics of Jet Screech Tones*" [2]. The vertical axis displays the screech wavelength normalized by the nozzle diameter (i.e., $\lambda_s/D = a_\infty/(f_s D)$), where a_∞ is the speed of sound, f_s is the screech frequency and D is the nozzle diameter. In addition, note how certain modes overlap. It has been experimentally demonstrated that the jet might lock itself to a preferred oscillation mode depending on the initial boundary conditions (i.e., nozzle lip thickness, presence of upstream reflectors, etc.) or contain two modes coexisting or in a mutually-exclusive fashion [4]. The specific reason of the above still remains unsolved but demonstrates the high degree of non-linearity governing resonant flows.

The distinct oscillation dynamics are also shown in Fig. 1.5. The image has been extracted

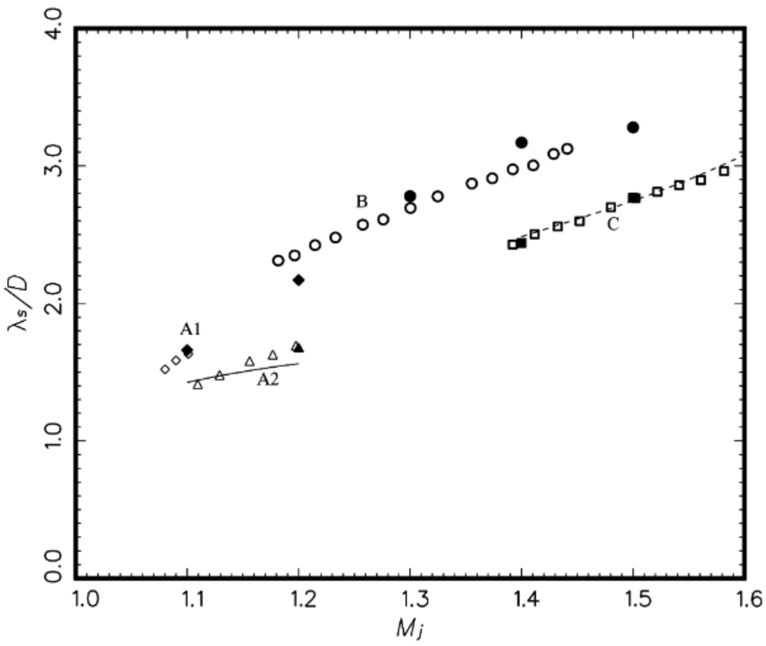

Figure 1.4: Normalized screech wavelength as a function of the fully-expanded jet Mach number of underexpanded round supersonic jets, extracted from Tam *et al.* [2]

from Umeda and Ishii, "*Sound sources of screech tone radiated from circular supersonic jet oscillating in the helical mode*" [3] and was obtained using a Schilieren apparatus with an exposure time of 1 μs. The jet flow issued from a convergent nozzle at different total pressures. Clear symmetric structures can be seen for oscillations modes A1 and A2. It can also be observed how the upstream-propagating waves of the symmetric modes are weaker compared to those present for mode B or C. As such, one expects the tonal components of mode B or C to be more prominent to those of A1 and A2 [37, 4].

Finally, an example of an SPL spectrum of the same imperfectly expanded jet, recorded with a far-field microphone located at $\theta = 70.65°$ is shown in Fig. 1.6. The image is particularly useful as it displays the three components that were previously introduced which characterize jet noise. Obviously, screech tones and BBSAN are eliminated if there are no shocks present within the jet flow (i.e., if the nozzle is working at its design conditions). As such, these two components are not usually a cause of concern within the context of commercial aviation.

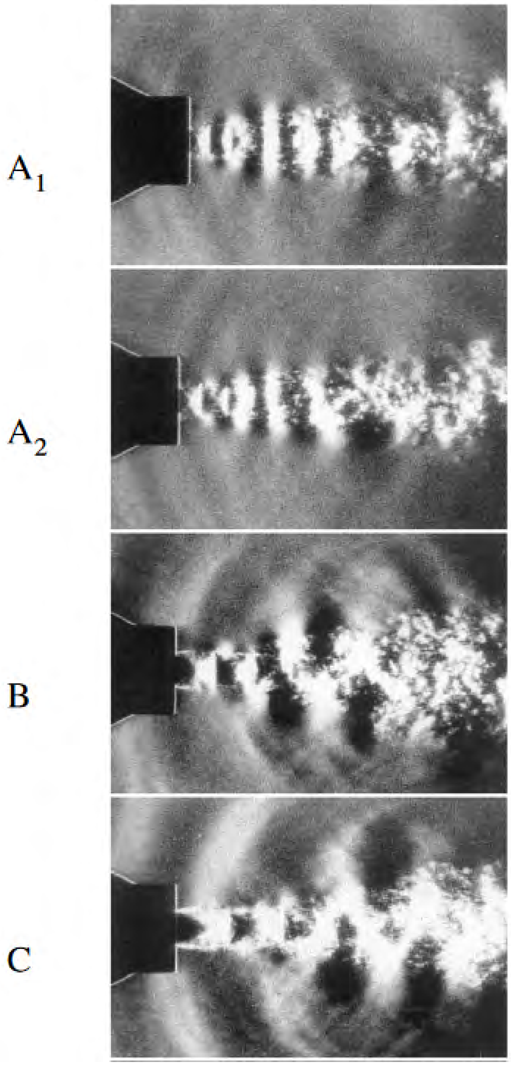

Figure 1.5: Schilieren photographs of the convergent circular jets oscillating in mode A1, A2 (symmetrics), B (lateral) and C (helical). Figure extracted from Umeda and Ishii [3].

However, they are an important noise generator to take into account for the military, rockets and for supersonic transportation. High degrees of tonal noise are linked to hearing losses of military aircraft carrier personnel and sonic fatigue failure of aircraft and rocket structures, incurring into billions of dollars of healthcare and maintenance expenditure every year.

Having introduced the main components associated with the noise emanating from subsonic and supersonic jet flows, the following lines will describe the mechanisms of noise generation and provide a brief summary of how the scientific community has understood the topic over

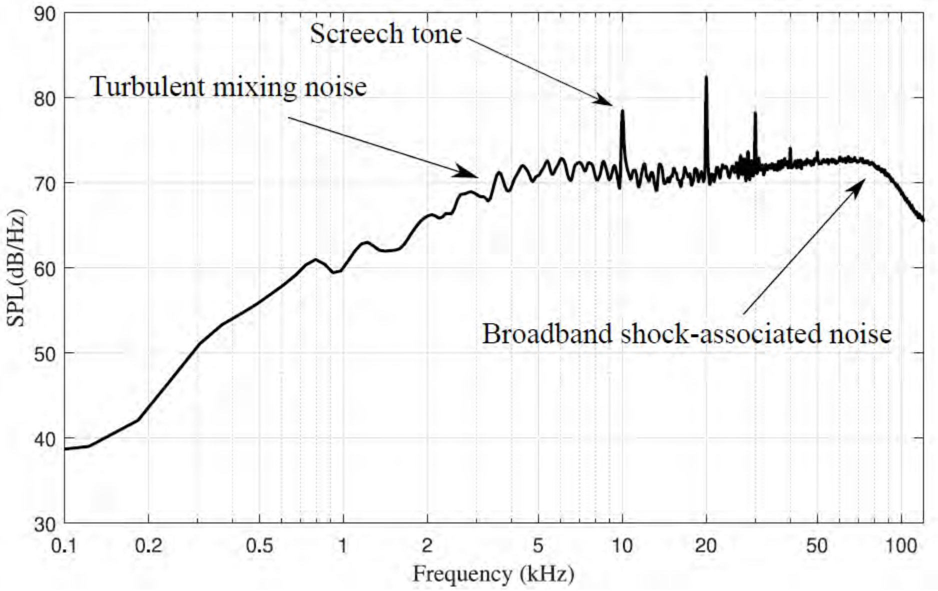

Figure 1.6: Far-field supersonic jet noise SPL spectrum of an imperfectly-expanded jet experiment performed at UCI. The microphone was located at a polar angle of 70.65°.

the recent decades.

1.2.2 The Sources of Jet Noise

The production of noise due to the flow structures that are present in turbulent jets was first described in the seminal work of Lighthill [33, 40]. Lighthill derived an exact relationship, commonly referred to as Lighthill's equation, starting from the Navier-Stokes equations, which described the sound radiated by a turbulent flow field contained within a limited volume in a quiescent environment (i.e., in ambient air with no mean flow velocity). The equation governing the sound production under the above conditions is

$$\frac{\partial^2 \rho}{\partial t^2} - a_\infty^2 \nabla^2 \rho = \frac{\partial^2 T_{ij}}{\partial x_i \partial x_j} \tag{1.1}$$

Notice how the left hand side of the relationship resembles the acoustic wave equation on a quiescent medium (i.e, there is no convective term). The right hand side of the equation represents the generation of noise and its propagation through the turbulent field, where T_{ij} is the Lighthill's stress tensor, which contains contributions from turbulence self-interaction, viscous stresses and the compressive stress tensor. Lighthill stated how the tensor reduces to $T_{ij} \approx \rho_0 u_i u_j$ for low Mach number, unheated flows, with an approximation error on the order of M^2. In fact, the turbulence self-interaction, which involves the product $\rho u_i u_j$ is the dominant component in the production of noise in unbounded turbulent jets, especially when the Reynolds numbers is high. He also showed how the stress field emitted sound like an equivalent mathematical quadrupole field that had a strength per unit volume equal to the stress tensor T_{ij}. The quadrupole source model has been widely-used the past decades when utilizing Lighthill's acoustic analogy. However, as will be discussed within the next lines, this source treatment is not the only jet noise model that exists in aeroacoustic analysis and, in fact, the quadrupole nature of the jet noise source has been contested in more recent works [29].

In his seminal work, Lighthill utilized dimensional analysis to demonstrate that the acoustic sound power intensity of turbulent jet flows is related to, approximately, the 8th power of the exit velocity for $M < 1$ (that is $I \sim U_j^8$). This important relation was one of the main drivers in the early research on new jet propulsion devices. To some degree, these relationships helped in the development of the turbofan engine and its wide implementation in commercial aviation in the present. The invention of the turbofan engine was a major breakthrough, proving to be a significant improvement on overall efficiency and noise reduction when operating at high bypass ratios compared to the utilization of turbojet engines. The noise reduction was achieved by having a lower total exit velocity, shielding the inner high-speed jet with a slower outer velocity flow emanating from the inlet fan. Recall that while Lighthill's scaling law is a powerful tool to predict the noise impact for low Mach numbers, it is still based on a mathematical quadrupole and does not appear to hold at high Mach numbers. However, the relationship is still used and provides an order of magnitude estimate of noise in the early design stages of propulsive devices. Years later, Vishwanathan

[30] showed that the power was, in fact, oscillating near 8, but not exactly 8. Vishwanathan demonstrated that the power exponent decreased for increasing total temperature ratios of the turbulent jet, and is different at other jet Mach numbers.

In 1963, almost a decade later after the work by Lighthill was first released, Ffowcs Williams published his influential work *"The noise from turbulence convected at high speed"* [41]. He showed that, for high speed flows, where Mach wave radiation is relevant, the sound power intensity is related to, approximately, the 3rd power of the exit velocity of the flow ($I \sim U_j^3$). His reasoning was verified utilizing measurements of very high speed flows taken by Chobotov and Powell [42]. The departure from Lighthill's 8th power law was partly attributed to compressibility effects, which caused a reduction in the source strength and a reduction of the transverse velocity fluctuations in the jet mixing layer. Other authors have proposed that the scaling power ranges from 3 to 6, and shown it has a strong dependence on the jet Mach number [43], suggesting that the sources of noise could also be mathematically represeted using monopoles and dipoles. The departure from the 8th power law is relevant, and might be related to different source mechanisms.

More recently, studies have concentrated on studying the dependence of jet noise emission on polar angle, frequency, total temperature ratio and jet Mach number. For instance, Viswanathan [44] (2007) showed how noise is generally suppressed with increasing total temperature ratios at several polar stations. He also demonstrated how the exponent used in his power law ranges from 8 to 5 depending on the temperature ratio, Mach number and polar angle, suggesting complex noise mechanisms involving the large- and small-scale turbulence structures. The overall trends seen in his study show how the exponent decreases with increasing total temperature ratio and increases with polar angle. The study also showed experimentally that decreasing the jet Mach number decreases the production of noise, as stated by Lighthill decades earlier. A final but yet important conclusion of his work indicates that the 8th power law exponent still holds for unheated jets near the peak emission region within a reasonable range of jet Mach numbers.

In 2008, the influential work of Tam *et al.* *"The sources of jet noise: experimental evidence"* [29] explored the possibility of different source mechanisms that would explain the different SPL distributions at distinct polar angles. In their work, they concluded that there were two distinct sources of turbulence mixing noise: the large- and the small-scale turbulence structures, each with a different behavior that causes different imprints in the acoustic far-field. Amongst the most important findings of their study, two were of particular relevance. First, they found that the acoustic field in the downstream direction was coherent radially and along large polar sectors, suggesting it is generated by large coherent turbulence structures. Secondly, the acoustic field near the sideline direction (i.e., $\theta \approx 90^\circ$) is correlated over narrow polar regions, with a SPL that appears relatively flat. This suggests the field is generated by small-scale incoherent turbulence structures. The authors utilized far-field single microphone data, auto-correlations and two-point correlations of turbulent jets operating over a wide range of Mach numbers to support their claims.

These above results were very relevant and must be put in the appropriate context. Many theoretical approaches linked the sources of noise to quadrupoles using Lighthill's acoustic analogy. The findings of Tam *et al.* "challenged" the quadrupole source model. Rather than attributing the recorded acoustic far-field to distinct quadrupole sources, the authors suggested that the true nature behind the generation of turbulence mixing noise was the large- and small-scale turbulence structures, which dominated distinct polar regions. Mathematically, one could create an equivalent acoustic far-field if one used the quadrupole model. However, these mathematical descriptions do not necessarily need to be the physical mechanisms that generated noise. That is because the solution of the inverse problem is not unique (i.e., given a particular acoustic field, one might generate it using quadrupoles, monopoles, wavepackets, etc., and their combinations). This study will also utilize a model for the acoustic sources, and will be explicitly introduced in Chapter 2. The next lines will describe the upstream- and downstream-traveling perturbations that are found in supersonic jets, and how these different families of waves are related to the screech feedback mechanism loop that has been detailed in the preceding paragraphs. This is of relevance within this study as significant efforts have been made to study overexpanded screeching jets.

1.2.3 Waves in Supersonic Jets

Supersonic jets that contain shocks within the jet plume make them prone to exhibiting a degree of aeroacoustic resonance. For free supersonic turbulent jets, the resonance is manifested in the form of screech. However, resonance might be manifested differently depending on the geometry of the problem and jet Mach number (e.g., subsonic and supersonic impinging tones). As stated in the preceding section, jet screech involves a complex feedback loop process in which downstream- and upstream-propagating waves are involved. The downstream-propagating wave is the only process that provides energy to the feedback mechanism, extracting it from the mean flow and contributing to the growth of the instability wave [45, 46] contained in the shear layer. While the nature of the downstream-traveling wave involved in jet screech is clear (Kelvin-Helmholtz instability type of wave), that of the upstream-traveling wave is less clear.

It was firstly proposed by Powell [38] that the upstream-propagating waves were free-stream acoustic waves, propagating outside of the jet plume. These waves provided the closure for the feedback mechanism loop involved in jet screech, and had strong supporting experimental evidence, as some shapes resembling to acoustic waves were seen in Schlieren images (see Fig. 1.5). In addition, several screech frequency prediction models, based on a sonic wave speed, also predicted the screech frequency relatively well for some modes. For instance, Powell's phased monopole array model [38] is able to predict the frequency of resonance of mode B (lateral oscillation) remarkably well when one utilizes a sonic phase speed. The model of Panda *et al.* [47] has also been used to predict the screech frequency of other modes based on the standing wave pattern caused by KH and upstream-traveling free-stream waves. However, it has been found that these models do not capture well the staging behavior of jet screech nor they work when multiple tones are present. Perhaps it was this issue that triggered researchers to believe that additional waves might be present in jet screech, besides the free-stream upstream-traveling waves.

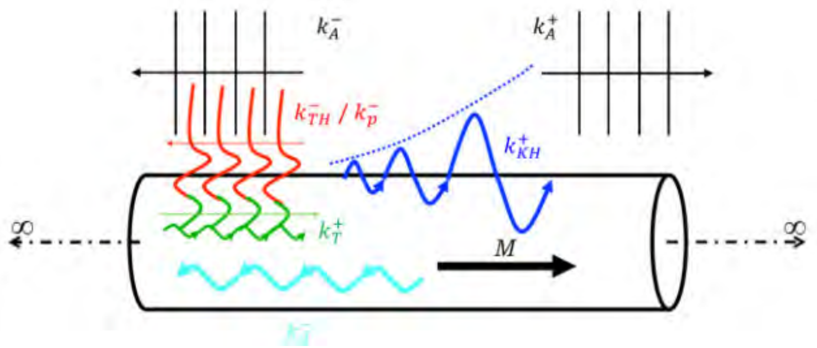

Figure 1.7: Schematic of the different waves supported by a compressible vortex sheet model. Extracted from Ref. [4]

.

Tam and Ahuja [45] proposed that the upstream-traveling wave might be a guided jet mode rather than a free-stream acoustic wave. Their work was founded on the previous work of Tam and Hu [48], who originally showed that supersonic jet flows support three types of waves: Kelvin-Helmholtz, supersonic instability waves and neutral waves. They also reported that at very high Mach numbers, the KH became indistinguishable from the supersonic instability waves. Nevertheless, at the typical Mach numbers involved in jet screech, KH dominates the downstream-traveling part. Concerning the upstream-propagating waves, the existence of guided neutral waves might change our understanding of jet screech and provide a closure for the feedback loop mechanism. These neutral upstream-propagating waves have been denoted by k_{TH^-} in past works and have well-defined radial and azimuthal structures.

The recent years have seen an increased interest in the role played by the distinct jet acoustic modes on aeroacoustic resonance [49]. To that end, researchers have used a compressible cylindrical vortex sheet analogy to find the waves supported by a supersonic jet (Fig. 1.7). New trapped acoustic modes within the jet have been recently discovered [4], with them being capable to transport energy upstream (k_{d^-}) or downstream (k_{T^+}). Thus, these modes and the free-stream acoustic waves are all capable of closing the screech feedback mechanism loop. The free-stream acoustic waves are denoted by k_{A^-} (upstream-traveling) and k_{A^+} (downstream-traveling) in the figure. Shen and Tam [50] originally mentioned that screech could be closed with a k_{TH^-} wave rather than a free-stream acoustic wave in their 2002 numerical study. Their predictions have been recently verified utilizing LES data for modes A1 and C, and using a triple decomposition based on POD for mode A2.

Perhaps the most challenging part of these neutral acoustic waves lies on their radial structure. As seen in Fig. 1.8, these neutral acoustic wave have strong support outside of the jet plume. Thus, these particular modes might appear indistinguishable from free-stream upstream-propagating waves in Schlieren imaging techniques or noise source localization studies (the latter would only show a source at the nozzle exit plane) and it might be the reason why they have been unnoticed for several decades. The jet screech feedback loop will be seen in Chapter 5 when utilizing the high-resolution experimental techniques developed here. However, the exact nature of the waves will not discerned using the same methodologies.

1.3 Research Goals

The overarching goal of the research presented in this work is the development of advanced acoustic testing techniques for microphone arrays that contain continuously-scanning sensors, and utilization of the proposed methodology to study propulsion-related noise sources. As stated in the previous sections, traditional microphone array setups, in many instances, lack of the spatial resolution that is required to study complicated acoustic fields such as

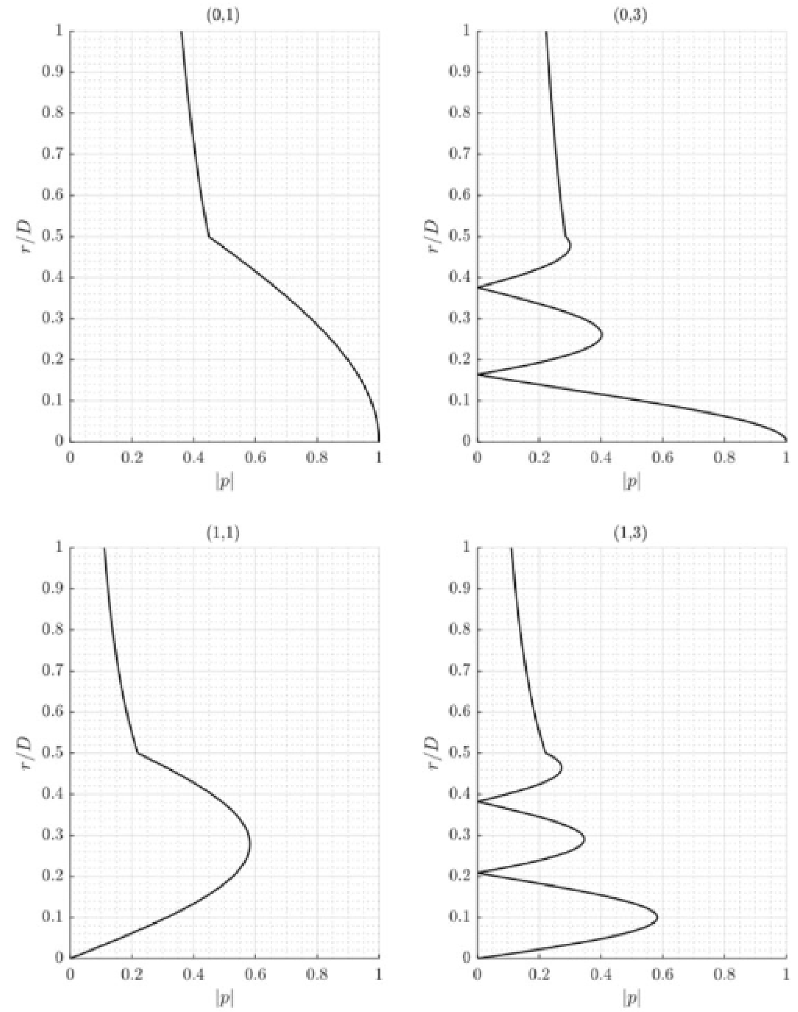

Figure 1.8: Pressure eigenfunction for the upstream-traveling acoustic modes (k_{TH^-}) of mode (m,n)=(azimuthal,radial) for a jet with $M_j = 1.5$, obtained using a compressible vortex sheet model. Extracted from Ref. [4]

.

those emitted by subsonic and supersonic jet flows. This project involves a combination of advanced experimental setup designs and theoretical development of tools and guidelines to process microphone data from continuously-scanning sensors for the study of such jet flow fields. The ability of the continuous-scan approach to obtain high-resolution noise source maps will be demonstrated. In addition, the images obtained from an array containing fixed sensors only will be used for assessing the improvement attained with the continuous-scan paradigm. The remaining sections this dissertation are organized as follows.

An overview of the traditional noise source localization techniques is provided in Chapter 2. The model for the acoustic source is introduced first, followed with the description of time-domain and frequency-domain delay-and-sum beamforming. A first approximation to the continuous-scan paradigm consists on using several Cross-Spectral Submatrices (CSSM), utilizing the non-repeated elements of each matrix to form the noise source map. However, this results into deconvolution becoming impossible due to the lack of a global Cross-Spectral Matrix (CSM). As such, two additional techniques are introduced so that advanced deconvolution processes can be used in conjunction with the continuous-scan paradigm. These techniques correspond to a matrix completion process and a partial field decomposition, and their formulation and assumptions are described in detail. Chapter 2 also introduces the concept of the point spread function and explains how it affects the beamformed images. Lastly, the chapter briefly summarizes three deconvolution processes that are used in this work: DAMAS, CLEAN-SC and the Richardson-Lucy (R-L) approach.

The signal processing involved in the continuous-scan approach is described in Chapter 3. The signal segmentation process and minimization of signal non-stationarity have important impacts on the quality of the resulting noise source images. Quantities such as block length, number of blocks, and block overlap are introduced and discussed, and clear guidelines for signal division are presented. The effects of the signal processing on the resulting noise source maps is assessed in terms of the point spread function and the sidelobe levels.

The experimental facilities are discussed in Chapter 4. The anechoic chamber and details of the microphone array are presented, including the synchronization and tracking of the scanning microphones. In addition, the acoustic sources studied in this work are shown. These involve an impinging jets source, which is an approximation to a point source that uses the collision of four jets, a subsonic jet in isolation and in three shielding configurations, and several supersonic jet flow configurations. The latter presented the phenomenon of screech.

Chapter 5 includes the results section. Details of the SPL spectra at different polar stations are presented. The acoustic source localization images are also displayed. Parameters such as peak noise source location for the subsonic jet or screech source location for the supersonic jet flow are introduced. In addition, the flow features extracted from the beamforming measurements are used to predict the screech frequency of jet oscillation mode B with a high degree of accuracy, underscoring the potential of the continuous-scan approach.

Finally, Chapter 6 briefly provides the concluding remarks of this work and details future considerations.

Chapter 2

Beamforming

A phased microphone array is a system consisting of a spatially-distributed number of microphones that records pressure signals simultaneously. The pressure signals are then used to determine the location of the acoustic sources of interest by taking into account the amplitude and phase differences of the signals recorded by the distinct sensors. By electronically adjusting these differences in a process known as beamforming, one can determine the position of the sources and quantify their strength. A certain nature about the acoustic sources must be modeled in beamforming and many related deconvolution approaches. A schematic of a noise source and a microphone array is shown in Fig. 2.1. No assumptions with regards to the noise source or array have been made.

The present chapter outlines the key points in the noise source localization process, including a description of how the sources of interest are modeled. Then, formulations for beamforming in the time domain and frequency domain are presented. The effects of the array geometry through the point spread function are later discussed. Finally, beamforming is extended to microphone arrays comprising fixed and continuously-scanning sensors. The challenges of the continuous-scan approach include the treatment of signals that are non-stationary in

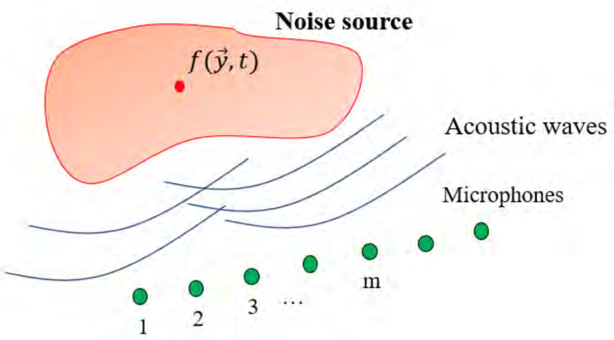

Figure 2.1: Schematic of a noise source and a microphone array.

time, requiring complex signal processing techniques. The motion of the sensor introduces a Doppler-shifted frequency and a frequency of oscillation of the entire spectrum for sensors that have a relative velocity [1]. The continuous-can formulation presented in this chapter will specifically treat the Doppler-shift in frequency. The expression of the oscillation frequency of the cross-spectral densities for sensors that have a relative velocity will also be derived.

Parts of this chapter are a partial reprint and adaptation of Morata, D., and Papamoschou, D., *"Extension of Traditional Beamforming Methods to the Continuous-Scan Paradigm"*, AIAA Paper 2022-1154, doi: 10.2514/6.2022-1154. Excerpts from the chapter have been submitted as a full-length journal paper to the Journal of the American Institute of Aeronautics and Astronautics (AIAA Journal) as *"High-Resolution Continuous-Scan Beamforming"*, with Morata, D., and Papamoschou, D., as the authors, as of April 2nd, 2022

2.1 Model for the Acoustic Source

Suppose a turbulent flow issuing from a nozzle, and a far-field microphone array containing a number $\mathcal{M}_f$ of fixed microphones, as schematically depicted in Fig. 2.2. The beamforming study presented in this work assumes a certain nature about the acoustic source that generates the pressure far-field. The source is modeled as a one-dimensional distribution of uncorrelated monopole sources [17]. It is further assumed that the medium has a zero velocity (no co-flow) and constant speed of sound a_∞. The governing equation of the problem is then

$$\frac{1}{a_\infty^2}\frac{\partial^2 p}{\partial t^2} - \nabla^2 p = 0 \tag{2.1}$$

As stated in the preceding section, the uncorrelated monopole source model is one of the multiple representations that can be used for the acoustic inverse problem (i.e., find the acoustic sources given an acoustic far-field). Researchers have utilized dipole sources [51], wavepackets [32, 52], etc., with the later allowing to infer the degree of source coherence. However, the uncorrelated monopole source model is still the most widely-used representation of jet noise in beamforming studies given its relative simplicity and its ability at obtaining physical results. In addition, most of the deconvolution algorithms available assume the same nature about the acoustic source.

The pressure recorded by a fixed microphone m located in the acoustic far-field at a distance $\ell_m(\xi) = \sqrt{(x-\xi)^2 + y^2 + z^2}$ from the acoustic source, where (x, y, z) are the coordinates of the microphone, and ξ is a running coordinate along the x axis, obeys the relationship

$$p_m(t) = \int_{\mathcal{L}} \frac{f\left(\xi, t - \dfrac{\ell_m(\xi)}{a_\infty}\right)}{\ell_m(\xi)} d\xi \tag{2.2}$$

where $f(\xi, t)$ is the strength of the acoustic source at location ξ. It is seen how the pressure recorded by the microphone is a consequence of all the sources present within the region of interest $\mathcal{L}$.

The amplitude and phase of the recorded pressure signal obviously depends on the relative position between the source and the microphone, as stated by Eq. 2.2. This implies that two

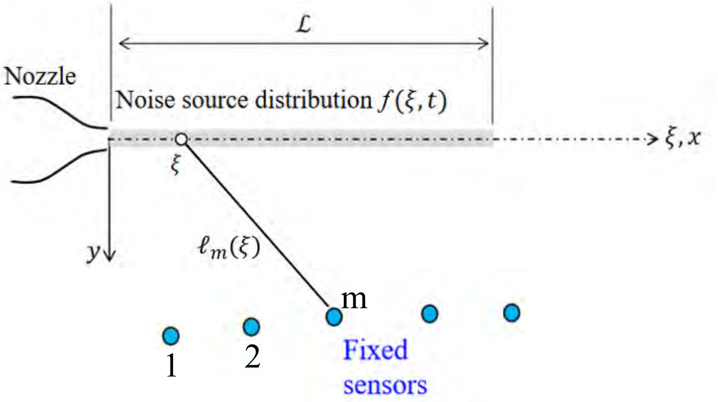

Figure 2.2: Far-field microphone array and the one-dimensional model of the jet noise source.

microphones at distinct positions will perceive a pressure signal at different time instances, with different statistics, depending on the directivity of the source. The one-dimensional uncorrelated monopole source model sets the foundation for the results discussed in this work, including the extension of the beamforming techniques to continuously-scanning sensors.

2.2 Time Domain Beamforming

The widely-used delay-and-sum (DAS) beamforming algorithm exploits the previously-mentioned ideas about the differences in phase and amplitude between the distinct microphones in order to find the location and strength of the acoustic sources. The objective behind the DAS technique is to sum all the microphone signals with added time delays that are dependent on the relative position between the microphone and the point of interest. These signals are summed coherently or incoherently as a function of the time delays that are used, and depending on whether there exists an acoustic source at the point of interest. Considering only one-dimensional noise source distributions the usual summation relationship to location

ξ utilized in the DAS process is given by

$$s(\xi, t) = \sum_{m=1}^{\mathcal{M}_f} \frac{1}{\ell_m(\xi)} p_m(t + \tau_m(\xi)) \tag{2.3}$$

where

$$\tau_m(\xi) = \frac{\ell_m(\xi)}{a_\infty} \tag{2.4}$$

is the source-sensor travel time. Usually, Eq. 2.3 is expressed in a compact form as

$$s(\xi, t) = \sum_{m=1}^{\mathcal{M}_f} w_m p_m(t + \tau_m(\xi)) \tag{2.5}$$

where the term w_m is a microphone weight that might include corrections for sound convected through the shear layer or shading algorithms to improve the resolution of the beamformer output. As one scans along the x axis, a local maximum of $s(\xi, t)$ will be found near the location of the source. Usually, the location of the maximum of $s(\xi, t)$ is the location of the source with some caveats, as will be further detailed in the next sections. If the scanned point does not contain any acoustic source then the signals are not summed coherently, and thus the value of $s(\xi, t)$ is no longer a local maximum. Note that, many times, the microphone weight w_m might include additional terms to improve the array performance or to take into account the sound convected due to the shear layer [8, 53].

2.3 Frequency Domain Beamforming

Beamforming studies typically use frequency domain representations to characterize the acoustic sources of interest. This approach is usually preferred over the time-domain representation as one can study the strength and frequency content of the noise sources that produce the recorded acoustic far-field. The process is similar to the time domain beamforming. However, one makes use of the Fourier transform to translate signal time delays into phase shifts. The process starts by taking the Fourier transform of Eq. 2.5, which is

$$S(\xi,\omega) = \int_{-\infty}^{\infty} \sum_{m=1}^{\mathcal{M}_f} w_m p_m(t+\tau_m(\xi)) e^{-i\omega t} dt \tag{2.6}$$

Using the time-shift property of the Fourier Transform, Equation 2.6 can be expressed as

$$S(\xi,\omega) = \sum_{m=1}^{\mathcal{M}_f} w_m P_m(\omega) e^{-i\omega\tau_m(\xi)} \tag{2.7}$$

where $P_m(\omega)$ is the Fourier transform of the pressure signal $p_m(t)$, and $e^{-i\omega\tau_m(\xi)}$ is known as the steering vector element for microphone m to location ξ, and contains information about the phase shifts applied to the microphone. Traditional beamforming approaches aim at obtaining the array power spectrum, which reveals the distribution, intensity and frequency content of noise sources within the region of interest. The array power spectrum at location ξ and frequency ω is computed as

$$Y(\xi,\omega) = S(\xi,\omega)S^*(\xi,\omega) = \sum_{m=1}^{\mathcal{M}_f}\sum_{n=1}^{\mathcal{M}_f} w_m w_n \left(\overline{P_m(\omega)P_n^*(\omega)}\right) e^{-i\omega\tau_m(\xi)} e^{i\omega\tau_n(\xi)} \tag{2.8}$$

where the symbol $*$ is used to denote the complex conjugate, and $\overline{(\cdot)}$ is used to indicate the spectral averaging involved in the Fast Fourier Transform (FFT) algorithm. The above equation is normalized by the number of microphones used by dividing it by $\mathcal{M}_f^2$. The quantity $\overline{P_m(\omega)P_n^*(\omega)}$ is known as the Cross-Spectral Matrix (CSM) and is the starting point of all beamforming approaches. The CSM contains all the relevant statistics for a particular experiment (i.e., the auto- and cross-spectral densities of all microphones of the phased array) for all frequencies ω. In addition, the CSM only needs to be calculated once for each frequency, as it is independent of the beam steering process. A schematic of a CSM for a generic acoustic experiment is shown in Fig. 2.3.

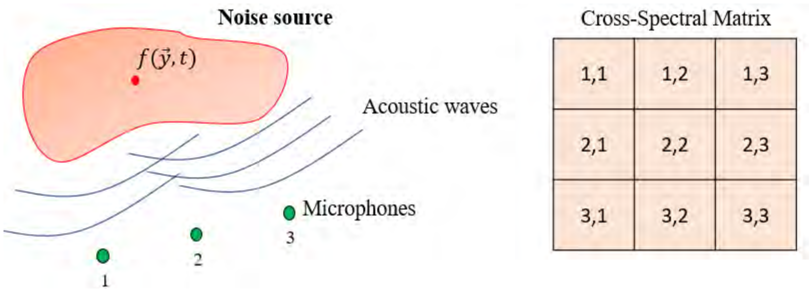

Figure 2.3: schematic of a CSM for a generic acoustic experiment that involves three fixed microphones.

The above equation is usually expressed in a more compact form as

$$Y(\xi,\omega)=\frac{\mathbf{g}_(\xi,\omega)\mathbf{C}(\omega)\mathbf{g}^H(\xi,\omega)}{\mathcal{M}_f^2} \tag{2.9}$$

where $C(\omega)=\overline{P_m(\omega)P_n^*(\omega)}$, $g(\xi,\omega)$ is the steering vector to location ξ, and H indicates the complex transpose. The steering vector $\mathbf{g}(\xi,\omega)$ is constructed as

$$g(\xi,\omega)=[w_1e^{-i\omega\tau_1(\xi)} \quad w_2e^{-i\omega\tau_2(\xi)} \quad \ldots \quad w_{\mathcal{M}_f}e^{-i\omega\tau_{\mathcal{M}_f}(\xi)}] \tag{2.10}$$

A modified version of the Eq. 2.9 can be used to increase the dynamic range of the microphone array by reducing microphone self-noise contamination and giving more weight to the cross-spectral terms, which offer information about the phase of the acoustic source. The beamformed maps can be generated as follows: assume that the microphone self-noise contamination is concentrated along the CSM diagonal; then, obtain the beamformed image as

$$Y(\xi,\omega)=\frac{\mathbf{g}(\xi,\omega)\mathbf{C}_{\text{diag}=0}(\omega)\mathbf{g}^H(\xi,\omega)}{\mathcal{M}_f^2-\mathcal{M}_f} \tag{2.11}$$

where $\mathbf{C}_{\text{diag}=0}(\omega)$ places zeros on the diagonal of the CSM. When executing the diagonal removal operation, however, one must be cautious given that the resulting CSM may contain negative eigenvalues linked with negative source auto-powers, which are considered non-physical. Negative source auto-powers can be considered to be noise sinks instead of noise sources. The diagonal reconstruction process (DiRec) of Hald [54] or Dougherty [55] is an alternative to the diagonal removal method. Given that the DiRec approach is a semidefinite programming (SDP) problem, it can be used in conjunction with sophisticated convex optimization libraries like CVX [56, 57]. Then, the resulting noise source image can be obtained using Eq. 2.9 utilizing the CSM with the optimized diagonal. The diagonal removal (or reconstruction) operation is usually performed in wind tunnel testing, where the microphones are subject to incoherent noise due to the boundary-layer interaction. The implementation of microphone phased arrays in wind tunnels is slightly different to that used in anechoic chambers as one must attempt to minimize boundary-layer interaction. The reader is referred to Refs. [58, 59] for additional information on beamforming in wind tunnels.

2.4 Microphone Array Performance: the Point Spread Function

Denoting the Fourier transform of the source $f(\xi, t)$ as

$$F(\xi, \omega) = \int_{-\infty}^{\infty} f(\xi, t) e^{-i\omega t} dt \tag{2.12}$$

the source spectral density can be modeled as

$$\overline{F(\xi, \omega) F^{*}(x, \omega)} = \Phi(x, \omega) \delta(x - \xi) \tag{2.13}$$

where the source is assumed to be spatially incoherent. The array response obtained through DAS (i.e., the beamformed source map) can be shown to be a convolution between the PSF and the noise source distribution. This is mathematically expressed as

$$Y(\xi,\omega) = \int_{\mathcal{L}} \mathcal{S}(x,\xi,\omega)\Phi(x,\omega)dx \tag{2.14}$$

where $\mathcal{S}(x,\xi,\omega)$ is the PSF, $\Phi(x,\omega)$ is the source distribution that causes the array response $Y(\xi,\omega)$ when measured with the array, and $\mathcal{L}$ is the region of interest. The PSF at location x_0 is

$$\mathcal{S}(x_0,\xi,\omega) = \sum_{m=1}^{\mathcal{M}_{\{}} \sum_{n=1}^{\mathcal{M}_{\{}} w_m(\xi)w_n(\xi)w_m(x_0)w_n(x_0)e^{i\omega[\tau_m(x_0)-\tau_m(\xi)]}e^{i\omega[\tau_n(\xi)-\tau_n(x_0)]} \tag{2.15}$$

The PSF determines how the microphone array responds to a monopole source placed at a position $x = x_0$. Ideally, the microphone array would respond to such source by showing a small point source in the noise source map (Eq. 2.9), without creating artificial or "ghost" sources. However, due to the limited number of microphones that is used, the output will be spatially aliased, containing artificial sources due to the contamination introduced by the sidelobes. In other words, the microphone array works as a spatial filter bank that aliases the source distribution due to its geometric constraints.

It has been thoroughly argued [60] that in order to avoid significant spatial aliasing effects, the distance between microphone pairs should not exceed half of the acoustic wavelength that is being resolved. The criterion is similar to the Nyquist temporal sampling requirement, in which one must sample the signal, at least, at twice the frequency of the maximum frequency that is expected. This clearly introduces a challenge when resolving high frequencies, where the acoustic wavelength is very small, and requires a high number of sensors. The effect of the array geometry on the sidelobes has been studied in the past and some geometries that minimize sidelobe formation have been proposed [61, 62, 10]. However, the constraint on the microphone spacings still remains and one might only attain a certain degree of improvement using optimized geometries.

The PSF causes a blurring effect on the imaged noise source distribution. This effect is not something seen in phased microphone arrays only. In fact, investigations on how to separate the effects of the PSF from the real image (or the real source) began within the field of astronomy in the 1970s. Scientists were using a combination of telescopes to form a focused image of galactic object but they only obtained blurred images. An example of this is shown in Fig. 2.4. The figure shows the image of the lunar surface, obtained from the processing of a combination of measurements (left), and the reconstructed (or deconvolved) image (right). The effects of the PSF are critical, as it lowers the spatial resolution that is required in many instances.

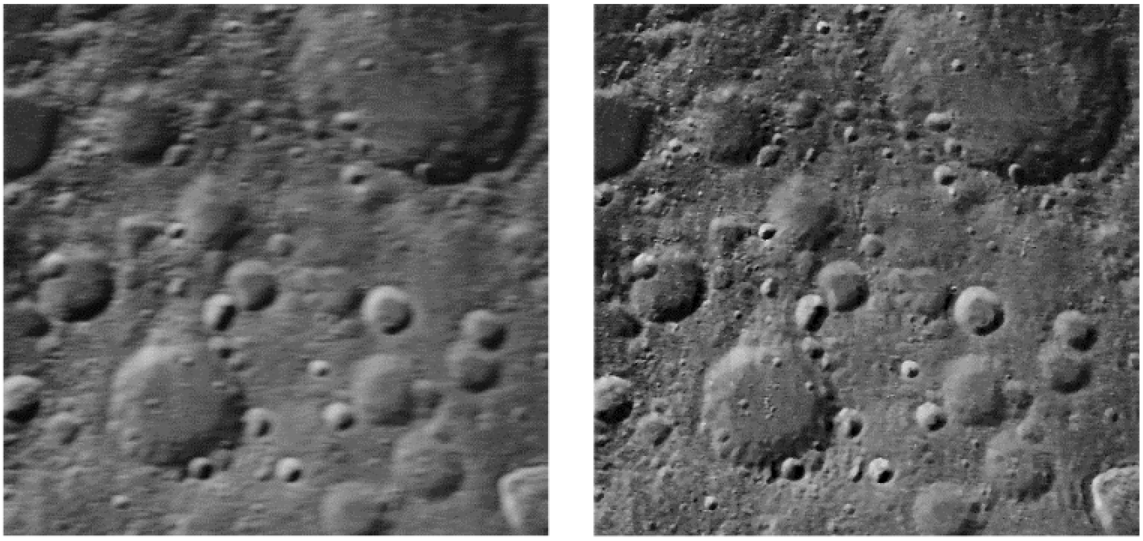

Figure 2.4: Image of the lunar surface. Image affected by the point spread function (left) and real image (right). Image extracted from Ref. [5].

During the past decades, numerous deconvolution algorithms have been presented with the aim to improve the spatial resolution of the image and reject the sidelobes that are inherent to the PSF. The distinct deconvolution approaches attempt at separating the contribution from the sidelobes from the beamformed image. These techniques again assume a certain nature about the acoustic sources that are present (i.e., incoherent monopoles). This work will explore three of such methods: DAMAS [63, 13], CLEAN-SC [14] and the Richardson-Lucy

(R-L) algorithm [15, 16, 17, 64, 28]. The DAMAS and CLEAN-SC deconvolution processes are implemented as in Refs. [63] and [14] in this work, respectively, and will be discussed in more detail in the next sections. The Richardson-Lucy image restoration algorithm has been extensively used in astronomy [65] and acoustic beamforming in the past [17, 1, 64, 28], and is based on assigning the meaning of a conditional probability to the PSF. The inversion method uses Bayes' theorem to find the inverse conditional probability $\mathcal{S}(\xi|x, \omega)$. The R-L is implemented following the guidelines of Ref. [17].

It is important to stress that even when utilizing these deconvolution approaches or when using optimized array geometries, the resolution that one obtains might still not be enough to fully characterize aeroacoustic sources of interest due to the limitations on the number of microphones used. Thus, other approaches such as continuous-scan techniques or non-synchronous measurements have been explored during the last years to improve beamforming resolution. These approaches can also be combined with deconvolution to obtain very highly-resolved noise source maps. It will be demonstrated how the continuous-scan paradigm attains high spatial resolutions through tailored signal processing guidelines that increase the number of closely-located microphones, thus reducing the degree of spatial aliasing compared to the use of arrays with fixed sensors only.

2.5 Continuous-Scan Beamforming

There has recently been a surge in interest in sensor arrays with both fixed and continuously-scanning sensors. The technique can be considered to be an extension of Lee's start-and-stop method [21], which is employed in Near-Field Acoustic Holography (NAH). The continuous-scan paradigm has been shown to improve the spatial resolution of the noise source maps for a fixed sensor count [1], and has recently found applications in order tracking [66], NAH [23], and beamforming [1, 27, 25]. The methodology has been shown to be ideal for microphone arrays that contain a low number of sensors, where their geometrical properties are highly constrained by the low number of sensors used. These sparse array configurations suffer from high sidelobe contamination and are unable to obtain resolved images of relevant aeroacoustic sources [1, 27].

2.5.1 Signal Division

A naive extension of the DAS method to continuous-scan phased arrays could use Eq. 2.3 with source-sensor propagating times that are time-varying. This is

$$s(\xi, t) = \sum_{m=1}^{\mathcal{M}_f+\mathcal{M}_s} w_m p_m(t + \tau_m(\xi, t)) \tag{2.16}$$

However, attention must be paid in these additional time-varying dependencies that arise due to the motion of the sensors when extending the DAS method to arrays containing scanning microphones. For a scanning sensor, the signal $p_m(t)$ is non-stationary, as described above. Thus, the expression for the source-sensor propagation time of Eq. 2.4 is no longer valid. Quasi-stationarity is sought by dividing the signal into a number K of overlapping or non-overlapping blocks of duration T (see Fig. 2.5), similar to the approach of Ref. [1]. Considering an array with $\mathcal{M}_f$ fixed and $\mathcal{M}_s$ scanning microphones, division of the signal into K blocks can be thought of as increasing the sensor count to $\mathcal{M}_f + K\mathcal{M}_s$. However, it is immediately obvious that not all of these sensors can be correlated. In particular, the signals of a given scanning sensor at different blocks (different spatial positions) are asynchronous and thus cannot be related. When considering the CSM based on the sensor count $\mathcal{M}_f + K\mathcal{M}_s$, the matrix has missing entries, hence is incomplete. This section will outline three distinct ways to compute the noise source maps from phased arrays that comprise fixed and scanning sensors. Two of such approaches will intend to obtain a CSM that is representative of the complete experiment run.

Division of the signal into a K number of blocks allows to use a few geometrical approximations, provided the block length T (in seconds) is sufficiently small. A first-order Taylor series expansion is used to approximate the source-sensor travel time and source-sensor distance for block k as

$$\begin{aligned} \ell_m(\xi, t) &\approx \ell_{mk}(\xi) \\ \tau_m(\xi, t) &\approx \tau_{mk}(\xi) + \left.\frac{\partial \tau_m(\xi, t)}{\partial t}\right|_{t=t_k} (t - t_k) \end{aligned} \tag{2.17}$$

where t_k is the center time of the block, and $\tau_{mk}(\xi)$ and $\ell_{mk}(\xi)$ are the source-sensor travel time and the source-sensor distance, respectively, calculated from the spatial center of the block. It can be shown that for a microphone array similar to that depicted in Fig. 2.6, the derivative of the source-sensor propagation time can be written as

$$\left.\frac{\partial \tau_m(\xi, t)}{\partial t}\right|_{t=t_k} = \frac{V_{mk}}{a_\infty} \frac{(x_{mk} - \xi)\cos\beta - y_{mk}\sin\beta}{\ell_{mk}(\xi)} = \alpha_{mk}(\xi) \tag{2.18}$$

where V_{mk} is the velocity of scanning sensor m for block k, thus allowing for the possibility of position-dependent sensor speeds, (x_{mk}, y_{mk}) are the coordinates of the scanning sensor at the geometric center of the block, and β is the array inclination.

Thus, Eq. 2.16, which was no longer valid within the continuous-scan paradigm, can now be approximated for every block k as

$$s_k(\xi, t) = \sum_{m=1}^{\mathcal{M}_f + \mathcal{M}_s} w_{mk} p_{mk}\Big((1 + \alpha_{mk}(\xi))t + \tau_{mk}(\xi)\Big) \tag{2.19}$$

where $p_{mk}(t)$ is the pressure recorded by sensor m at block k, and w_{mk} is the microphone weight, similar to that introduced for fixed-reference DAS.

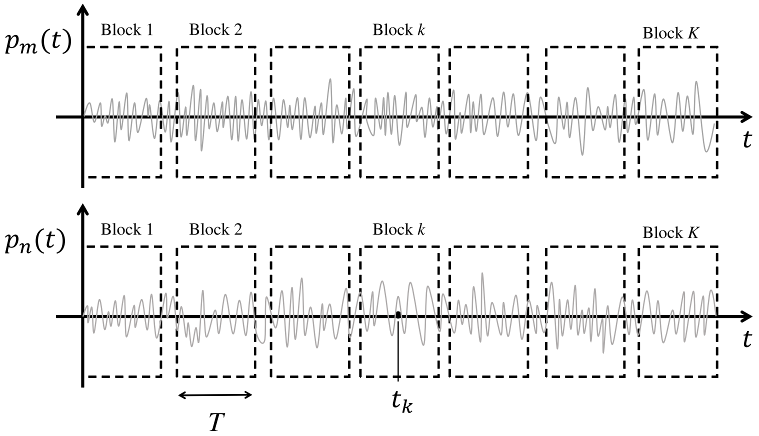

Figure 2.5: Illustration of the division of the signal into K quasi-stationary blocks without block overlap.

Finding the noise source map involves taking the Fourier transform of Eq. 2.19 and multiplying it by its complex conjugate. However, the issue requires special attention, as one must deal with auto- and cross-spectral densities of non-stationary signals. As such, special spectral estimation techniques must be used to handle such cross-spectral densities. The way in which the signal non-stationarity affects the beamforming results is derived explicitly in the next section, and methods will be proposed to mitigate its worst effects.

2.5.2 Signal Non-Stationarity

There exist several methods to estimate the auto- and cross-spectral densities of non-stationary signals. One of the most popular techniques is the short-term periodogram. The method consists of dividing the signal into smaller blocks and performing a short-time periodogram analysis (i.e., a Short Time Fourier Transform (STFT) is applied). Downsides of the technique include that the time-varying spectra are highly dependent on the block size that is selected, and that there is no guidance with regards to the signal division. In addition, the technique is unable to quantify the non-stationarity of the signal itself, and thus becomes useless if one tries to minimize it. Papamoschou *et al.* [1] identified the Wigner-Ville spectral

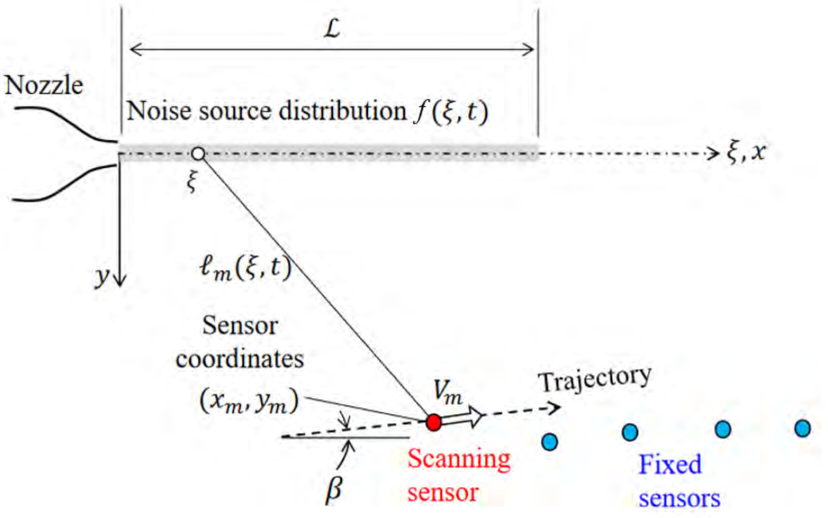

Figure 2.6: Line source distribution and far-field microphone array containing fixed microphones and one scanning sensor.

estimator as one of the most robust ways to handle the correlation of non-stationary signals in the context of continuous-scan beamforming. A similar development is presented next.

Considering two random signals $u(t)$ and $v(t)$, their symmetric cross-correlation is defined as

$$R_{u,v}(t,\tau) = \Big\langle u\Big(t+\frac{\tau}{2}\Big)v^*\Big(t-\frac{\tau}{2}\Big)\Big\rangle \tag{2.20}$$

where $\langle\ \rangle$ is used to denote the expected value (ensemble average), and the symbol $*$ denotes the complex conjugate, thus allowing the signals to be complex. The cross-Wigner-Ville spectrum (XWVS) for two random variables is defined as the Fourier transform of the symmetric cross-correlation

$$G_{u,v}(t,\omega) = \int_{-\infty}^{\infty} R_{u,v}(t,\tau)e^{-i\omega\tau}d\tau \tag{2.21}$$

Obviously, the auto-Wigner-Ville spectrum is obtained if the two random variables are the same. On defining the quantity

$$\beta_{mk}(\xi) = 1 - \alpha_{mk}(\xi) \tag{2.22}$$

where $\alpha_{mk}(\xi)$ is defined in Eq. 2.18, the symmetric cross-correlation of the scanning microphones pressure signals $p_m(t)$ and $p_n(t)$ for block k is written as

$$\begin{aligned}\Big\langle p_{mk}\Big(t + \frac{\tau}{2}\Big)p^*_{nk}\Big(t - \frac{\tau}{2}\Big)\Big\rangle &= \int_{\mathcal{L}}\int_{\mathcal{L}} \frac{1}{\ell_{mk}(\xi)\ell_{nk}(x)}\Big\langle f\Big(\xi, \beta_{mk}(\xi)[t + \tau/2] - \tau_{mk}(\xi)\Big) \\ &\times f^*\Big(x, \beta_{nk}(x)[t - \tau/2] - \tau_{nk}(x)\Big)\Big\rangle dx d\xi\end{aligned} \tag{2.23}$$

Using the definition from Eq. 2.21, the XWVS is calculated as

$$G_{mnk} = \int_{-\infty}^{\infty} \Big\langle p_{mk}\Big(t + \frac{\tau}{2}\Big)p^*_{nk}\Big(t - \frac{\tau}{2}\Big)\Big\rangle e^{-i\omega\tau} d\tau \tag{2.24}$$

On defining two new variables

$$\begin{aligned}t' &= \beta_{nk}(\xi)[t - \tau/2] - \tau_{nk}(\xi) \\ \tau' &= t[\beta_{mk}(\xi) - \beta_{nk}(\xi)] + \frac{\tau}{2}[\beta_{mk}(\xi) + \beta_{nk}(\xi)] + \tau_{nk}(\xi) - \tau_{mk}(\xi)\end{aligned} \tag{2.25}$$

the XWVS becomes

$$\begin{aligned}G_{mnk} &= \int_{-\infty}^{\infty}\int_{\mathcal{L}}\int_{\mathcal{L}} \frac{1}{\ell_{mk}(\xi)\ell_{nk}(x)}\Big\langle f\Big(\xi, t' + \tau'\Big) f^*\Big(x, t'\Big)\Big\rangle e^{-i\omega\tau'} dx d\xi d\tau' \\ &= \int_{\mathcal{L}}\int_{\mathcal{L}} \frac{2F(\xi, x, \omega'_{mnk})}{\ell_{mk}(\xi)\ell_{nk}(x)[\beta_{mk}(\xi) + \beta_{nk}(x)]} \times \exp\Big(i\omega'_{mnk}[\tau_{nk}(x) - \tau_{mk}(\xi)]\Big) \\ &\times \exp(i\omega''_{mnk}t) dx d\xi d\tau'\end{aligned} \tag{2.26}$$

where

$$F(\xi, x, \omega) = \int_{-\infty}^{\infty} \Big\langle f\Big(\xi, t + \tau\Big) f^*\Big(x, t\Big)\Big\rangle e^{-i\omega\tau} d\tau \tag{2.27}$$

is the source cross-spectral density, as denoted in Eq. 2.13. The source cross-spectral density is a fundamental relationship that is used to model the source distribution in spectral estimation methods.

An important observation derived from Eq. 2.26 is that the source spectral density, which is what beamforming aims at obtaining, is affected by two parameters that are a direct consequence of the motion of the sensor. First, a Doppler-shifted frequency ω'_{mnk} appears in the source cross-spectral density and the steering vectors. Reference [1] approximated $F(\xi, x, \omega'_{mnk}) \approx F(\xi, x, \omega)$ with little loss in accuracy provided that the sensor scan speed was sufficiently low. A similar approach is followed in the present work. The Doppler-shifted frequency is given by

$$\omega'_{mnk} = \omega \frac{2}{\beta_{mk}(\xi) + \beta_{nk}(\xi)} \tag{2.28}$$

and will explicitly appear in the derivation of the equations for the Cross-Spectral Submatrices (CSSM) method.

The second parameter affecting the source distribution is a frequency of oscillation of the entire spectrum ω''_{mnk}. This effect worsens as the frequency increases, requiring modification in the way the cross- and auto-spectral densities are handled. The expression for the frequency of oscillation is

$$\omega''_{mnk} = \omega'_{mnk}[\beta_{mk}(\xi) - \beta_{nk}(x)] \tag{2.29}$$

which can be approximated as [1]

$$\omega''_{mnk} \approx \omega \Big(\frac{V_{nk}}{a_\infty} cos(\theta_{nk}(x)) - \frac{V_{mk}}{a_\infty} cos(\theta_{mk}(\xi)) \Big) \tag{2.30}$$

Note that if the WVS was not used and one instead utilized the short-term periodogram

(STFT) approach, these exact effects of the signal non-stationarity could have not been quantified. Suppression of non-stationarity, assuming that only one sensor is scanning, requires $|\omega''_{mnk}T/2| << 1$. It can be demonstrated that the oscillation is suppressed [1] when

$$V_{mk}T << \lambda \tag{2.31}$$

where V_{mk} is the velocity of the scanning sensor, T is the duration of the block in seconds, and λ is the acoustic wavelength that is being resolved. The above relation implies that as the frequency resolved rises, the block size must be decreased to suppress the non-stationarity. However, selecting a block time for each wavelength is not feasible as it incurs into increased comptational time to compute the noise source maps. Instead, Ref. [1] suggested using a frequency-dependent window that acts as a filter on the block length. The authors utilized a Gaussian window that was energy-conserving, with the latter condition expressed as

$$\int_{-T/2}^{T/2} |b(\omega, t)|^2 dt = T \tag{2.32}$$

where $b(\omega, t)$ is the frequency-dependent function. The expression for the energy-conserving Gaussian window is

$$b(\omega, t) = A(\omega) f_w(\omega, t) = \Big(\frac{2}{\pi}\Big)^{1/4} \sqrt{\frac{T}{\delta(\omega)} \frac{1}{\mathrm{erf}\frac{T}{\sqrt{2}\delta(\omega)}}} \times \exp\Big[-\Big(\frac{t}{\delta(\omega)}\Big)^2\Big] \tag{2.33}$$

where $A(\omega)$ is the parameter to ensure energy conservation, $f_w(\omega, t)$ is the shape of the window, and $\delta(\omega)$ is the tuning parameter of the Gaussian window. Equation 2.31 can be expressed as

$$V_{mk}\delta(\omega) = c_\lambda \lambda \tag{2.34}$$

where c_λ is the fraction of the acoustic wavelength that the scanning sensor traverses with time $\delta(\omega)$. Ref. [1] proposed applying the Gaussian window in combination with the computation of the cross-spectral densities between microphones that had a relative velocity. Their work demonstrated how the non-stationarity could be minimized with the Gaussian filter, and the source distribution could be recovered at high frequency.

In addition to the frequency-dependent Gaussian of Ref. [1], this work also explored a hyperbolic secant and a Cauchy distribution as potential function shapes. However, it was found that the outcomes were mainly unaffected by the shape of the function used. The expressions for the frequency-dependent windows are summarized in Table 2.1 for completeness.

	$A(\omega)$	$f_w(\omega, t)$
Gaussian	$\left(\frac{2}{\pi}\right)^{1/4}\sqrt{\frac{T}{\delta(\omega)}\frac{1}{\operatorname{erf}\frac{T}{\sqrt{2}\delta(\omega)}}}$	$\exp\left[-\left(\frac{t}{\delta(\omega)}\right)^2\right]$
Hyperbolic Secant	$\sqrt{\frac{k(\omega)T}{2\tanh(k(\omega)T/2)}}$	$\operatorname{sech}(k(\omega)t)$
Cauchy distribution	$\sqrt{1/\left(\frac{2}{(\sqrt{k(\omega)}T)^2+4}+\frac{\tan^{-1}(\sqrt{k(\omega)}T/2)}{\sqrt{k(\omega)}T}\right)}$	$\frac{1}{k(\omega)t^2+1}$

Table 2.1: Expressions for the frequency-dependent windows.

The tuning parameter for the hyperbolic secant and the Cauchy distribution is $k(\omega)$, with

$$V_{mk}T = k(\omega)\lambda \tag{2.35}$$

The parameter $k(\omega)$ represents the number of wavelengths λ traversed by a scanning sensor with velocity V_{mk} for block duration T. An example of the energy-conserving frequency-dependent windows is shown in Fig. 2.7. A block size of $\sim$ 0.56 seconds was used. The block center is located at $t = 0$ and $k(\omega) = 5$. Notice how all windows are continuous and how they are relatively similar in their filtering nature.

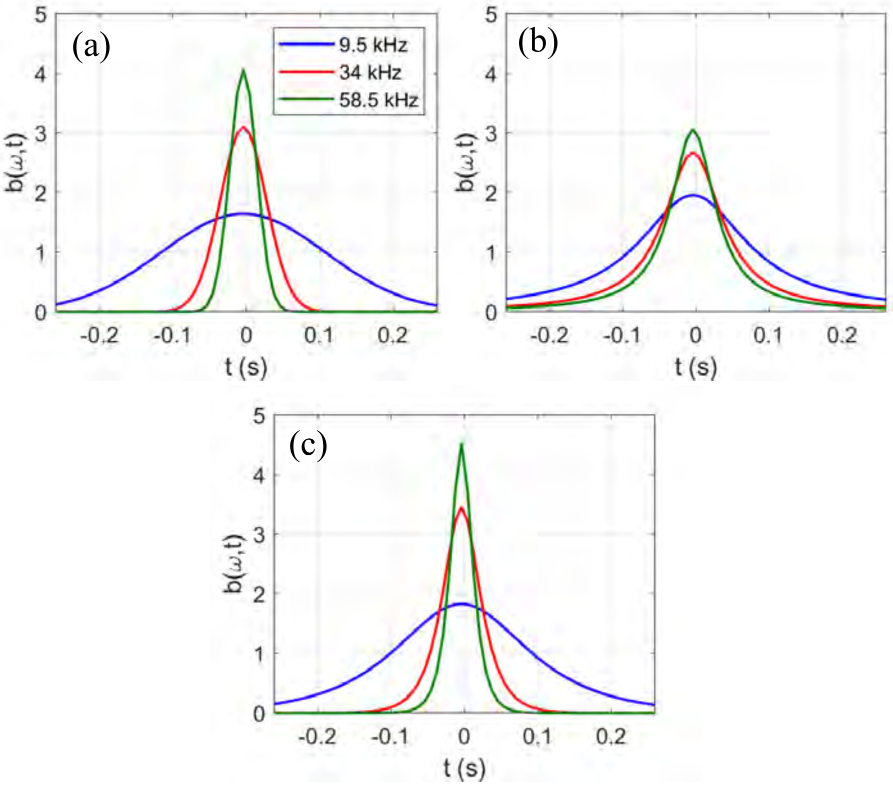

Figure 2.7: Frequency-dependent windows. (a) Gaussian; (b) Cauchy distribution; and (c) Hyperbolic secant.

The extensions of the beamforming technique to the continuous-scan paradigm must be necessarily informed by these non-stationarity observations, including the division of the signal into smaller, quasi-stationary blocks and the application of a frequency-dependent window to suppress its worst effects. The signal non-stationarity results in a special signal processing that affects the quality of the noise source maps. This will be explored in detail in Chapter 3. A schematic of the window width reduction with frequency is depicted in in Fig. 2.8.

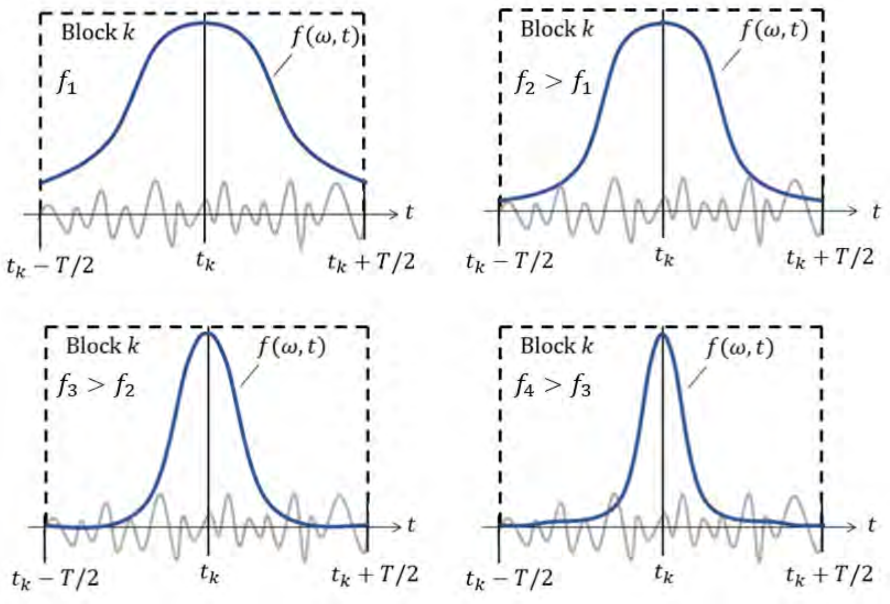

Figure 2.8: Schematic of the Gaussian window width reduction with increasing frequency.

2.5.3 Beamforming using Cross-Spectral Submatrices

Finding the noise source map involves taking the Fourier transform of Eq. 2.19 and multiplying it by its complex conjugate while considering the windowing process that has been previously described. The Fourier transform of Eq. 2.19 is written as

$$S_k(\xi,\omega) = \int_{-\infty}^{\infty} \sum_{m=1}^{\mathcal{M}_f+\mathcal{M}_s} w_{mk}\; p_{mk}[(1+\alpha_{mk}(\xi))t + \tau_{mk}(\xi)]\; e^{-i\omega t} dt \tag{2.36}$$

Using the properties of the Fourier Transform, Eq. 2.36 can be transformed into

$$S_k(\xi,\omega) = \sum_{m=1}^{\mathcal{M}_f+\mathcal{M}_s} \frac{w_{mk}}{1+\alpha_{mk}(\xi)}\; P_{mk}(\omega'_{mk}(\xi))\; e^{-i\omega'_{mk}\tau_{mk}(\xi)} \tag{2.37}$$

where $P_{mk}(\omega'_{mk}(\xi))$ is the Fourier transform of $p_{mk}(t)$. Notice that the quantity $\omega'_{mk}(\xi)$ appears. This variable is the Doppler-shifted frequency that arises due to the motion of the sensor [1], as was previously introduced, and was expected to rise in the analysis. Its exact expression is

$$\omega'_{mk}(\xi) = \frac{\omega}{1 + \alpha_{mk}(\xi)} \tag{2.38}$$

For low scan Mach number (i.e. $V_{mk}/a_{\infty} << 1$), the Fourier transform of the pressure signal $P_{mk}(\omega'_{mk}(\xi))$ can be approximated as $P_{mk}(\omega)$ with little error.

The Fourier transform of the summation of all microphone signals (fixed and scanning) for block k can then be approximated as

$$S_k(\xi, \omega) = \sum_{m=1}^{\mathcal{M}_f + \mathcal{M}_s} \frac{w_{mk}}{1 + \alpha_{mk}(\xi)} \; P_{mk}(\omega) \; e^{-i\omega'_{mk}\tau_{mk}(\xi)} \tag{2.39}$$

On defining the continuous-scan microphone weight

$$W_{mk} = \frac{w_{mk}}{1 + \alpha_{mk}(\xi)} \tag{2.40}$$

the Fourier transform of the summation of all microphone signals for a block k becomes

$$S_k(\xi, \omega) = \sum_{m=1}^{\mathcal{M}_f + \mathcal{M}_s} W_{mk} \; P_{mk}(\omega) \; e^{-i\omega'_{mk}\tau_{mk}(\xi)} \tag{2.41}$$

To find the noise source map for block k, one needs to multiply Eq. 2.41 by its complex conjugate, which includes the averaging involved in the FFT algorithm, and the application of the frequency-dependent window when estimating the spectral densities between sensors that have a relative velocity

$$Y_k(\xi, \omega) = \sum_{m=1}^{\mathcal{M}_f + \mathcal{M}_s} \sum_{m=1}^{\mathcal{M}_f + \mathcal{M}_s} W_{mk} W_{nk} \; \overline{P_{mk}(\omega) P^*_{nk}(\omega)} \; e^{-i\omega'_{mk}(\xi)\tau_{mk}(\xi)} \; e^{i\omega'_{nk}(\xi)\tau_{nk}(\xi)} \tag{2.42}$$

On defining the CSM for block k as

$$C_k(\omega) = \overline{P_{mk}(\omega) P^*_{nk}(\omega)} \tag{2.43}$$

which has a size of $(\mathcal{M}_f + \mathcal{M}_s) \times (\mathcal{M}_f + \mathcal{M}_s)$ and includes the windowing process as outlined in Ref. [1], the array output for block k can be computed as

$$Y_k(\xi,\omega) = \mathbf{g}(\xi,\omega)\ \mathbf{C_k}(\omega)\ \mathbf{g^H}(\xi,\omega) \tag{2.44}$$

where the steering vector is defined as

$$\begin{aligned}\mathbf{g}(\xi,\omega)\ =&[W_{1k} e^{-i\omega'_{1k}(x)\tau_{1k}(\xi)} \quad W_{2k} e^{-i\omega'_{2k}(\xi)\tau_{2k}(\xi)} \quad \dots \\ & W_{(\mathcal{M}_f+\mathcal{M}_s)k} e^{-i\omega'_{(\mathcal{M}_f+\mathcal{M}_s)k}(\xi)\tau_{(\mathcal{M}_f+\mathcal{M}_s)k}(\xi)}]\end{aligned} \tag{2.45}$$

Analogous to the procedure performed for the fixed-reference DAS discussed in Section 2.3, one can attempt to eliminate the microphone self-noise contamination and improve the dynamic range of the array by removing the diagonal from the block-CSMs

$$Y_k(\xi,\omega) = \mathbf{g}(\xi,\omega)\ \mathbf{C}_{\text{diag}=0,k}(\omega)\ \mathbf{g}^H(\xi,\omega) \tag{2.46}$$

However, the cautionary comment noted before should be remembered when removing the diagonal elements.

The past paragraphs have described how to find the array power response for a block k. However, care must be taken in assembling the responses over all the blocks, to include only the distinct elements of the CSSMs (Eq. 2.43) as to avoid averaging of repeated information. Methodologies using direct spectral estimation [1, 27] have addressed this issue by breaking down the CSM into a number of cross-spectral submatrices (CSSMs), one for each block k, with $k = 0$ comprising the correlations between the fixed sensors only, calculated using the full duration of the pressure signals. A similar approach is employed here to calculate the DAS noise source map.

As an example, assume that two microphones are scanning and five microphones are fixed. The CSSMs are organized such that the first two rows and columns always contain the contributions involving the scanning sensors. This is highlighted in pink in the figure. The contributions from the fixed sensors are highlighted in blue. Only the bold elements are used to produce the DAS noise source map, as they contain non-repeated information for each block. This is illustrated in Fig. 2.9

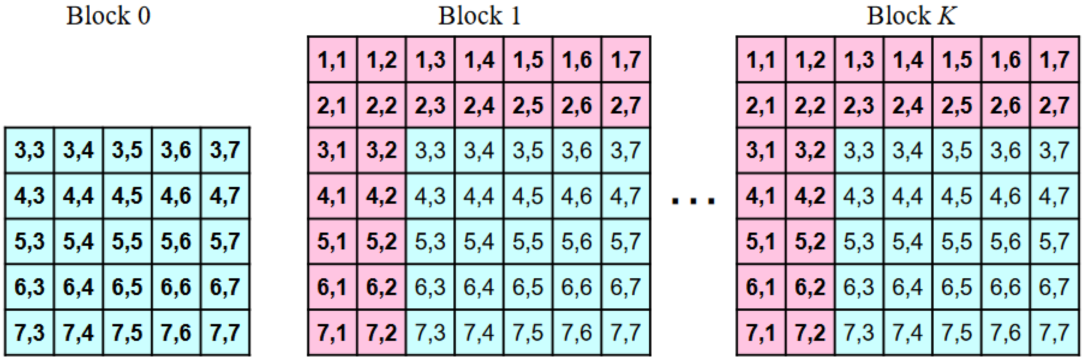

Block 0

3,3	**3,4**	**3,5**	**3,6**	**3,7**
4,3	**4,4**	**4,5**	**4,6**	**4,7**
5,3	**5,4**	**5,5**	**5,6**	**5,7**
6,3	**6,4**	**6,5**	**6,6**	**6,7**
7,3	**7,4**	**7,5**	**7,6**	**7,7**

Block 1

1,1	**1,2**	**1,3**	**1,4**	**1,5**	**1,6**	**1,7**
2,1	**2,2**	**2,3**	**2,4**	**2,5**	**2,6**	**2,7**
3,1	**3,2**	3,3	3,4	3,5	3,6	3,7
4,1	**4,2**	4,3	4,4	4,5	4,6	4,7
5,1	**5,2**	5,3	5,4	5,5	5,6	5,7
6,1	**6,2**	6,3	6,4	6,5	6,6	6,7
7,1	**7,2**	7,3	7,4	7,5	7,6	7,7

...

Block K

1,1	**1,2**	**1,3**	**1,4**	**1,5**	**1,6**	**1,7**
2,1	**2,2**	**2,3**	**2,4**	**2,5**	**2,6**	**2,7**
3,1	**3,2**	3,3	3,4	3,5	3,6	3,7
4,1	**4,2**	4,3	4,4	4,5	4,6	4,7
5,1	**5,2**	5,3	5,4	5,5	5,6	5,7
6,1	**6,2**	6,3	6,4	6,5	6,6	6,7
7,1	**7,2**	7,3	7,4	7,5	7,6	7,7

Figure 2.9: Illustration of the CSSMs for two scanning sensors (1-2) and 5 fixed sensors (3-7). Non-repeated elements are indicated in bold font.

It is easy to show that the number of non-repeating elements used to compute the noise source map is then

$$J = (\mathcal{M}_f - \mathcal{M}_s)^2 + (K-1)\mathcal{M}_s(2\mathcal{M}_f - \mathcal{M}_s) \tag{2.47}$$

When the diagonal is removed from the CSM, the number of elements is

$$J = (\mathcal{M}_f - \mathcal{M}_s)^2 - (\mathcal{M}_f - \mathcal{M}_s) + (K-1)\mathcal{M}_s(2\mathcal{M}_f - \mathcal{M}_s - 1) \tag{2.48}$$

Note that if the DiRec method is used to mitigate the microphone self-noise contamination on a block by block basis, the number of total elements is that of Eq. 2.47. On defining

$$B_{mn} = w_m w_n$$

and

$$T_{mn,k} = W_{mk} W_{nk}$$

the contributions from block 0 are

$$\sum_{m=\mathcal{M}_s+1}^{\mathcal{M}_f+\mathcal{M}_s} \sum_{n=\mathcal{M}_s+1}^{\mathcal{M}_f+\mathcal{M}_s} B_{mn}\ C_{mn}(\omega)\ e^{i\omega\tau_m(\xi)}\ e^{-i\omega\tau_n(\xi)}$$

The contributions of the first two rows (Fig. 2.9) of a CSSM k are

$$\sum_{m=1}^{\mathcal{M}_s} \sum_{n=1}^{\mathcal{M}_f+\mathcal{M}_s} T_{mn,k}\ C_{mn,k}(\omega)\ e^{i\omega'_{mk}(\xi)\tau_{mk}(\xi)}\ e^{-i\omega'_{nk}(\xi)\tau_{nk}(\xi)}$$

and those of the first two columns, excluding the elements previously accounted for, are

$$\sum_{m=\mathcal{M}_s+1}^{\mathcal{M}_s+\mathcal{M}_f} \sum_{n=1}^{\mathcal{M}_s} T_{mn,k}\ C_{mn,k}(\omega)\ e^{i\omega'_{mk}(\xi)\tau_{mk}(\xi)}\ e^{-i\omega'_{nk}(\xi)\tau_{nk}(\xi)}$$

Then, the expression for the noise source map obtained with the CSSM approach is

$$\begin{aligned} Y(\xi,\omega) = \frac{1}{J}\Bigg(& \sum_{m=\mathcal{M}_s+1}^{\mathcal{M}_f+\mathcal{M}_s} \sum_{n=\mathcal{M}_s+1}^{\mathcal{M}_f+\mathcal{M}_s} B_{mn}\ C_{mn}(\omega)\ e^{i\omega\tau_m(\xi)}\ e^{-i\omega\tau_n(\xi)} \\ & \sum_{k=1}^{K} \Bigg[\sum_{m=1}^{\mathcal{M}_s} \sum_{n=1}^{\mathcal{M}_f+\mathcal{M}_s} T_{mn,k}\ C_{mn,k}(\omega)\ e^{i\omega'_{mk}(\xi)\tau_{mk}(\xi)}\ e^{-i\omega'_{nk}(\xi)\tau_{nk}(\xi)} + \\ & \sum_{m=\mathcal{M}_s+1}^{\mathcal{M}_s+\mathcal{M}_f} \sum_{n=1}^{\mathcal{M}_s} T_{mn,k}\ C_{mn,k}(\omega)\ e^{i\omega'_{mk}(\xi)\tau_{mk}(\xi)}\ e^{-i\omega'_{nk}(\xi)\tau_{nk}(\xi)} \Bigg] \Bigg) \end{aligned} \tag{2.49}$$

The equation constitutes the extension of the DAS methodology to the continuous-scan paradigm, here referred to as CSSM. Note that the first term of the equation uses only the fixed sensors; as such, the frequency is not influenced by the Doppler-shift. The spatial resolution of the noise source map is significantly increased when using the CSSM technique over fixed reference DAS, as will be demonstrated in the Chapter 5. However, one of the principal drawbacks of the CSSM approach is the lack of a global CSM. Deconvolution (DAMAS, DAMAS2, CLEAN-SC, R-L, etc.) and advanced beamforming approaches (Orthogonal Beamforming, Functional Beamforming, etc.) are based on having a global CSM. As such, it is highly desirable to obtain a global CSM that is representative of the complete experimental run. Two new methods are introduced with this regard: a Cross-Spectral Matrix Completion process and a Partial Fields Decomposition technique.

2.5.4 Matrix Completion Techniques

As stated earlier, the lack of a global CSM when using the CSSM technique makes it impossible to utilize advanced beamforming and deconvolution approaches. This section explores the possibility of obtaining a global CSM through interpolation and a matrix completion process that bears similarities to the matrix completion technique that is used in other beamforming fields [67].

Considering an array with $\mathcal{M}_f$ fixed and $\mathcal{M}_s$ scanning microphones, division of the signal into K blocks can be thought of as increasing the sensor count to $\mathcal{M}_f + K\mathcal{M}_s$ as stated previously. However, it is immediately obvious that not all of these sensors can be correlated. When considering the cross-spectral matrix (CSM) based on the sensor count $\mathcal{M}_f + K\mathcal{M}_s$, the matrix has missing entries, which is illustrated in the example of Fig. 2.10a. As an example, the figure assumes an array with three microphones that are fixed and one microphone that is scanning. The signal of the scanning microphone is divided into six blocks. Treating the position of the scanning microphone as a “virtual” sensor, one is tempted to construct a 9 × 9 cross-spectral matrix. Auto- and cross-correlations are possible between the fixed microphones, between the scanning and fixed microphones, and the scanning sensor with itself at a given block. However, correlations of the scanning sensor at different blocks are not possible. These are indicated by the blank entries in Fig. 2.10a. This section attempts at completing the missing entries of the global CSM.

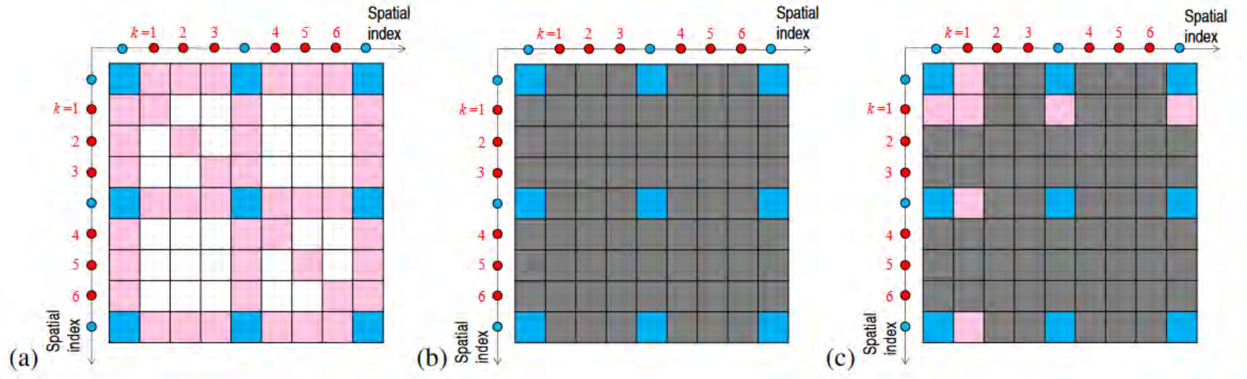

Figure 2.10: (a) Cross-spectral matrix for an array with three fixed microphones and one scanning sensor whose output is divided into six blocks. The correlations involving fixed sensors only are highlighted in blue, while those involving fixed and scanning sensors are indicated in red. Blank entries indicate missing elements. (b) Submatrix for block 0. (c) Submatrix for block 1.

UPAINT Method

An interpolation approach to construct a global CSM was explored as a first approximation in this work. In particular, a methodology similar to the array interpolation approach of Ref. [68] was tested on real supersonic and subsonic jet flow data.

Array interpolation methods have been used in the past to improve signal to noise ratio [69] or replace faulty microphones [70]. These methods have also been used to extend the spatial bandwidth of microphone arrays, thus reducing sidelobe contamination [68]. The present work explored the possibility of using the Unwrapped Phased Array Interpolation (UPAINT) of Goates *et al.* [68] within the continuous-scan paradigm. The technique interpolates the

CSM magnitude and phase for each frequency, thus allowing to virtually increase the number of references. The process involved in the UPAINT approach is briefly summarized.

The first step in the UPAINT method extended to the continuous-scan approach is the division of the signal into a number of K quasi-stationary blocks, and the computation of the cross-spectral densities between fixed sensors pairs, and fixed sensors and the distinct blocks, and the auto-spectral density of each block. As outlined earlier, the cross-spectral densities between the blocks cannot be calculated as the measurements have been performed asynchronously, and one obtains a CSM with missing entries (Fig. 2.10a). The entries of the CSM are sorted according to a spatial index such as the polar angle to allow proper interpolation of neighboring microphone correlations. The matrix containing the missing entries is referred to as $\mathbf{C}_{missing}$.

The second step in the UPAINT process is to obtain the phase and amplitude of the CSM. The amplitude of the CSM is denoted by $|\mathbf{C}_{missing}|$ while the phase is referred to by $\mathbf{\Phi} = \arg(\mathbf{C}_{missing})$.

A general issue of the approach is that $\mathbf{\Phi}$ might contain 2π discontinuities if the phase is wrapped. This can easily be overcome if the phase of the known cross-spectral densities is unwrapped as

$$\tilde{\Phi}_{mn}(\omega) = \Phi_{mn} + 2\pi\Lambda(\omega) \tag{2.50}$$

where $\tilde{\Phi}_{mn}(\omega)$ is the phase unwrapping for microphones m and n and $\Lambda(\omega)$ is an integer. The frequency at which the phase discontinuity occurs is highly dependent on the source emission pattern and the microphone spacings. The phase unwrapping constitutes the third step in applying the UPAINT method to continuous-scan beamforming.

After the phase is unwrapped, the missing entries are estimated by 2-D interpolation of the magnitude and phase of $|\mathbf{C}|$ and $\tilde{\Phi}(\omega)$, respectively, constituting the fourth and final step in the process.

Although the method has been successfully applied in past beamforming studies [68], it failed at providing an accurate estimate of the missing block correlations at high frequencies. This is due to the relationship of Eq. 2.50 not being perfectly linear. An example of this behavior is shown in Fig. 2.11. The images were obtained using far-field microphones with different spacings for the isolated supersonic jet flow experiments presented in this work. It is seen how the relationship of Eq. 2.50 fails to hold as the frequency increases, resulting in penalizations in the spatial resolution of the noise source map which is obtained when the interpolated CSM is steered to the region of interest. As such, beamforming results utilizing the UPAINT technique will not be shown in Chapter 5.

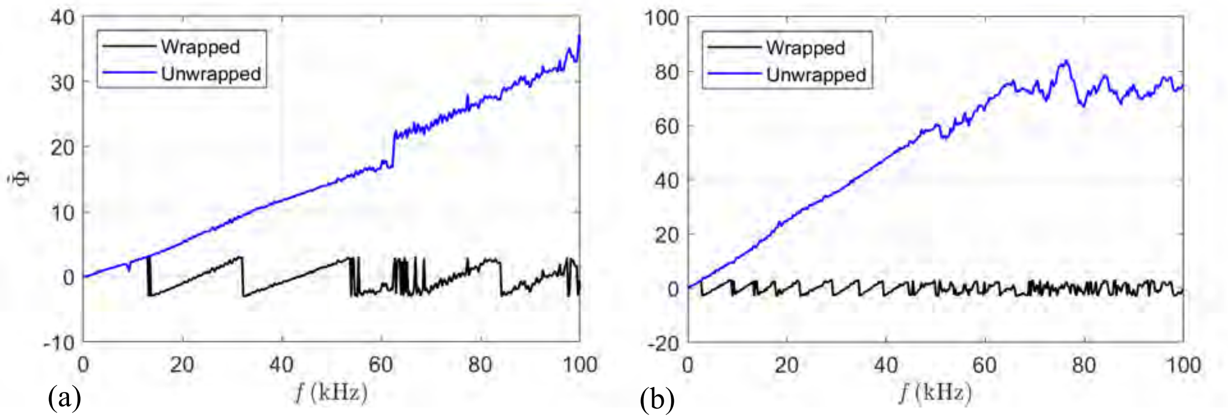

Figure 2.11: Wrapped and unwrapped phased between cross-spectral densities of microphones with spacings of (a) 0.06 m and (b) 0.22 m.

Cross-Spectral Matrix Completion

The second matrix completion technique (CSMC) utilized in this work bears similarities to the matrix completion techniques used in non-synchronous microphone measurements. The study of noise source localization algorithms utilizing a set of non-synchronous microphone recordings has gained significant attention in recent years [71, 72, 73, 74, 75]. An initial approach consisted in moving a prototype array in a sequential manner to perform several measurements at different points. However, the phase correlations between the array's microphones at two independent sequential places were lost, resulting in a reduction in the spatial precision required for many beamforming applications (Fig. 2.10a). An early solution consisted in placing zeroes at the positions of the missing entries (those that related the array at two distinct positions). However, this procedure did not improve the spatial resolution of the beamformed maps [75].

Later, an approach consisting of installing reference microphones near the source was used as an approach to infer the missing relationships. Using conditioned spectral analysis and principal component analysis [76] in a technique akin to partial fields decomposition, such microphones were utilized to reconstruct the lost phase correlations between consecutive points of the array. However, in order to resolve the missing relationships accurately enough, a large number of reference sensors were often required to have independent recordings of large numbers of uncorrelated noise sources, such as those associated with the high frequencies of turbulence mixing noise or shock-associated noise, resulting in a prohibitive cost for several applications.

References [67, 76] proposed a novel method for determining missing relationships in sequential microphone measurements. The methodology was designed to complete a global CSM generated by non-synchronous microphone array measurements, which involved the estimation of the missing entries of a CSM. A similar undertaking has been adapted to the continuous-scan paradigm. The technique is briefly summarized in the next lines. The mathematical description is introduced next.

First, the signal from all microphones is divided into smaller, quasi-stationary blocks. A CSM is created by including the cross-spectral densities that relate scanning and fixed sensors. The spectral densities from the fixed microphones are also incorporated in the CSM. These utilize the full duration of the microphone pressure signals. Each fixed microphone and block correspond to a measurement taken at a distinct geometrical position. As such, it is advisable to organize the CSM according to a spatial index (e.g., the polar angle with respect to the noise source). The above process obtains a data-missing CSM. A schematic of the data-missing matrix obtained within the continuous-scan paradigm is shown in Fig. 2.12, where three microphones are fixed and the signal from one scanning sensor is divided into 6 blocks. The cross-spectral densities between the distinct blocks (i.e., the scanning sensor at distinct positions) are not readily available as the measurements have been taken asynchronously. The contributions from the fixed sensors are highlighted in blue, while those of the scanning sensor are highlighted in pink. Then, the missing entries of the CSM are estimated by using a minimization approach. This requires to assume and impose certain characteristics about the completed matrix that will be further discussed in this section. Additionally, the position of the microphones (and distinct blocks) must be encoded in the minimization algorithm to obtain physical results, as discussed by Yu *et al.* [67, 77, 71]. This is done by "filtering" the CSM using a spatial basis, which prevents neighboring cross-spectral densities, associated microphone pairs that are geometrically close, from being very different from each other. The completed CSM can be steered back to the region of interest using the steering vectors. Deconvolution can be used. The mathematical insights of the matrix completion process are discussed next.

The CSMC completion method is typically expressed as a matrix rank minimization problem (low rank model) with constraints. However, when dealing with signals produced by a large and unknown number of uncorrelated sources the process of estimating the rank of the completed matrix can be cumbersome without a priori information. Additionally, as discussed by Yu [67], the process of estimating the matrix rank poses a great challenge when dealing with signals with moderate to high levels of noise in the measurements, as might be the case in wind tunnel beamforming applications. If the matrix completion problem was formulated as a rank minimization process, one would be required to use an experimentally-

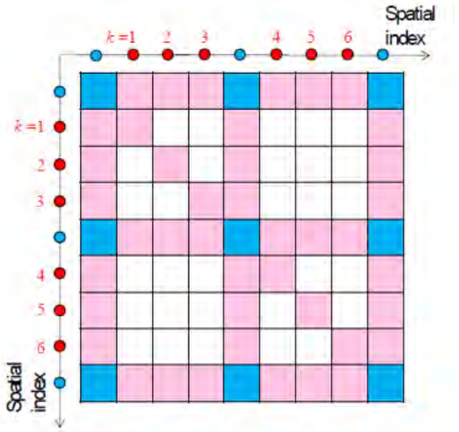

Figure 2.12: Schematic of a data-missing CSM within the continuous-scan paradigm; 3 microphones are fixed and the signal from one scanning sensor is divided into 6 blocks.

determined thresholding parameter related to the most relevant eigenvalues. The parameter would have to be linked to the most important uncorrelated acoustic sources. For instance, one could use the difference between consecutive eigenvalues values to inform the selection of the thresholding value. However, this would introduce a high degree of variability in the results. As a result, the low rank model is frequently restated as a weakly sparse eigenvalue spectrum problem. This also allows the use of advanced semidefinite programming (SDP) methods and libraries for convex optimization applications. In otherwords, it is here assumed that the completed CSM is of full rank and contains only a few dominant eigenvalues, rather than imposing a reduced fixed rank. The task of CSM completion can then be translated into a problem of minimizing the CSM nuclear norm, subject to some constraints. The CSM nuclear norm is defined as

$$\|\mathbf{C}_{completed}(\omega)\|_* = \sum_{i=1}^{\mathcal{M}_f+K\mathcal{M}_s} \lambda_i^2(\omega) \tag{2.51}$$

where λ_i are the eigenvalues. The requirements imposed to ensure a physical solution of the matrix completion process are discussed next.

The first restrictions imposed on the global CSM are the Hermitian and semipositive definite conditions. That is

$$\mathbf{C}_{completed}(\omega) = \mathbf{C}^{H}_{completed}(\omega) \tag{2.52}$$

and

$$\mathbf{C}_{completed}(\omega) \succeq 0 \tag{2.53}$$

respectively. This guarantees that there are no negative source auto-spectral densities, associated with negative eigenvalues, which is deemeded to be non-physical, as discussed in earlier sections. The Hermitian condition ensures that the resulting CSM is a suitable and realistic matrix within the context of beamforming.

The next condition is imposed such that the completed CSM does not modify the measured entries of the data-missing CSM, denoted by $\mathbf{C}_{missing}$. However, this requirement can be relaxed and stated as

$$\|\mathcal{A}(\mathbf{C}_{completed}(\omega)) - \mathbf{C}_{missing}(\omega)\|_F \leq \epsilon_1 \tag{2.54}$$

where the $\mathcal{A}(\cdot)$ operator only extracts the positions containing the measured cross- and auto-spectral densities of the data-missing CSM, $\|\cdot\|_F$ is the Frobenius norm, and ϵ_1 is a thresholding parameter that relaxes the modification constraint.

At this point, a CSM that is representative of the complete experiment run can be calculated with the above requirements. However, as discussed by Yu [67], the results might not necessarily be physical within the context of aeroacoustic applications. Yu argues that a new constraint must be introduced in order to ensure that the results are physical. This new constraint ensures the smoothness of the acoustic far-field by using a smoothing operator that encodes the positions of the microphones, including the fixed sensors and the center locations of the blocks where the “virtual microphones” are placed.

The operator essentially acts as a filter on the completed CSM, preventing significant variations in the auto- and cross-spectral densities in neighboring columns and rows, associated with microphones or “virtual microphones” that are placed close to each other. The filter is denoted by $\boldsymbol{\Psi}$ and can be constructed using a wide variety of basis functions. Hu *et al.* [74] discuss the influence of the use of distinct spatial basis functions on the errors in the estimation of the missing entries of the CSM. In particular, they use Generalized Harmonic Polynomials (GHPs), which are an approximate solution to the homogeneous Helmholtz equation in a star-convex domain and also utilize a set of plane wave functions. The present work uses a simpler version of the plane wave basis spatial filter, constructed using a dimension-reduced Fourier spatial basis. The Fourier spatial basis is constructed as

$$\boldsymbol{\Theta} = \exp\Big[i(k_x\mathbf{x} + k_y\mathbf{y})\Big] \tag{2.55}$$

where $\mathbf{x}$ and $\mathbf{y}$ represent the coordinates of the fixed sensors and center coordinates of the blocks, and $(k_x,\ k_y)$ are spatial wavenumbers. The wavenumbers are discretized as $k_x^n = n\Delta k_x$, with $n = -N, ..., N$, and similarly for k_y, with $k_y^m = m\Delta k_y$ and $m = -M, ..., M$, according to the guidance found in the work of Yu *et al.* [67]. Note that the expressions for k_y will not be explicitly written in this work given their similarity to those obtained for k_x. The maximum spatial frequency is obviously

$$k_{x,\max} = N\Delta k_x = \frac{\pi}{\Delta x} \tag{2.56}$$

Additionally, the spatial frequency can be linked to the aperture of the microphone array by $\Delta k_x = \frac{2\pi}{L_x}$, where L_x is the array aperture in the x direction, and similarly for M. The integer N is given by the expression

$$N = \frac{\pi}{\Delta x \Delta k_x} \tag{2.57}$$

Up to this point, no information with regards to the coordinate z has been given. The array used in this study consists of a one-dimensional distribution of microphones, inclined a certain angle with respect to the nozzle axis (see Fig. 2.6). The scanning microphone traverses in a line parallel to that formed by the fixed sensors and with a very small vertical offset. As such, this work assumes that the acoustic waves will not be significantly different within the small offset Δz between the fixed and scanning microphones.

The use of the spatial basis presented earlier is valid provided that the far-field correlation length, here denoted by ℓ_c, is larger than the average distance between two microphones or block centers. This poses a restriction in the position of sequential microphone measurements. However, within the context of the continuous-scan approach, the above statement poses a requirement in terms of the signal processing, implying that the blocks must be relatively close to each other. This will be discussed in more detail in the next section. A general rule to determine the minimum resolution of the Fourier spatial basis is

$$\Delta x, \Delta y \geq \min(\ell_c, 2d_c) \tag{2.58}$$

with d_c being the distance between two contiguous microphones or block centers. The smoothing filter is then constructed as

$$\boldsymbol{\Psi} = \boldsymbol{\Theta}\boldsymbol{\Theta}^{\dagger} \tag{2.59}$$

where $\boldsymbol{\Theta}^{\dagger}$ is the Moore-Penrose pseudo-inverse. The Moore-Penrose inverse is defined as

$\mathbf{\Theta}^{\dagger} = \mathbf{V\Sigma^{-1}U^{H}}$, where the rectangular diagonal matrix $\mathbf{\Sigma^{-1}}$ is

$$\mathbf{\Sigma}^{-1} = \begin{pmatrix} \sigma_{11}^{-1} & 0 & \cdots & 0 \\ 0 & \sigma_{22}^{-1} & \cdots & 0 \\ \vdots & \vdots & \ddots & \vdots \\ 0 & 0 & \cdots & \sigma_{2N\times 2M}^{-1} \end{pmatrix} \tag{2.60}$$

and only contains non-negative numbers. The relationship $\mathbf{\Theta} = \mathbf{U\Sigma V^{H}}$ is the singular value decomposition of matrix $\mathbf{\Theta}$, where $\mathbf{V}$ and $\mathbf{U}$ are the singular value vector matrices, and $\mathbf{\Sigma}$ is a rectangular diagonal matrix that contains the singular values. It is important to mention that integers M and N do not necessarily need to be equal, as they depend on the discretization that has been used to obtain the dimension-reduced spatial basis. At this point a new requirement to obtain the completed CSM can be stated as

$$\|\mathbf{\Psi}\mathbf{C}_{completed}(\omega)\mathbf{\Psi^{H}} - \mathbf{C}_{completed}(\omega)\|_F \leq \epsilon_2 \tag{2.61}$$

The above condition ensures that the entries of the completed CSM are not significantly changed due to the filtering process and ϵ_2 is the thresholding error that governs it. After all of the necessary variables have been introduced, the problem of CSM completion within the context of continuous-scan phased arrays is defined as

$$\begin{aligned} \text{minimize} \quad & \|\mathbf{C}_{completed}(\omega)\|_* \\ \text{subject to} \quad & \|\mathcal{A}(\mathbf{C}_{completed}(\omega)) - \mathbf{C}_{missing}(\omega)\|_F \leq \epsilon_1 \\ & \|\mathbf{\Psi}\mathbf{C}_{completed}(\omega)\mathbf{\Psi^{H}} - \mathbf{C}_{completed}(\omega)\|_F \leq \epsilon_2 \\ & \mathbf{C}_{completed}(\omega) = \mathbf{C}^{H}_{completed}(\omega) \succeq 0 \end{aligned} \tag{2.62}$$

The above equation is similar to that used by Yu *et al.* [67] within the context of non-synchronous microphone measurements, with it being successfully applied to complete block-Hermitian CSMs. However, an important distinction between the continuous-scan approach and the non-synchronous approach is that the data-missing CSM is not necessarily block-Hermitian. Another difference is that one does not need to physically move the array sequentially when using the continuous-scan approach, and the sequential array movement can be related to the signal processing and block segmentation schedule utilized. The completed CSM is finally computed, as per Eq. 2.62, using the Fast Iterative Shrinkage Thresholding Algorithm (FISTA) approach of Ref. [77] or using the complex optimization tools of the SDP Matlab library [56, 57]. It was found the results were largely independent of the method used. Using the methodology described above requires careful processing and organization of the completed and data-missing CSMs as outlined in Fig. 2.10. A schematic of a completed CSM is shown in Fig. 2.13, where 3 microphones are fixed, and the signal from one scanning sensor is divided into 6 blocks. The contributions from the fixed microphones are highlighted in blue, while those of the scanning sensor are highlighted in pink. The estimated cross-spectral densities from Eq. 2.62 are shown in yellow.

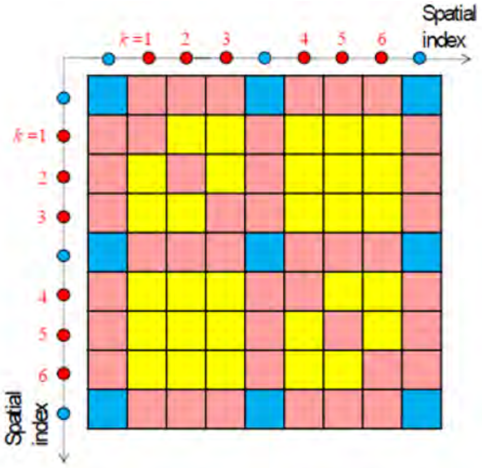

Figure 2.13: Schematic of a completed CSM within the continuous-scan paradigm; 3 microphones are fixed and the signal from one scanning sensor is divided into 6 blocks.

The completed CSM is finally steered back to a location ξ within the region of interest to find the array power response as

$$Y(\xi,\omega) = \frac{\mathbf{g}(\xi,\omega)\mathbf{C}_{completed}(\omega)\mathbf{g}^H(\xi,\omega)}{J} \tag{2.63}$$

where $J = \big(\mathcal{M}_s + K\mathcal{M}_s\big)^2$. Note that a fundamental difference between the steering vectors $\mathbf{g}(\xi, \omega)$ used in this approach and the CSSM technique is that the elements are here sorted according to their spatial index (for instance, from low to high polar angle). It must be noted that diagonal removal or reconstruction approaches can be used to improve the array response. This, however, requires a modification on the number of elements used J.

The steering vector matrix that is used in Eq. 2.63 has components that are associated with fixed microphones and continuously-scanning sensors. As such, the steering vectors associated with the continuously-scanning sensor should be corrected with the Doppler-shifted frequency introduced in the preceding section (Eq. 2.38).

A cautionary note is made with regards to the errors linked to the estimation of the missing entries of the CSM. These errors are denoted by Matrix Completion Errors (MCE), and can be defined as

$$\mathrm{MCE}(\omega) = \frac{\|\mathbf{C}_{\mathrm{real}}(\omega) - \mathbf{C}_{completed}(\omega)\|_F}{\|\mathbf{C}_{\mathrm{real}}(\omega)\|_F} \tag{2.64}$$

where $\mathbf{C}_{\mathrm{real}}$ is the real global CSM, in which all the relationships between sensors are known. Past studies [77] have investigated the performance of the matrix completion process in conjunction with the FISTA algorithm in the accrued estimation errors. It has been found that the MCE is usually below 0.1 when the signal-to-noise ratio of a given experiment is below 10 dB. The MCE improves when utilizing additional reference sensors that are common for all the non-synchronous measurement points, independently of the number of references used [77]. Reference [67] identified the FISTA approach as a robust method of minimizing Eq. 2.62 when the number of uncorrelated acoustic sources is unknown a priori. The matrix completion problem adapted to the continuous-scan approach can be considered an extension of the FISTA matrix reconstruction of Ref. [77], where the reference sensors are the fixed microphones and the sequential measurements are the distinct blocks.

Other matrix completion techniques could be utilizied, such as that of Ning *et al.* [73] which are based on Sylvester's law of inertia. However, these require the data-missing matrix to be block-Hermitian, which is not generally the case in continuous-scan beamforming.

2.5.5 Partial Fields Decomposition

In line with the previous section, the next paragraphs aim at constructing a CSM that is representative of the complete experiment run so that advanced beamforming and deconvolution approaches might be used in conjunction with the continuous-scan paradigm. The CSM is here constructed using a Partial Fields Decomposition (PFD) technique. This method varies from the preceding in that no elements of the CSM are calculated using a minimization algorithm. A phase referencing approach is used instead. The strategy presented here is similar to that used by Shah *et al.* [25, 26] and has been applied in past experimental studies to obtain the noise source images of supersonic jets and ducted fans. The approach presented in this section might be considered an extension of the start-and-stop method of Refs. [78, 79, 21] that is used in NAH and is briefly summarized next.

The method originally depended on having an array of *reference* (stationary) sensors measuring concurrently and continuously while a small subset of the array successively scanned through a number of patches. In this work, however, one microphone is continuously-scanning and the subset of the array at different patches is obtained through the signal segmentation. Additionally, the non-stationarity of the signal introduced by the scanning microphone requires advanced spectral estimation techniques such as the application of the frequency-dependent window in the computation of cross-spectral densities of sensors that have a relative velocity, as argued previously.

In general, the technique decomposes the acoustic field into an $\mathcal{M}_f$ number of coherent and mutually orthogonal partial fields on a hologram surface using reference sensors (fixed microphones) to provide the phase-reference. In the present thesis, the hologram surface corresponds to the scanned region, and the value for the partial field is obtained at each block center. The partial fields are then used to construct a CSM that is representative of the complete experiment run. A schematic of the decomposition of the acoustic field emitted by a jet noise source into partial fields on the hologram surface is shown in Fig. 2.14.

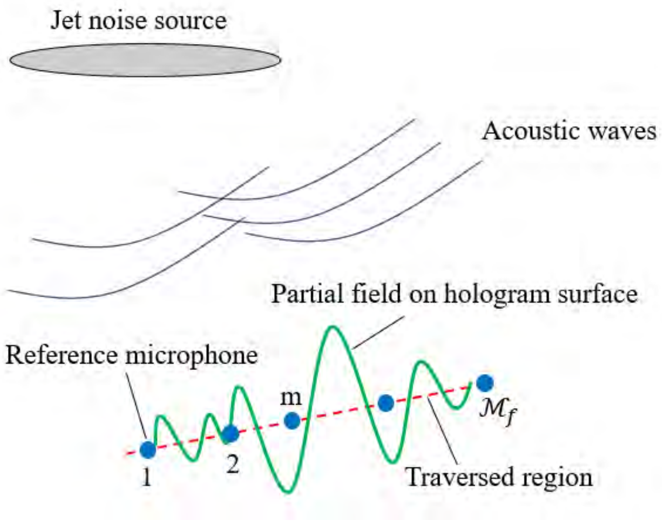

Figure 2.14: Schematic of the decomposition of the acoustic field emitted by a jet noise source into a partial field on the hologram surface.

The PFD might be employed in other contexts besides the construction of a CSM. For instance, the technique can be used for the development of low-order models that can be used in conjunction with boundary element methods [80]. In order to construct the partial fields, first the microphone signals must be divided into smaller, quasi-stationary blocks. A reference CSM (i.e., associated with the fixed sensors only) that uses the full duration of the microphone signals is computed. Then, a transfer function matrix between fixed and scanning sensors is calculated for each block. The partial fields are obtained for each block using the reference CSM and the transfer function matrix, and the full CSM is obtained by “sewing” together all the partial fields. The procedure is mathematically described in the next lines. A sketch of the process is depicted in Fig. 2.15, where 3 microphones are fixed (references), and one microphone is scanning. Only three blocks (k = 1, 3, 5) are shown.

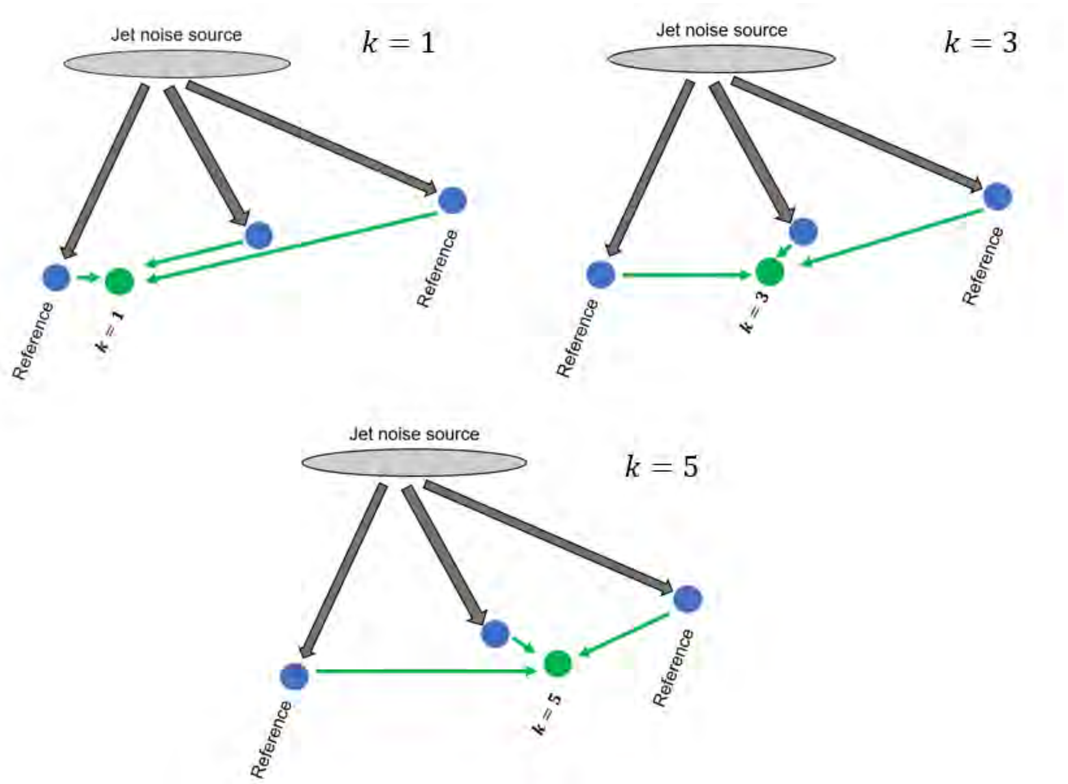

Figure 2.15: Schematic representation involved in the partial field decomposition technique for an array containing 3 fixed sensors and one scanning sensor. Blocks displayed are $k = 1$, 3, and 5.

The mathematical expressions involved in obtaining the CSM with the PFD technique for the continuous-scan approach are described next. First, a reference CSM, denoted by $\mathbf{C}_{ff,T}$, is constructed as

$$\mathbf{C}_{ff,T}(\omega) = C_{f_m f_n,T}(\omega) \;=\; \overline{P_{f_m,T}(\omega) P^{*}_{f_n,T}(\omega)} \tag{2.65}$$

where the matrix is constructed using the fixed sensors only, indicated by subscript ff, and using the complete duration of the pressure signals, indicated by subscript T. The reference CSM is a square and Hermitian matrix, with a singular value decomposition defined by

$$\mathbf{C}_{ff,T} = \mathbf{U}_{ff,T} \mathbf{\Sigma}_{ff,T} \mathbf{V}^{H}_{ff,T} \tag{2.66}$$

In line with the previous two continuous-scan approaches, the pressure signals from all sensors (fixed and scanning) are then divided into a number K of overlapping or non-overlapping blocks. The next step in the PFD technique is obtaining a transfer function matrix between the reference microphones and the continuously scanning sensors (i.e., the distinct blocks). The transfer function matrix is constructed for every block k as

$$\mathbf{H}_{fs,k} = \Big(\mathbf{C}_{ff,k}\Big)^{-1}\mathbf{C}_{fs,k} \tag{2.67}$$

where $\mathbf{H}_{fs,k}$ is the transfer function matrix, $\mathbf{C}_{ff,k}$ is a CSM computed using the fixed sensors only for block k

$$\mathbf{C}_{ff,k}(\omega) = G_{f_m f_n,k}(\omega) \ = \ \overline{P_{f_m,k}(\omega)P^*_{f_n,k}(\omega)} \tag{2.68}$$

and $\mathbf{C}_{fs,k}$ is the CSM computed using the combinations of fixed and scanning sensors

$$\mathbf{C}_{fs,k}(\omega) = C_{f_m s_n,k}(\omega) \ = \ \overline{P_{f_m,k}(\omega)P^*_{s_n,k}(\omega)} \tag{2.69}$$

The matrix $\mathbf{C}_{ff,k}$ might not necessarily have an inverse. Thus, it is a standard practice to find its pseudo-inverse using the Moore-Penrose formula

$$\Big(\mathbf{C}_{ff,k}\Big)^{-1} = \Big(\mathbf{C}_{ff,k}\Big)^{\dagger} = \mathbf{V}_{ff,k}\mathbf{\Sigma}^{-1}_{ff,k}\mathbf{U}^{H}_{ff,k} \tag{2.70}$$

where $\mathbf{C}_{ff,k} = \mathbf{U}_{ff,k}\mathbf{\Sigma}_{ff,k}\mathbf{V}^{H}_{ff,k}$ is the singular value decomposition of the matrix. The operation $\mathbf{\Sigma}^{-1}_{ff,k}$ is defined as

$$\mathbf{\Sigma}^{-1}_{ff,k} = \begin{pmatrix} \sigma^{-1}_{11} & 0 & \cdots & 0 \\ 0 & \sigma^{-1}_{22} & \cdots & 0 \\ \vdots & \vdots & \ddots & \vdots \\ 0 & 0 & \cdots & \sigma^{-1}_{\mathcal{M}_f\mathcal{M}_f} \end{pmatrix}_k \tag{2.71}$$

The partial fields for block k are calculated as

$$\mathbf{\Pi}_k = \mathbf{H}^T_{fs,k}\mathbf{U}_{ff,T}\mathbf{\Sigma}^{1/2}_{ff,T} \tag{2.72}$$

where T is used to indicate the transpose. The global CSM is the constructed by “sewing” the partial fields together as indicated in Ref. [25]

$$\mathbf{C}_{\text{PF}} = \mathbf{\Pi}^T_i\mathbf{\Pi}_j \quad i, j = 1, ..., K \tag{2.73}$$

In the notation adopted here, $\mathbf{C}_{\text{PF}}$ is used to denote the CSM obtained with PFD, having a size of $K\mathcal{M}_s \times K\mathcal{M}_s$. Once the CSM is obtained, the noise source map can be computed using the traditional DAS approach as

$$Y(\xi, \omega) = \frac{\mathbf{g}_{PF}(\xi, \omega)\mathbf{C}_{PF}(\omega)\ \mathbf{g}^H_{PF}(\xi, \omega)}{J} \tag{2.74}$$

where the steering vector matrix is

$$\begin{aligned} \mathbf{g}_{PF}(\xi, \omega) = \Big[& W_{11}e^{-i\omega'_{11}(\xi)\tau_{11}(\xi)} \quad ... \quad W_{\mathcal{M}_s1}e^{-i\omega'_{\mathcal{M}_s1}(x)\tau_{\mathcal{M}_s1}(\xi)} \\ & W_{12}e^{-i\omega'_{12}(\xi)\tau_{12}(\xi)} \quad ... \quad W_{\mathcal{M}_s2}e^{-i\omega'_{\mathcal{M}_s2}(\xi)\tau_{\mathcal{M}_s2}(\xi)} \\ & \quad ... \\ & W_{1K}e^{-i\omega'_{1K}(x)\tau_{1K}(x)} \quad ... \quad W_{\mathcal{M}_sK}e^{-i\omega'_{\mathcal{M}_sK}(\xi)\tau_{\mathcal{M}_sK}(\xi)} \Big] \end{aligned} \tag{2.75}$$

and has a size of $1 \times K\mathcal{M}_s$, and $J = (K\mathcal{M}_s)^2$

As stated in previous sections, diagonal removal or reconstruction processes can be used in conjunction with the partial fields beamforming approach. If the first approach is to be used, the number of elements J will require a modification. Additionally, the steering vector matrix that is used in Eq. 2.74 has contributions from continuously-scanning sensors (i.e., the distinct blocks at which the partial fields are calculated) and the Doppler-shifted frequency must be included.

Care must be taken when interpreting the results obtained with PFD. The partial fields are constructed by using phase information from the *reference* sensors (i.e., the fixed microphones). The PFD technique decomposes the acoustic field into a number of mutually orthogonal and coherent partial fields. The partial fields are then “sewed” together to construct a CSM based on the locations of the scanning sensor. The quality of the CSM depends on whether the number of partial fields utilized for its construction is sufficient to adequately represent the acoustic field emitted by the source. This number depends on the number of fixed microphones used to construct the reference CSM. It is generally accepted that, in other to fully describe a particular acoustic field, the number of microphones used must be greater that the number of noise sources present. This is particularly important for the case of jet noise, where the ranked singular values are expected to be well separated at low frequency, where turbulence mixing noise dominates, and be of a similar magnitude at high frequency, where small-scale turbulence noise is important. This is a manifestation of the randomness of noise generation at high frequency and makes the PFD less accurate at high frequency.

2.6 Summary of the Continuous-Scan Techniques

The preceding sections introduced three distinct methods to perform the noise source localization process utilizing measurements from arrays comprising fixed and continuously-scanning sensors. The first, CSSM, consisted in the natural extension of Fixed-Sensor (FS) DAS to the continuous-scan approach. The drawback of the method was its inability to obtain a global CSM, thus making it impossible to use deconvolution processes. Two techniques were introduced with the aim at constructing a global CSM. These techniques are based on a matrix completion process (CSMC) and a Partial Fields Decomposition (PFD) technique. The main characteristics of these methods are summarized in Table 2.2.

Name	Acronym	Based on	Global CSM	Deconvolution
Fixed-Sensor	FS	Traditional beamforming techniques	Yes	Yes
Cross-Spectral Submatrices	CSSM	Non-repeating contributions from block-CSMs	No	No
Cross-Spectral Matrix Completion	CSMC	Completing the missing entries of a sparse CSM using the FISTA scheme [67]	Yes	Yes
Partial Fields Decomposition	PFD	Using the fixed microphones as phase references to construct a transfer function matrix for each block to find the partial fields	Yes	Yes

Table 2.2: Summary of the beamforming methods utilized.

Deconvolution approaches might be applied to any of the techniques that obtains a global CSM, as indicated in the table, and are briefly summarized next.

2.7 Deconvolution Methods

In beamforming, the array response is a convolution between the noise source distribution and the array PSF, as given by Eq. 2.14. Several deconvolution approaches, which attempt at separating the noise source distribution and the PSF, have been proposed during the past decades. The present work utilizes three of such methods: DAMAS, CLEAN-SC and the Richardson-Lucy approach. These deconvolution techniques are briefly summarized next and their underlying assumptions are explained in detail.

2.7.1 DAMAS

The Deconvolution Approach for the Mapping of Acoustic Sources (DAMAS) was proposed by Brooks and Humphreys [63] in 2004. DAMAS discretizes Eq. 2.14 and assumes that the region of interest can be divided into a number N_x of uncorrelated monopole sources. The basic steps involved in the deconvolution process are briefly summarized next. This section uses a notation similar to that of Brooks and Humphreys for clarity.

The first step in the DAMAS process is to relate the Fourier transform of the pressure signal of microphone m to a modeled monopole source at a location ξ, contained within the region of interest

$$P_{m,\xi} = Q_{m,\xi} g_{m,\xi}^{-1} \tag{2.76}$$

where $Q_{m,\xi}$ is the Fourier transform of the pressure if it was not affected by shear-layer convection or any other losses, and $g_{m,\xi}^{-1}$ is the individual component of the steering vector of Eq. 2.10. Using the above equation, one might calculate the product of the pressure transforms to obtain a modeled CSM due to a source at location ξ

$$P_{m,\xi} P^*_{n,\xi} = (Q_{m,\xi} g^{-1}_{m,\xi})(Q_{n,\xi} g^{-1}_{n,\xi})^* \tag{2.77}$$

The above expression can be rearranged as

$$\mathbf{C}_{mod,\xi} = X_\xi \begin{pmatrix} (g_1^{-1})(g_1^{-1})^* & (g_1^{-1})(g_2^{-1})^* & \cdots & (g_1^{-1})(g_{\mathcal{M}}^{-1})^* \\ (g_2^{-1})(g_1^{-1})^* & (g_2^{-1})(g_2^{-1})^* & \cdots & (g_2^{-1})(g_{\mathcal{M}}^{-1})^* \\ \vdots & \vdots & \ddots & \vdots \\ (g_{\mathcal{M}}^{-1})(g_1^{-1})^* & (g_{\mathcal{M}}^{-1})(g_1^{-1})^* & \cdots & (g_{\mathcal{M}}^{-1})(g_{\mathcal{M}}^{-1})^* \end{pmatrix}_\xi = X_\xi \mathbf{C}_\xi \tag{2.78}$$

where X_ξ is the mean square pressure per bandwidth of the source (i.e., $X_\xi = Q_{m,\xi} Q^*_{n,\xi}$) and $\mathcal{M}$ is the total number of microphones used. Having divided the region of interest into a number $\mathcal{N}_x$ of increments, the modeled CSM then becomes

$$\mathbf{C}_{mod} = \sum_{i=1}^{\mathcal{N}_x} \mathbf{C}_{mod,i} \tag{2.79}$$

which states that the CSM has contributions from all the orthogonal sources located within the region of interest. The above expression can obviously be steered back to the region of interest to find the array response as

$$Y_{mod}(\xi, \omega) = \frac{\mathbf{g}(\xi, \omega) \mathbf{C}_{mod}(\omega) \mathbf{g}^{\mathbf{H}}(\xi, \omega)}{\mathcal{M}^2} \tag{2.80}$$

where $\mathbf{g}(\xi, \omega)$ are the steering vectors. By equating $Y_{mod}(\xi, \omega)$ to the experimentally-measured array response $Y(\xi, \omega)$, one can obtain an equation that relates the measured array response to that which is free of contamination from the sidelobes and is not influenced by shear-layer convection

$$Y(\xi, \omega) = \sum_{i=1}^{\mathcal{N}_x} X_i A_i(\xi) \tag{2.81}$$

where i is a running index that considers all uncorrelated sources and

$$A_i(\xi) = \mathbf{g}(\xi, \omega)\mathbf{C}_i\mathbf{g}^{\mathbf{H}}(\xi, \omega) \tag{2.82}$$

In the application of the DAMAS algorithm to the continuous-scan approach, the terms included in the steering vectors $\mathbf{g}(\xi, \omega)$ should reflect the Doppler-shifted frequency when dealing with moving sensors. Equations 2.81 and 2.82 constitute the fundamental relations for the DAMAS algorithm. As stated by Brooks and Humpreys, if matrix $A_i(\xi)$ was non-singular, one could find the source auto-powers as $X = A^{-1}Y$. However, in many instances, A is a singular matrix, making the inversion cumbersome. The authors proposed to use an iterative scheme to solve Eq. 2.81. A component of Eq. 2.81, where the ω is omitted for brevity can be expressed as

$$Y(\xi) = A_1(\xi)X_1 + A_2(\xi)X_2 + ... + A_{\mathcal{M}}(\xi)X_{\mathcal{M}}. \tag{2.83}$$

When the matrix $A_i(\xi)$ is steered to location ξ, we obtain $A_i(\xi) = 1$ (see Eq. 2.82). As such, Eq. 2.83 can be rearranged as

$$X_{i=\xi} = Y(\xi) - \Big(\sum_{i=1}^{i=\xi-1} A_i(\xi)X_i + \sum_{i=\xi+1}^{N_x} A_i(\xi)X_i \Big) \tag{2.84}$$

The notation $i = \xi$ represents the index of i that is associated with location ξ within the region of interest. The above equation is solved iteratively using a Gauss-Seidel approach when using DAMAS. For the first iteration, it is assumed that the initial values X_i can be taken as zero. The source auto-powers are updated as each equation is resolved, and used in a succeeding fashion. The algorithm stops when the solution has converged.

2.7.2 CLEAN-SC

The CLEAN-SC deconvolution process was introduced by Sijtsma [14] in 2007 as an improvement of the Clean-PSF method, which is widely used in astronomy. The CLEAN-SC assumes the source to be comprised of single correlated sources, with no correlation between them, and uses the fact that the sidelobes are coherent with the main lobe to remove their contributions from the noise source map iteratively. This section briefly summarizes the steps involved in the deconvolution process, as described in the influential work of Sijtsma [14].

First, the source cross-powers are defined as

$$\mathbf{Y}(x,\xi,\omega) = \mathbf{g}(x,\omega)\mathbf{C}(\omega)\mathbf{g}^{\mathbf{H}}(\xi,\omega) \tag{2.85}$$

A new quantity, known as degraded CSM is defined. For the first iteration, this quantity is just

$$\mathbf{D}^{(i=0)}(\omega) = \mathbf{C}(\omega) \tag{2.86}$$

The source power at location ξ can be calculated using the traditional beamforming algorithm. That is, for the first iteration $i = 0$

$$\mathbf{Y}(\xi,\omega) = \mathbf{g}(\xi,\omega)\mathbf{C}(\omega)\mathbf{g}^{\mathbf{H}}(\xi,\omega) = \mathbf{g}(\xi,\omega)\mathbf{D}^{(i=0)}(\omega)\mathbf{g}^{\mathbf{H}}(\xi,\omega) \tag{2.87}$$

Using the above expression, the location of the peak source (i.e., the strongest source) can be determined. This peak source induces a CSM that can be assumed to be

$$\mathbf{G}^{(i)} = Y_{max}^{(i-1)}(\omega)\mathbf{g}_{\mathbf{max}}^{(\mathbf{i})}(\omega)\mathbf{g}_{\mathbf{max}}^{\mathbf{H},(\mathbf{i})}(\omega) \tag{2.88}$$

The steering vector matrix $\mathbf{g_{max}}$ is that which is associated with the position of the peak source. The relationship is the fundamental idea behind the Clean-PSF method. However, the matrix $\mathbf{G}$ is constructed differently in the CLEAN-SC approach to account for the coherence between the sidelobes and the main lobe. The matrix is built such that cross-powers of any scan point satisfy

$$\mathbf{g}(x,\omega)\mathbf{D^{(i-1)}}\mathbf{g_{max}^{H,(i)}}(\omega) = \mathbf{g}(x,\omega)\mathbf{G^{(i)}}\mathbf{g_{max}^{H,(i)}}(\omega) \tag{2.89}$$

for all possible $\mathbf{g}(x,\omega)$. The above equation does not have a unique solution and is only satisfied when [14]

$$\mathbf{D^{(i-1)}}(\omega)\mathbf{g_{max}^{H,(i)}} = \mathbf{G^{(i)}}(\omega)\mathbf{g_{max}^{H,(i)}} \tag{2.90}$$

Assuming that $\mathbf{G^{(i)}}(\omega)$ is due to a single source component $\mathbf{h^{(i)}}(\omega)$, the matrix can be constructed as

$$\mathbf{G^{(i)}}(\omega) = Y_{max}^{(i-1)}\mathbf{h^{(i)}}(\omega)\mathbf{h^{H,(i)}}(\omega) \tag{2.91}$$

The above equation is rewritten as

$$\mathbf{G^{(i)}}(\omega) = Y_{max}^{(i-1)}\mathbf{h^{(i)}}(\omega)\mathbf{h^{G,(i)}}(\omega) = Y_{max}^{(i-1)}\Big(\mathbf{h^{(i)}}(\omega)\mathbf{h^{H,(i)}}(\omega) - \mathbf{H^{(i)}}(\omega)\Big) \tag{2.92}$$

where the term $\mathbf{H^{(i)}}(\omega)$ is

$$\mathbf{H_{x,\xi}^{(i)}} = \mathbf{h^{(i)}}(x,\omega)\mathbf{h^{H,(i)}}(\xi,\omega) \tag{2.93}$$

for all positions $x \neq \xi$. Equation 2.90 is only solved when

$$\mathbf{h^{(i)}}(\omega) = \frac{1}{\left(1 + \mathbf{g^{(i)}_{max}}(\omega)\mathbf{H^{(i)}}(\omega)\mathbf{g^{H,(i)}_{max}}(\omega)\right)^{1/2}} \times \left(\frac{\mathbf{D^{(i-1)}}(\omega)\mathbf{g^{H,(i)}_{max}}(\omega)}{Y^{(i-1)}_{max} + \mathbf{H^{(i)}}(\omega)\mathbf{g^{H,(i)}_{max}}(\omega)}\right) \tag{2.94}$$

As stated by Sijtsma [14], $\mathbf{H^{(i)}}(\omega)$ contains the diagonal elements of $\mathbf{h^{(i)}}(\omega)\mathbf{h^{H,(i)}}(\omega)$. As such, an iterative scheme must be employed to achieve convergence. It is usually assumed that $\mathbf{h^{(i)}}(\omega) = \mathbf{g^{(i)}_{max}}(\omega)$. The source powers (the deconvolved noise source map) is then obtained as

$$Q^{(i)}(\xi) = \phi Y^{(i-1)}_{max}(\omega)\Psi(\xi - \xi_{max}) \tag{2.95}$$

where $\Psi(\xi - \xi_{max})$ is just a beam of a specified width, that fulfills $\Psi(0) = 1$ and ϕ is a gain between 0 and 1. The degraded CSM is then computed as

$$\mathbf{D^{(i)}}(\omega) = \mathbf{D^{(i-1)}}(\omega) - \phi Y_{max}(\omega)\mathbf{h^{(i)}}(\omega)\mathbf{h^{H,(i)}}(\omega) \tag{2.96}$$

The deconvolution process stops when the CSM is sufficiently degraded

$$||\mathbf{D^{(i-1)}}(\omega)|| \leq ||\mathbf{C}(\omega)|| \tag{2.97}$$

The principal drawback of the CLEAN-SC technique is that it tends to merge closely-spaced sources into a single one that has the sum of strengths [81, 82, 28]. This is due to the relatively high level of coherence of the sidelobes surrounding the main lobe with the main lobe itself. As such, this approach might not be ideal when trying to resolve flow fields that contain very fine features. Successful attempts at improving the spatial resolution of CLEAN-SC have been carried out [81]. However, this work did not explore such methods.

2.7.3 Richardson-Lucy

The Richardson-Lucy image restoration algorithm is described in the next paragraphs. This technique originated within the field of astronomy, when trying to de-blur astronomical images by Richardson[15] in 1972 and Lucy[16] in 1974. The method has been extensively used in acoustic beamforming in past studies [83, 17, 1, 64]. The Richardson-Lucy deconvolution technique is based on assigning the meaning of a conditional probability to the PSF. The inversion method makes use of Bayes' theorem to find the inverse conditional probability $R(\xi|x,\omega)$. In line with the DAMAS approach, the R-L algorithm assumes the sources to be statistically incoherent and approximates the convolution integral of Eq. 2.14 as a sum of $\mathcal{N}_x$ elements (i.e., $\mathcal{N}_x$ sources). This section outlines a method to perform the R-L deconvolution that is similar to that of Ref. [17].

For a given frequency, and assuming a total of $\mathcal{N}_x$ incoherent sources, Eq. 2.14 is discretized as

$$Y(\xi,\omega) \to Y_i$$

$$R(x,\xi,\omega) \to R_{ni}$$

$$\Phi(x,\omega)\Delta \to \Phi_n$$

such that the following linear system is obtained

$$Y_i = \sum_{n=1}^{\mathcal{N}_x} R_{in}\Phi_n \tag{2.98}$$

The Richardson-Lucy iteration algorithm is [15, 16]

$$\Phi_n^{(r)} = \Phi_n^{(r-1)} \frac{1}{\sum_{i=1}^{N} R_{in}} \sum_{i=1}^{\mathcal{N}_x} \frac{R_{in}Y_i}{\tilde{Y}_i} \tag{2.99}$$

where r denotes the iteration step and

$$\tilde{Y}_i = \sum_{n=1}^{\mathcal{N}_x} R_{in} \Phi_n^{(r-1)} \tag{2.100}$$

The Richardson-Lucy image restoration technique is independent of the indices i and n and does not need to be performed in a specific order, such as DAMAS, thus becoming a more robust means of inverting the previous relationship. In addition, the Richardson-Lucy image restoration technique produces produces results that are of higher quality as those obtained by DAMAS.

Chapter 3

Signal Processing for Continuous-Scan Microphone Arrays

The biggest challenge of the continuous-scan approach is the treatment of the non-stationarity in the pressure signals introduced by the scanning sensors. This has been extensively discussed and treated in the preceding section. To summarize, quasi-stationarity is sought by dividing the signal into blocks (i.e. the signal is quasi-stationary within each block) and by applying a frequency-dependent window that acts as a block size filter. The frequency-dependent window can take any of the forms outlined in Table 2.1.

The newly-introduced signal segmentation process has direct consequences on the quality of the noise source maps. As a result, this section studies it carefully and proposes clear guidelines to improve the spatial resolution of the noise source maps and minimize computational time for processing the data from continuous-scan phased microphone arrays. Criteria to determine the optimal number of the blocks and their size are formulated in terms of the geometry of the microphone array, the spectral estimation parameters, and the width of the frequency-dependent window. Only uniform signal division (equal block sizes) for each frequency range of interest is considered.

In general, processing of non-stationary signals may employ adaptive segmentation [84] creating non-uniform block sizes and overlaps. To that end, several techniques that divide the signal based on local changes in amplitude and/or frequency have been proposed [85, 86, 87, 88]. Some of these techniques require the tuning of different parameters such as the window length and overlap for a fractal dimension-based signal segmentation. Estimation of the parameters is key in order to reduce false block boundaries [89]. These methods greatly increase the computational cost and complexity of the signal processing, and do not always find the most suitable segmentation. In addition, a non-uniform block division for each element of the frequency vector would entail a prohibitive computational cost. For these reasons, only a uniform signal division is considered here (i.e., equal block sizes for each frequency range of interest), where the block sizes are based on the criteria outlined in the previous paragraph.

Furthermore, the previously described methods do not account for the beamforming nature of this study, in which the distance between fixed microphones and the scanning sensor has a strong influence on the spatial resolution of the noise source maps. Sufficient spatial sampling at high frequencies requires a very dense array, with microphone spacings of the order of the acoustic wavelength, which is deemed impractical in most of the cases when using fixed sensors only. The continuous-scan approach and the distinct block schedules intend to resolve this issue by introducing closely-spaced measurement points (i.e., the different blocks) between a given fixed microphone and the scanning sensor, significantly reducing the sidelobe levels.

This section will introduce new concepts on the signal segmentation process: upper bound for the block size, minimum and maximum block size, number of blocks and block overlap. Criteria for an optimal signal segmentation will be formulated in terms of these quantities.

Parts of this chapter are a partial reprint and adaptation of Morata, D., and Papamoschou, D., *"Advances in the Direct Spectral Estimation of Aeroacoustic Sources Using Continuous-Scan Phased Arrays"*, AIAA Paper 2021-0215, doi: 10.2514/6.2021-0215. Excerpts from the chapter have been submitted as a full-length journal paper to the Journal of Sound and Vibration (ElSevier) as *"Optimized Signal Processing for Microphone Arrays Containing Continuously-Scanning Sensors"*, with Morata, D., and Papamoschou, D., as the authors, as of March 9th, 2022

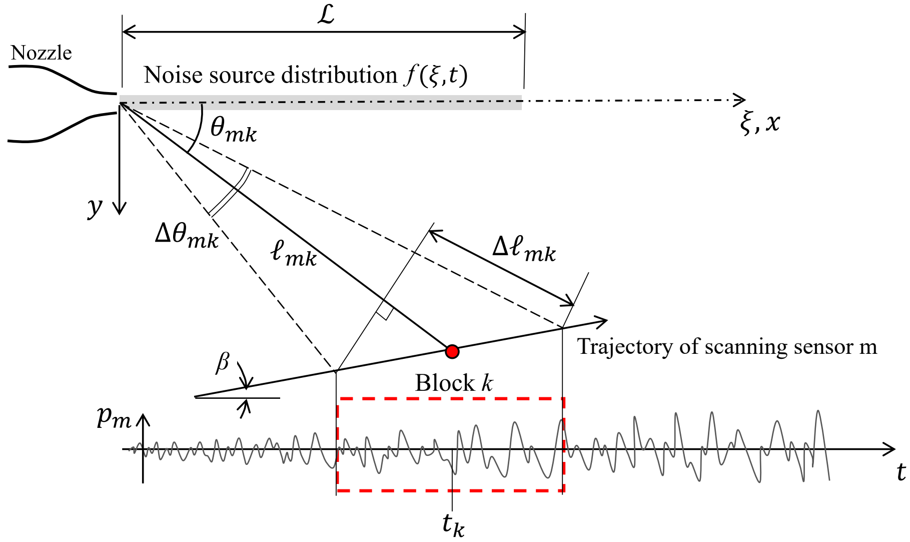

Figure 3.1: Distance and angle variations associated with the length of a signal block.

3.1 Upper Bound on Block Size

The upper bound on block size is based on the quasi-stationary approximations of Eq. 2.17. It is thus independent of frequency. Referring to Fig. 3.1, in the analysis that follows the origin of the source is placed at $(\xi, y) = (0, 0)$ for simplicity. This is valid when the sensors are in the geometric far field; otherwise, the steps presented below would need to be extended to various locations in the source region.

The first concern is the validity of the approximation $\ell_m(t,\xi) \approx \ell_{mk}(\xi)$ in Eq. 2.17. Considering a given block k for sensor m, this involves the variation of the source-sensor distance within the block and can be quantified as

$$\epsilon_{\ell,mk} = \frac{|\Delta \ell_{mk}|}{\ell_{mk}} \tag{3.1}$$

where ℓ_{mk} is the source-sensor distance at the center of the block and $\Delta \ell_{mk}$ is the variation of this distance across the block, as illustrated in Fig. 3.1. It is worked out from the geometry that $|\Delta \ell_{mk}| \approx V_{mk} T \cos\beta / \cos\theta_{mk}$, thus the error can be related to the velocity of the scanning sensor and to its position with respect to the noise source:

$$\epsilon_{\ell,mk} \approx \frac{V_{mk} T \cos\beta}{\ell_{mk} \cos\theta_{mk}} \tag{3.2}$$

Low scan velocities are preferred to maintain the errors in the approximation of Eq. 2.17 within reasonable limits, thus avoiding excessively small block sizes that might compromise the spectral estimation, as will be discussed in the next section.

The second concern is related to the directivity of the acoustic source. For a substantially omnidirectional acoustic field, this can be directly connected to Eq. 3.1. However, in a field with strong directivity, the directivity can overwhelm the geometric effects. Considering a source with characteristic polar directivity Θ, the error related to the source directivity is formulated as

$$\epsilon_{\theta,mk} = \frac{|\Delta \theta_{mk}|}{\Theta} \tag{3.3}$$

where $\Delta\theta_{mk}$ is the polar angle variation across the block, as indicated in Fig. 3.1. Figures 5.9, 5.17 and 5.35 show the far-field narrowband spectra for the impinging jet source, the isolated subsonic jet, and the isolated supersonic jet, at a number of polar angles θ. For the impinging-jets source, the spectrum varies as much as 3 dB for $\Delta\theta = 4°$ at the downstream-most polar stations. The spectrum of the subsonic jet also varies approximately 3 dB for $\Delta\theta = 4°$

near the peak emission region ($\theta \approx 35°$). It was observed how the spectra of the isolated supersonic jet varied as much as 6 dB for neighboring polar stations ($\Delta\theta = 6°$, with the tonal components being especially important. Therefore, it is physical to set $\Theta = 4° = 0.0698$ for all the acoustic sources. A different Θ could be set for the supersonic jet, however, the results on the upper bound on block size were largely independent of $\epsilon_{\theta,mk}$ for far-field microphone measurements, as will be detailed next.

To determine the upper bound on the block size, first the error thresholds are set. The selection here is $\epsilon_{\ell,mk} = 0.01$ and $\epsilon_{\theta,mk} = 0.3$. The sensor's trajectory is discretized into fine increments $(x_k, y_k), k = 1, \ldots, M$, representing the location of the center of a block. For each (x_k, y_k), the sample size N_k of the block determines its spatial extent through the sampling rate F_s and the sensor speed V_m, allowing calculation of the errors. N_k is increased from low value until one of the error thresholds is exceeded; this sets the final value of N_k. Seeking a uniform block size, the maximum bound is set equal to the minimum value of the vector N_k, that is,

$$N_{B_u} = \min(N_k, k = 1, \ldots, M) \tag{3.4}$$

For the experiments covered in this study, the criterion of Eq. 3.1 was always more constraining than the one related to Eq. 3.3. Once the upper bound is defined, the next steps involve determination of frequency-dependent minimum and maximum block sizes.

3.2 Minimum Block Size

The need to suppress the frequency of the spectral oscillation of Eq. 2.30 drives the processing towards small block sizes, particularly at high frequency. However, each block must contain sufficient samples to compute the auto- and cross-spectral densities accurately, the latter being strongly impacted by non-stationarity. This motivates the development of a criterion for the minimum block size, which is frequency-dependent.

Consider signals $p_m(t)$ and $p_n(t)$ corresponding to the pressure recorded by a scanning sensor and a fixed sensor, respectively. The signals are divided into K overlapping or non-overlapping blocks, each one of them containing N_B samples. For each block, the cross-spectral density is estimated by (i) dividing each signal into S segments with overlap σ_S; (ii) computing the Fast Fourier Transform (FFT) of the signals in each segment; (iii) multiplying appropriately the FFTs of the two signals within each segment, including the windowing process; and (iv) averaging the results over the number of segments. In the last step, the accuracy and smoothness of the result improve with increasing S. The FFT algorithm requires that each segment contains $2N_{\mathrm{FFT}}$ samples, where N_{FFT} is the size of the Fourier Transform. It is easy to show that the size of the block is related to the number of segments, segment overlap, and FFT size as follows:

$$N_B \;=\; 2N_{\mathrm{FFT}}\Big[(1-\sigma_S)(S-1)+1\Big] \tag{3.5}$$

For fixed segment overlap and FFT size, the minimum size of the block is dependent on the smallest number of segments that allows for accurate spectral estimation. This is directly linked to the nature of the acoustic source as well as to the array geometry.

The accuracy of spectral estimation is evaluated based on the narrowband SPL spectrum of the scanning sensor. The SPL is computed with fixed overlap, fixed N_{FFT}, and increasing number of segments S (thus increasing number of total samples) until the maximum sample bound (Eq. 3.4) is reached. Denoting SPL_S and SPL_{S-1} the SPL computed with number of segments S and $S-1$, respectively, the difference $\Delta\mathrm{SPL}_S = \mathrm{SPL}_S$ - SPL_{S-1} is plotted versus S for a number of frequencies. This quantity is a measure of the convergence of the statistics for each block as a function of the number of sample points utilized (i.e., the number of segments). Figure 3.2 plots this relationship for IJS and the subsonic turbulent jet, with $N_{\text{FFT}} = 1024$ and $\sigma_S = 0.5$. It is seen that ΔSPL_S undergoes strong oscillations when the number of segments is small. For $S \geq 15$ the spectral estimation has a variability of less than 0.25 dB for both sources. Thus, a minimum number of segments $S_{\text{min}} = 15$ is set as a criterion. Analysis for the supersonic jet, the distinct reflector configurations, and the remaining shielding and reflector configurations for the subsonic jet flow did not yield a different result, and $S_{\text{min}} = 15$ is used throughout this work. It is advisable to perform this analysis for various values of N_{FFT} and positions of the scanning sensor, although in the present experiments the result was largely independent of N_{FFT}. From Eq. 3.5 the minimum size of the block becomes

$$N_{B_{\text{min}}} = 2N_{\text{FFT}}\Big[(1-\sigma_S)(S_{\text{min}}-1)+1\Big] \tag{3.6}$$

3.3 Maximum block size

The maximum block size is driven by the implementation of the frequency-dependent windows of Table 2.1. These windows are integrated with the spectral estimation [1]. Multiplication of the signal within each block by the frequency-dependent window produces an effective reduction of the block size, as illustrated in Fig. 3.3. The reduction can be severe at high frequency, meaning that a significant portion of the block is neglected. The analysis carried out in this section uses the Gaussian window of Table 2.1. However, the reasoning can be similarly extended to the hyperbolic secant and Cauchy distribution. To limit the loss of information, one may consider maintaining the ratio T/δ constant. This would entail different block division for each frequency and therefore spectral estimation for each element of the frequency vector at prohibitive computational cost. It would also obviate the need for the Gaussian window, which allows efficient spectral estimation across the entire frequency

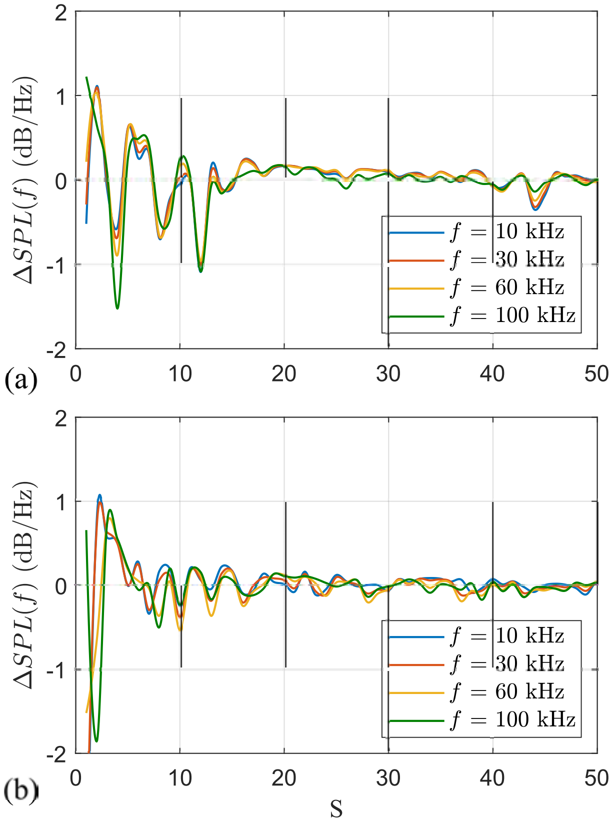

Figure 3.2: ΔSPL computed with consecutive segment increases as a function of the number of segments for $N_{\mathrm{FFT}} = 1024$ for distinct acoustic sources: (a) Impinging jets source; and (b) subsonic jet.

vector. However, it will be shown that setting $T \sim \delta$ connects directly T to the size of the FFT, which has a step-wise relation with frequency, as discussed in Ref. [1]. In other words, the above relation becomes discrete and requires spectral estimation for only a small number of frequency ranges, typically four.

The window width δ (Eq. 2.34) must be adequately covered by the segments used in the spectral estimation. This is illustrated in the sketch of Fig. 3.4, which depicts the division of the signal within a given block into segments and the generic shape of the Gaussian filter. For simplicity, the figure shows segments with zero overlap but the results that follow apply for positive overlap as well. Of the S segments covering the entire block, a sufficient number of them, c_{cov}, must be used to resolve the width δ of the Gaussian window. This number,

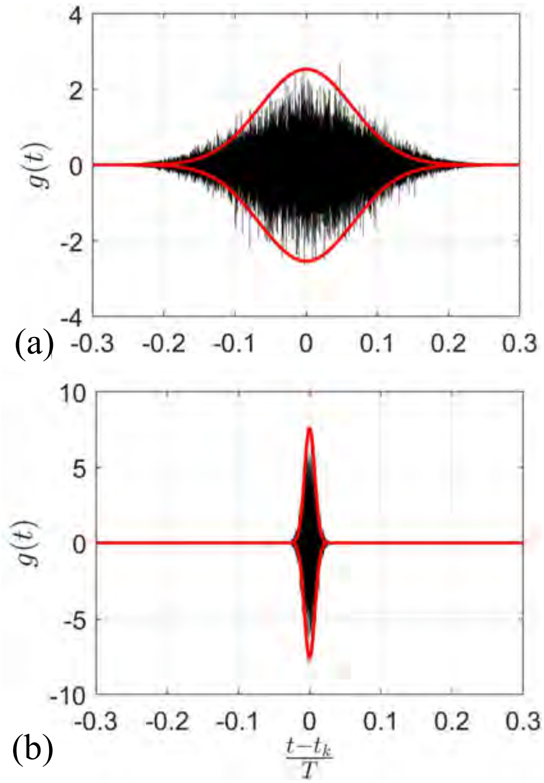

Figure 3.3: Example of the frequency-dependent Gaussian window (red) and resulting filtering of signal (black). (a) $f = 10$ kHz; (b) $f = 90$ kHz.

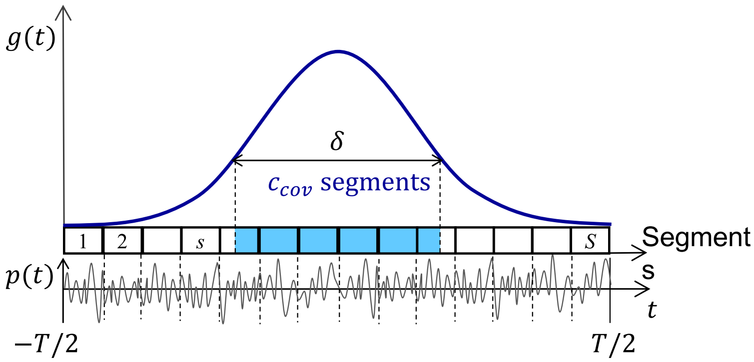

Figure 3.4: Segmentation of signal within a block and Gaussian window at given frequency.

which is not necessarily an integer, is selected to be $c_{\text{cov}} = 5$ [1]. Past experience has shown that $c_{\text{cov}} = 5$ adequately resolves the Gaussian and higher values do not offer a significant benefit [1, 26]. The window width can then be expressed as

$$\delta \;=\; c_{\text{cov}}\;\Delta t_{\text{seg}}$$

where $\Delta t_{\text{seg}} = 2N_{\text{FFT}}/F_s$ is the duration of each segment. Accordingly,

$$T \;=\; 2\frac{T}{\delta}\;c_{\text{cov}}\frac{N_{\text{FFT}}}{F_s}$$

Multiplication by the sampling rate F_s yields a frequency-dependent maximum block size

$$N_{B_{\max}} \;=\; 2\frac{T}{\delta}\;c_{\text{cov}}\;N_{\text{FFT}} \tag{3.7}$$

The coverage requirement imposes the restriction [1]

$$N_{\text{FFT}} \;\le\; \frac{1}{2}\frac{c_\lambda}{c_{\text{cov}}}\frac{a}{V_m}\frac{F_s}{f} \tag{3.8}$$

Because N_{FFT} must be a power of two, this entails discrete reduction of N_{FFT} with increasing frequency, and attendant discrete reduction of the block size. For example, setting $T/\delta = 1.7$ ensures that the tails of the Gaussian filter reach 50% of the peak value at the ends of the block. For adequate coverage of δ [1], a reasonable selection is $c_{\text{cov}} = 5$. Then, Eq. 3.7 becomes

$$N_{B_{\max}} \;=\; 17\;N_{\text{FFT}}$$

Matching the lower and upper bounds given by Eqs. 3.5 and 3.7, respectively, allows determination of the segment overlap

$$\sigma_S \;=\; 1 \;-\; \frac{\frac{T}{\delta}c_{\text{cov}} - 1}{S_{\min} - 1} \tag{3.9}$$

The role of the coverage requirement on the estimated acoustic source distribution was also explored in Ref. [26].

3.4 Number of blocks and overlap

Considering a signal with total number of samples N_T divided into blocks of size N_B and overlap σ_B, the number of blocks is

$$K = \frac{N_T - \sigma_B N_B}{(1 - \sigma_B) N_B} \tag{3.10}$$

The block overlap quantifies the repeated information contained in contiguous blocks. The number of non-repeating elements of the distinct CSSMs is

$$J = (\mathcal{M}_f - \mathcal{M}_s)^2 + (K - 1)\mathcal{M}_s(2\mathcal{M}_f - \mathcal{M}_s)$$

as outlined in the previous section. The number of non-repeating elements for CSMC is

$$J = (\mathcal{M}_f + K\mathcal{M}_s)^2$$

and that of the PFD technique is

$$J = (K\mathcal{M}_s)^2$$

The value of J relates to the cost of computing the CSMs as well as the cost of inverting the integral of Eq. 2.14. Some level of block overlap $\sigma_B > 0$ is desirable to prevent loss of information caused by the frequency-dependent filtering. However, excessive overlap leads to increase the computational cost without yielding new information. An appropriate balance appears to be $0.25 \leq \sigma_B \leq 0.75$ and is comparable to that used in recent work [26]. For the optimal signal division that will be proposed, the block overlap is set at $\sigma_B = 0.5$. However, this work will also show noise source maps obtained with a coarse block schedule, with $\sigma_B = 0.9$. This non-optimal schedule is used to illustrate the role of the signal processing on the resolution of the noise source maps.

3.5 Optimal signal segmentation

The guidance for signal division is summarized. The geometric criterion of Eq. 3.4 sets an upper bound on block size, N_{B_u}, for ensuring that the approximations of Eq. 2.17 are valid. The accuracy of spectral estimation imposes a frequency-dependent minimum size, $N_{B_{\text{min}}}$, formulated in Eq. 3.6. Prevention of information loss from the frequency-dependent window that filters each block requires frequency-dependent maximum size, $N_{B_{\text{max}}}$, defined by Eq. 3.7. Both $N_{B_{\text{min}}}$ and $N_{B_{\text{max}}}$ are directly proportional to the size of the FFT, N_{FFT}, used for spectral estimation, which has a step-wise declining relation with frequency.

The qualitative diagrams of Fig. 3.5 help explain these relationships. Figure 3.5a displays the trend of the block-size bounds versus N_{FFT}. N_{B_u} is invariant on N_{FFT} since it depends only on the array geometry, speed of the sensor, and directivity of the source. $N_{B_{\text{max}}}$ and $N_{B_{\text{min}}}$ are linear with N_{FFT}. The area bounded by $N_{B_{\text{max}}}$, $N_{B_{\text{min}}}$, and N_{B_u} (highlighted in green) represents the block sizes associated with optimal signal division. The relation of N_{FFT} with frequency is sketched in Fig. 3.5b. It declines in step-ladder fashion with frequency following Eq. 3.8 and the requirement that N_{FFT} be an integer power of two. Figure 3.5c represents the combination of the trends in the previous subfigures, showing that $N_{B_{\text{max}}}$ and $N_{B_{\text{min}}}$ decline in discrete steps with increasing frequency. The green region again represents the optimal block sizes. The sample size of the window width $F_s\ \delta$ is a smooth function of frequency. So, while the block size experiences discrete changes, the smoothness of δ ensures that filtering is done in a continuous fashion with minimal loss of information.

It is possible to match $N_{B_{\max}}$ and $N_{B_{\min}}$ by setting the segment overlap σ_S (used in spectral estimation) according to Eq. 3.9. This would result in the most efficient block division in terms of computational cost. Once the block sizes are set versus frequency, the number of blocks follows Eq. 3.10. If it turns out that $N_{B_{\max}} < N_{B_{\min}}$, and this cannot be fixed by reasonable settings of σ_S, it would imply that experimental parameters such as sensor speed and sampling frequency may need to be revised.

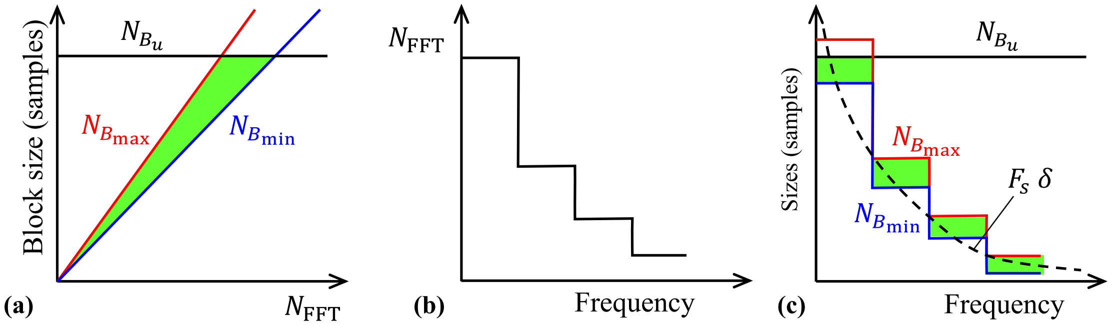

Figure 3.5: Trends governing the determination of optimal block size. (a) Block-size bounds versus N_{FFT}; (b) N_{FFT} relation with frequency; (c) Block-size bounds and Gaussian window width (in samples) versus frequency. Green regions indicate the allowed block size.

Chapter 4

Experimental Program

This section provides an overview of the experimental setup used to conduct the acoustic investigations presented in this work. It features a description of the anechoic chamber, microphone array and traversing system, microphone tracking system and a detailed description of the distinct acoustic sources used. The section also outlines the distinct block schedules that have been utilized.

Parts of this chapter are a partial reprint and adaptation of Morata, D., and Papamoschou, D., *"Advances in the Direct Spectral Estimation of Aeroacoustic Sources Using Continuous-Scan Phased Arrays"*, AIAA Paper 2021-0215, doi: 10.2514/6.2021-0215, and Morata, D., and Papamoschou, D., *"Extension of Traditional Beamforming Methods to the Continuous-Scan Paradigm"*, AIAA Paper 2022-1154, doi: 10.2514/6.2022-1154. Some figures have been obtained from Papamoschou, D., Morata, D., and Shah, P, *"Direct Spectral Estimation Method for Continuous Scan Beamforming"*, AIAA Paper 2018-2806, doi: 10.2514/6.2018-2806, with permission from the authors.

4.1 Anechoic Facility and Microphone Array

All the noise measurements were taken inside an anechoic facility of approximately 990 sqft in internal size, schematically depicted in Fig. 4.1. The inner side of the walls of the anechoic chamber were covered with acoustic foam wedges that were arranged to minimize wave reflections. The microphone array comprised twenty-four 1/8-inch condenser microphones (Brüel and Kjaer, Model 4138) with frequency resolution up to 120 kHz. The microphones were connected, in groups of four, to six conditioning amplifiers (Brüel and Kjaer, Model 2690-A-0S4). The outputs of the amplifiers were sampled simultaneously, at 250 kHz per channel, by three 8-channel multi-function data acquisition boards (National Instruments PCI-6143) installed in a PC with an Intel i7-7700K quad-core processor. National Instruments Labview software provided the interface for signal acquisition and filtering, as well as control of the experiment, utilizing a custom built program and graphics user interface.

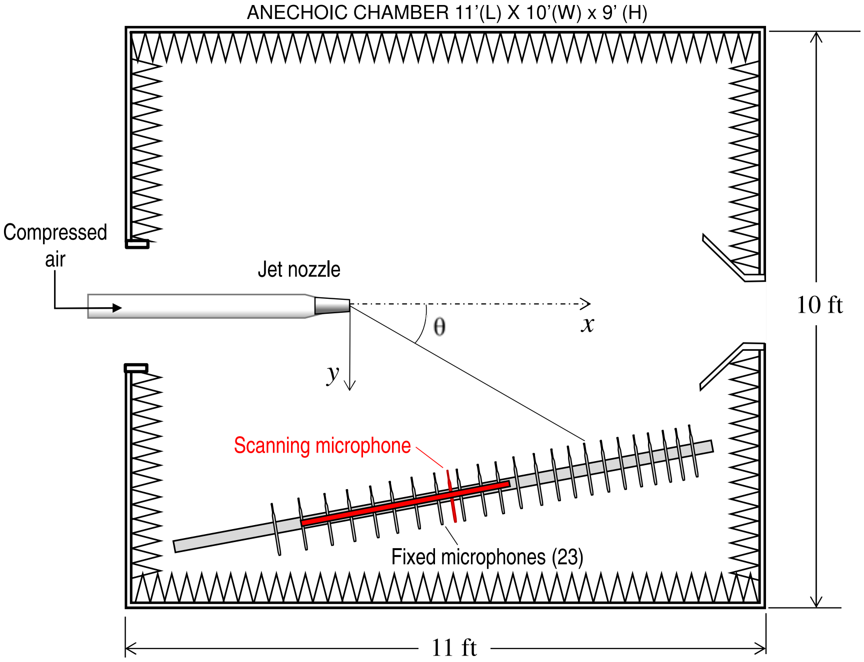

Figure 4.1: Anechoic chamber and qualitative deployment of the microphones.

The 'atmospheric' details inside the anechoic chamber were measured: temperature and humidity were recorded to enable computation of acoustic atmospheric absorption and calculation of the exact speed of sound. The microphone signals were conditioned with a high-pass filter set at 350Hz to wipe out any possible DC noise of the signals.

The narrowband sound pressure level (SPL) presented in this work have been computed using a 2048-point Fast Fourier Transform, yielding to a frequency resolution of 122Hz. The SPL spectra presented here are all corrected for microphone actuator response, microphone free field response and atmospheric absorption, thus resulting in lossless spectra. They are also referenced to a 1 foot arc radius (0.31 m).

One continuous-scan microphone was mounted on a linear traverse consisting of a belt drive (Igus ZLW-0630) powered by a servo motor (ClearPath-MCPV). The design of the traverse system is depicted in Fig. 4.2. The path of the traverse was parallel to the line of the microphones that were mounted on the horizontal arm of the array holder (see Fig. 4.2). The scanning and fixed microphones had offset distances of 6 mm, approximately, as illustrated in Fig. 4.3.

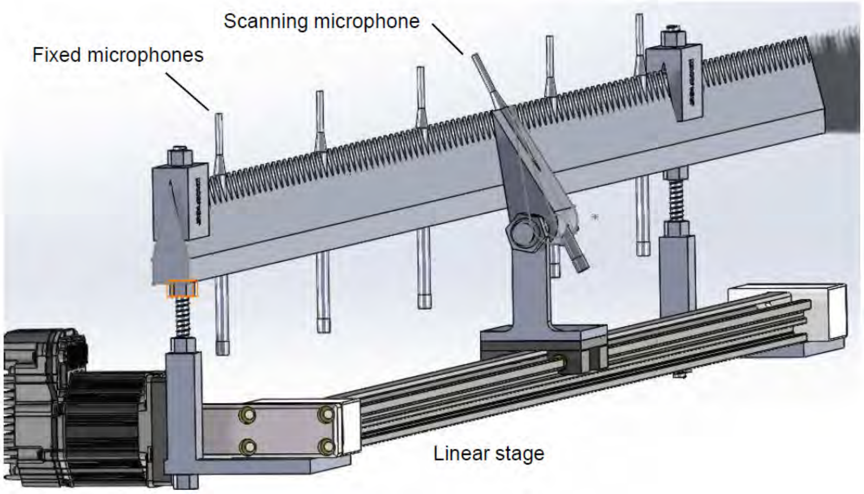

Figure 4.2: Design of the linear traverse system.

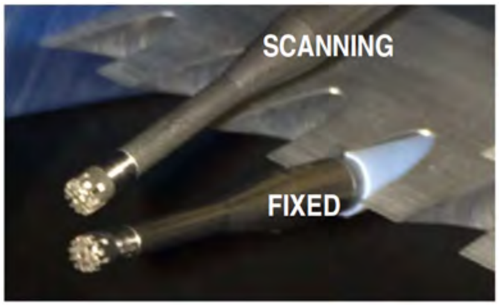

Figure 4.3: Fixed and scanning microphones at their closest spacing of 6 mm, measured from the cartridge centers.

4.2 Noise Sources

This work features several studies that used distinct aeroacoustic sources in conjunction with the continuous-scan paradigm presented in the preceding sections. The sources include an impinging jets source (IJS), which is an approximation to a point source, a subsonic jet and an underexpanded supersonic jet that issued from a convergent nozzle. The IJS is utilized to assess the performance of the continuous-scan techniques and deconvolution and compare it with that of an array that utilizes fixed sensors only. The last two sources are of particular interest within the context of commercial aviation and the military, respectively. Several reflector surfaces were used in conjunction to the supersonic jet to change the screech emission dynamics.

4.2.1 Impinging Jets Source

The impinging jets rig, shown in Fig. 4.4, uses the collision of four small round jets to create an approximation to a point source. The design is similar to that used by Gerhold *et al.* [90]. The jets issued from tubes with internal diameter of 2.4 mm, and were supplied by air at room temperature and pressure of 205 kPa. The selected total pressure resulted in the tubes being choked, with an exit Mach number of ~ 1, and a Reynolds number of approximately

4.2×10^4 based on the internal diameter.

Figure 4.4: Impinging jets source.

4.2.2 Subsonic Jet

The subsonic jet used in this work issued from a convergent nozzle with exit diameter $D =$ 14.22 mm. It was supplied by air at room temperature and pressure of 171 kPa, producing an exhaust at Mach number $M = 0.9$ and velocity $U = 285$ m/s. The jet Reynolds number, based on exit diameter, was 3.6×10^5. A rectangular aluminum plate was integrated with the jet to study the effects of shielding. The plate had a thickness of 3 mm, span of 610 mm ($42.9D$), and chord length c of 255 mm ($17.9D$). A schematic of the setup for the subsonic jet experiments is depicted in Fig. 4.5. The transverse distance H from the jet axis to the plate was kept constant at 29 mm ($2.1D$). The axial location L of the trailing edge from the nozzle exit plane took the values $L = 28.4$ mm, 71.0 mm, and 113.6 mm ($2D$, $5D$ and $8D$, respectively). The trailing edge of the plate for $L = 8D$ was located at an angle of 11.3° relative to the nozzle lip line proximal to the plate, a value significantly larger than the spreading rate of the shear layer. Mean velocity measurements for the same jet [91] show that the edge of the jet, defined as the surface on which the mean axial velocity equals $0.05U$, expands at an angle of $\sim 7°$ relative to the lip line. For $L = 8D$, the gap between the plate and the edge of the jet is $\sim 0.6D$. Therefore, the jet was not scrubbing the plate for any of the shielding configurations.

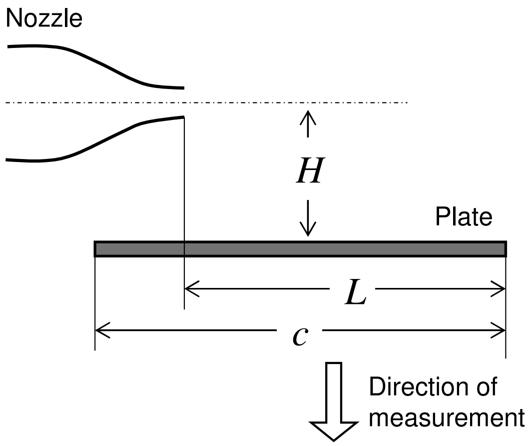

Figure 4.5: Schematic of convergent nozzle integrated with plate used in the subsonic jet experiments.

4.2.3 Supersonic Jet

The supersonic jet issued from a convergent nozzle with exit diameter $D = 14.22$ mm and lip thickness of 0.4 mm. The coordinates of the nozzle are shown in Fig. 4.6. The nozzle was supplied by air at room temperature at a variety of total pressures p_0 in order to identify the highest-amplitude screech tones, always operating in an underexpanded regime. Several reflector surfaces were mounted at the exit of the nozzle as depicted in Fig. 4.7. All the surfaces had the same base diameter of 60.0 mm ($4.22D$) and cone half-angles of 90° (flat plate), and 60°. The surfaces were 3D printed using a Formlabs Form 2 printer, and polished so that their surface roughness was much smaller than the screech acoustic wavelength. Structures upstream of the nozzle were covered with anechoic foam to minimize any reflections towards the nozzle.

Operation of the isolated nozzle (without reflector) at sweep of total pressures, from 239 kPa to 335 kPa, identified strong screech tones within a narrow range of total pressure associated with fully-expanded Mach numbers of $1.32 \leq M_j \leq 1.34$, or $289 \leq p_0 \leq 297$ kPa. As such, a total pressure of 297 kPa was selected in this work. The corresponding fully-expanded jet velocity was $U_j = 397$ m/s. The Reynolds number based on nozzle exit diameter was

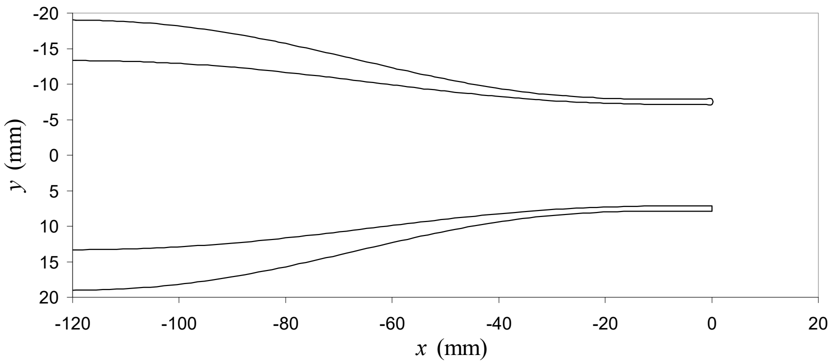

Figure 4.6: Nozzle coordinates on symmetry plane.

6.5×10^5. During each experimental run, the total pressure was held to within 1% of its target value.

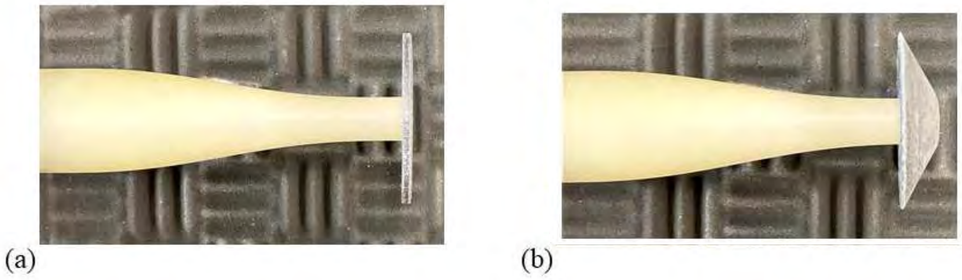

Figure 4.7: Photographs of the nozzle and the reflectors. (a) 90°; and (b) 60°.

4.3 Signal division and Array Layouts

The continuous-scan techniques presented in this work entailed division of the signals into blocks. Two block schedules were investigated to demonstrate the benefits of the tailored signal processing presented in the preceding chapter. One of the block schedules utilized a fixed block size while the second used a variable block size. The first schedule, $\mathrm{CS}_{K=120}$, utilized a block size $N_B = 260000$ with overlap $\sigma_B = 0.9$. The total number of blocks was $K = 120$, as given by Eq. 3.10. This configuration entails a relatively small number of blocks with a size close to the maximum size allowed, as dictated by Eq. 3.4. As discussed in Chapter 3, the large block size is expected to result in information loss at high frequency. The configuration is also predicted to yield a lower spatial resolution due to the limited number of blocks used as it does not significantly increase the number of closely-spaced measurement points. The second schedule, referred as CSV, utilized variable block size following the guidelines of Fig. 3.5. In particular, setting $T/\delta = 1.7$, $\sigma_S = 0.5$, and $c_{\text{cov}} = 5$ in Eq. 3.9 gives $S_{\min} = 16$, which satisfies the minimum criterion for number of segments discussed in Chapter 3. In turn, Eqs. 3.6 and 3.7 give $N_{B_{\min}} = N^*_{B_{\max}} = 17N_{\text{FFT}}$. The block division displayed in Table 4.1 follows approximately this formula. All the continuous-scan methods used the N_{FFT} schedule of Table 4.1 and a frequency-dependent Gaussian window with $c_\lambda = 0.2$. The source region of interest was -0.4 m $\leq x \leq$ 1.0 m.

Frequency Range (kHz)	N_{FFT}	N_B	T (s)	K	σ_B
0-30	2048	36000	0.144	166	0.50
30-60	1024	17000	0.060	352	0.50
60-90	512	8200	0.032	750	0.50
90-120	256	4100	0.016	1480	0.50

Table 4.1: Block division for continuous-scan method (CSV).

Phased-array measurements were conducted using different subsets of the fixed microphones in combination with the scanning microphone. Table 4.2 shows the number of sensors used, the polar angle coverage, and the array center polar angle θ_c for each layout. The array center angle is defined as the average angle of the fixed sensors. The polar angle coverage was slightly different for the fixed and scanning microphones. The impinging jets source and the subsonic jet, including its shielding configurations, were imaged using array layout P. The supersonic jet and all of the reflector configurations were imaged using layout S.

The coordinates of the fixed microphones and the scanned region for array layouts P and S are shown in Fig. 4.8. The total scanned region was 900 mm for both cases, with the sensor traversing at a steady-state velocity of approximately 75 mm/s. The total experiment time

Layout	$\mathcal{M}_f$	$\mathcal{M}_s$	θ range Fixed	θ range Scanning	θ_c
P	11	1	36.0° to 97.3°	50.0° to 97.0°	66.7°
S	13	1	51.1° to 97.8°	52.2° to 100.8°	74.5°

Table 4.2: Array layouts P and S.

was 12 seconds, resulting in the collection of 3×10^6 samples.

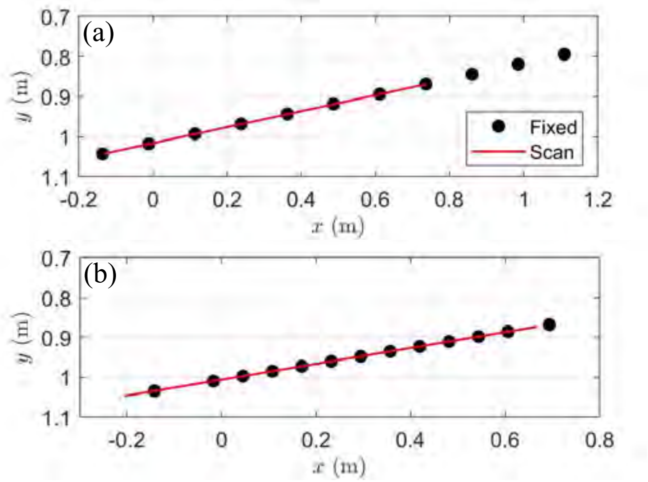

Figure 4.8: Coordinates of array layout P (a) and S (b). Fixed microphones indicated in black and scanned region indicated in red.

4.4 Tracking and Synchronization of the Scanning Sensor

The position of the scanning sensor must be properly acquired and monitored to ensure the microphone trace and the microphone pressure signals are synchronized. The source-sensor position is a fundamental parameter in beamforming. The continuous-scan approach entails division of the pressure signals into blocks. These blocks can be thought of as "virtual sensors", as described in Chapter 2, the coordinates of which are at their geometric centers. Errors on the position of the scanning microphone are particularly detrimental to the resolution of the noise source maps when utilizing dense block distributions, such as those presented in Table 4.1, as the number of virtual references used surpasses that of the fixed sensors. The following lines summarize the synchronization of the pressure signals with the scanning microphone and the tracking of its position.

The signals from the microphones, scanning and fixed, are sampled simultaneously at 250 kHz, as described previously. A synchronization signal and a position time-trace is also recorded in conjunction with the microphone pressure signals. The synchronization signal is created by splitting the voltage input of the motor moving the scanning sensor (ClearPath MCPV) into a channel connected to the Data Acquisition Board (DAQ). The voltage signal rises when the motor is activated and is equal to 0 V otherwise. This synchronization signal is used to detect the exact instant at which the scanning sensor starts moving by detecting the time instant of the initial voltage rise. The synchronization signal might be filtered using a high-pass Butterworth filter at 350 Hz to obtain a voltage peak when the motor is activated, as seen in Fig. 4.9b. The experimental data that is acquired before the initial voltage rise is always discarded. In addition, more data points than necessary are acquired to ensure signals are properly acquired for the full duration of the experiment. With knowledge of the total scanning time, the data recorded after the scanning sensor stops is also discarded. Figure 4.9 shows an example of a pressure and synchronization signal for an experiment of a duration of 8.4 seconds. The blue part of the pressure plot includes the data that is utilized to obtain the noise source maps. The activation instant can be clearly seen in image b.

Two systems are used to track the position of the scanning sensor and generate the position time-trace signal. First, ClearPath MSPV software is used to record the coordinates of the scanning sensor at all time instances. The position of the scanning sensor is determined from the encoder signal of the motor powering the traverse. At the same time, a second system consisting of a laser-based distance measurement device (SICK OD1000) is used. The laser utilizes the triangulation principle to determine the position of the target: a point light

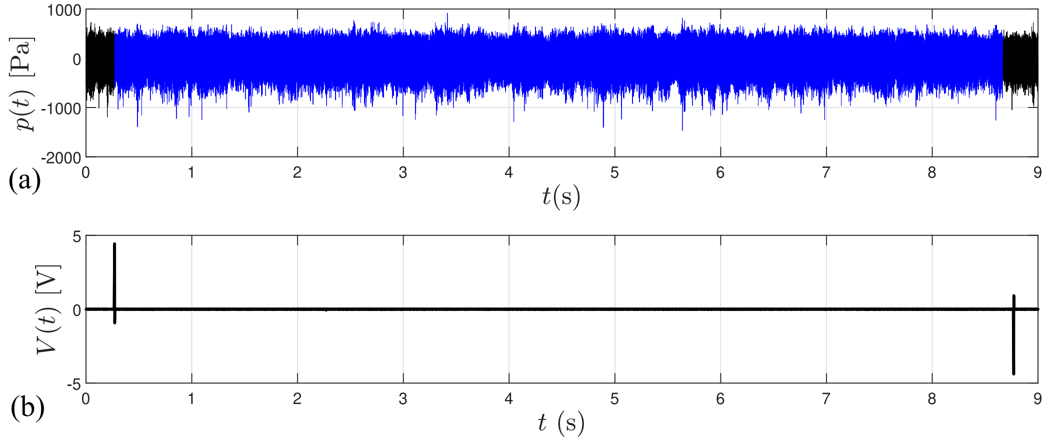

Figure 4.9: Example of the synchronization of the microphone traces with the position. (a) Pressure signal; (b) Synchronization signal.

source is projected onto a small body attached to the scanning sensor. The distance is then calculated based on the angle of the reflected light. The laser-based measurement channel is also connected to the DAQ and sampled simultaneously with the rest of the channels. Figure 4.10 shows an example of the trajectory of the scanning sensor, obtained using the ClearPath MSPV software signal and SICK OD1000. The image on the left represents the trajectory of the scanning sensor. The image on the right shows the error between the ClearPath motor encoder and SICK OD1000. The signal from the ClearPath motor encoder is usually utilized to produce the position time-trace.

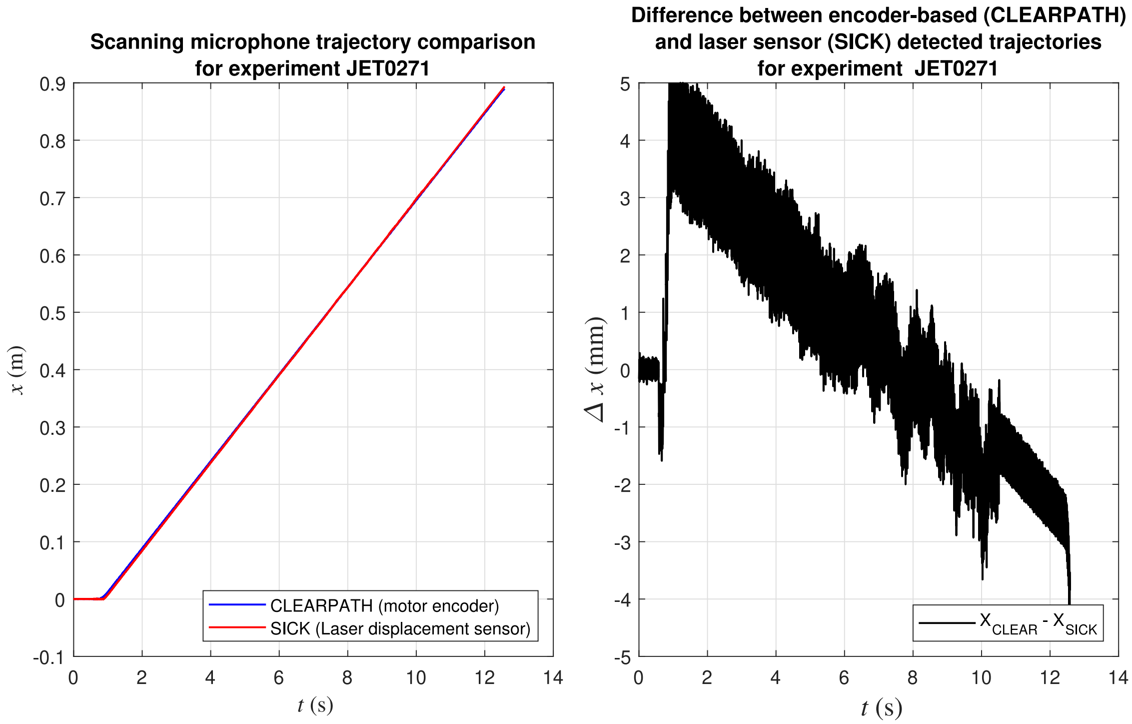

Figure 4.10: Scanning microphone trajectory comparison for a given experiment.

Chapter 5

Results

Results for the acoustic sources of this work are presented next. The results include a combination of far-field SPL spectra, and the noise source maps. In addition, the expected performance of the continuous-scan methods in conjunction with the signal processing guidelines is evaluated. The distribution of the impinging jets source shows a highly localized source. The noise source distribution of the subsonic jet shows agreement with past experimental works [29]. The shielding surfaces demonstrate to be an effective way of suppressing high-frequency noise. However, additional low-frequency noise sources are generated due to an energy conversion from hydrodynamic to acoustic waves at the trailing edge of the plate. The source distribution of the supersonic jet flow is of interest given its intricate flow pattern containing large-scale and small-scale turbulence structures and the shock-cells. The continuous-scan methodologies are able to discern the shock-cell spacing and predict the location of the screech sources. Finally, upstream reflectors are used to change the emission dynamics of the jet flow.

Parts of this chapter are a partial reprint and adaptation of Morata, D., and Papamoschou, D., *"Advances in the Direct Spectral Estimation of Aeroacoustic Sources Using Continuous-*

Scan Phased Arrays", AIAA Paper 2021-0215, doi: 10.2514/6.2021-0215; Morata, D., and Papamoschou, D., *"Effect of Nozzle Geometry on the Space-Time Emission of Screech Tones"*, AIAA Paper 2021-2306, doi: 10.2514/6.2021-2306; and Morata, D., and Papamoschou, D., *"Extension of Traditional Beamforming Methods to the Continuous-Scan Paradigm"*, AIAA Paper 2022-1154, doi: 10.2514/6.2022-1154. Excerpts from the chapter have been submitted as a full-length journal paper to the Journal of the American Institute of Aeronautics and Astronautics (AIAA Journal) as *"High-Resolution Continuous-Scan Beamforming"*, with Morata, D., and Papamoschou, D., as the authors, as of April 2nd, 2022.

5.1 Expected Performance of the Beamforming Methods

The array point spread function (Eq. 2.14) affects the spatial resolution of the beamformed images, as described in the preceding sections. In order to improve the spatial resolution of the array, the PSF should be free of sidelobes that will create artificial sources in the noise source map. These artificial sources lower the spatial resolution of the noise localization process and cause the DAS beamformed maps (Eqs. 2.9, 2.49, 2.63, and 2.74) to not truly represent the real noise source distribution.

The continuous-scan paradigm reduces the sidelobe levels significantly. The reduction is obviously dependent on the block schedule that is utilized (e.g., a relatively coarse block distribution will not suppress the sidelobes as much as a fine distribution [27]). The PSFs of the continuous-scan approaches of this work are studied next. They have been computed using array layout S (Table 4.2), and using the corresponding block distribution from Table 4.1 depending on the frequency of interest (i.e., using the optimized block schedule). The PSF of the fixed array (FS) is also included for reference. No signal segmentation is required for its calculation. The shape of the PSFs calculated for array layout P were of a shape relatively similar to that of layout S.

Typically, the PSF is characterized using two parameters. These variables are the main lobe beamwidth and the relative sidelobe level [92]. With regard to the main lobe beam width, Brooks and Humphreys [12] found it to be inversely proportional to frequency

$$B_{-3\text{dB}} \approx CR/(fL) \tag{5.1}$$

where L is the aperture of the array, R is the average distance between the array and the measurement line, and C is an experimentally-found constant [63]. The experimental constants for array layouts P and S are shown in Table 5.1.

Layout	L (m)	R (m)	C (m Hz)
P	0.8	0.95	298.12
S	0.85	1.02	308.34

Table 5.1: Array geometric constants.

The dependency on frequency of the main lobe beamwidth for array layouts S and P is shown in Fig. 5.1. The main lobe beamwidth is an indication of the minimum distance at which distinct sources must be situated in order to separate them properly using traditional beamforming techniques. As expected, the beamwidth is wider at low frequency and reduces significantly at high frequency [92]. It is observed that both array layouts had relatively similar main beamwidths given their geometric constants being alike (Table 5.1).

The relative sidelobe level is shown in Fig. 5.2. The image displays the PSF at the focal point $x = 0$ m, calculated using the various continuous-scan methodologies introduced in this work, and for the frequency range of interest. The PSF has been normalized for every frequency to allow for a fair comparison of the sidelobe levels. It is seen how all the continuous-scan methodologies suppress the sidelobes significantly when compared to FS. It was verified that

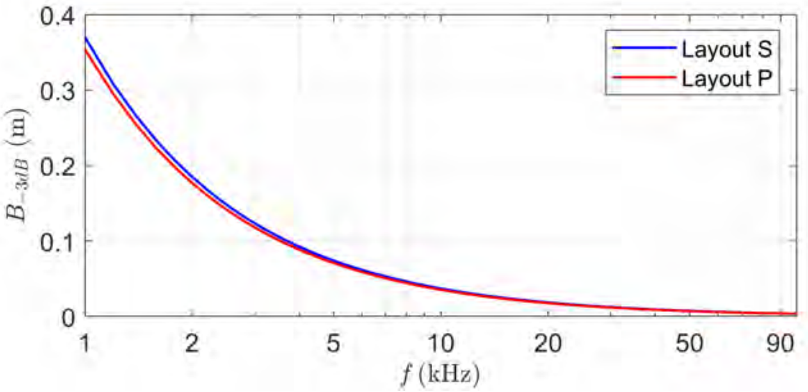

Figure 5.1: Main lobe beamwidth for array layouts S and P.

no strong sidelobes at high frequency appeared for $x < -0.3$ or $x > 0.5$ m when using CSSM, CSMC or PFD with the optimized block schedule of Table 4.1.

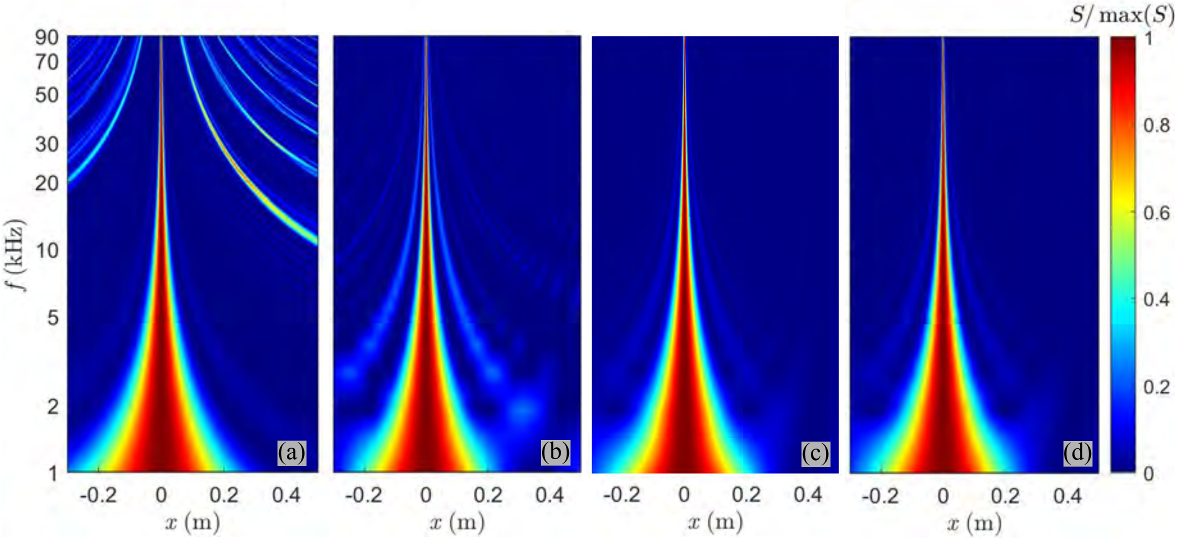

Figure 5.2: Normalized point spread function at $x = 0$ for the frequency range of interest obtained using the optimized block schedule. (a) FS; (b) CSSM; (c) CSMC; and (d) PFD.

It is instructive to examine the performance of the distinct continuous-scan methods in more detail. This is done in Figs. 5.3, 5.4, and 5.5. The images display a slice of Fig. 5.2 at a frequency of 15, 50 and 85 kHz, respectively. The sidelobe suppression is evident in the figures. At a frequency of $f = 15$ kHz, notice there is a strong sidelobe near $x = 0.4$ m when using FS (black). The prominent sidelobe is completely eliminated when using CSSM (red), CSMC (blue), and PFD (green). The CSMC and PFD produce PSFs of virtually the same quality and suppress the sidelobes that are neighboring the main beam that are present when using the CSSM technique.

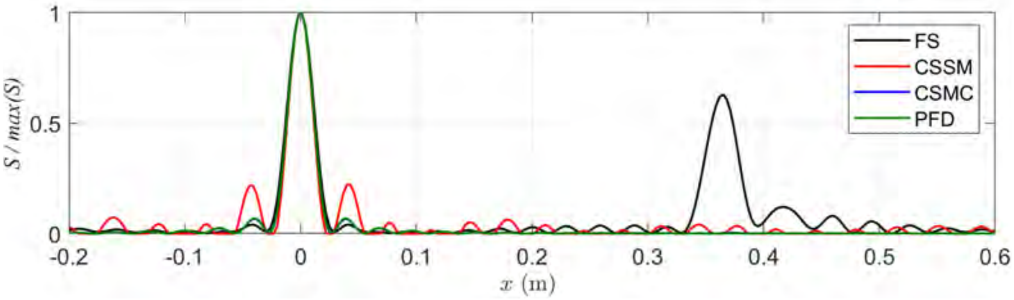

Figure 5.3: Normalized point spread function at $x = 0$ at 15 kHz.

A similar sidelobe suppression behavior is seen at a frequency of 50 kHz (Fig. 5.4), with the sidelobes for FS being significant at multiple positions.

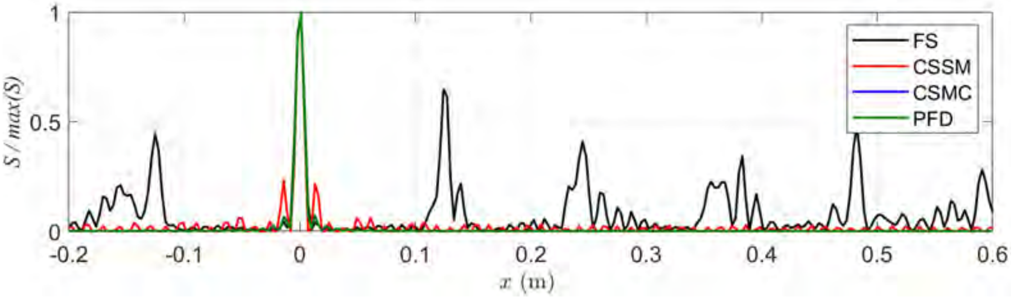

Figure 5.4: Normalized point spread function at $x = 0$ at 50 kHz.

Figure 5.5 shows the normalized point spread function at $x = 0$ m obtain with all the beamforming methods of this thesis. The plots have been divided into four distinct sub-figures to aid the visualization of the results given the high number of sidelobes present when utilizing the FS technique. High frequencies are noticeably contaminated as a consequence of the spatial aliasing produced by the geometric distribution of the microphone array with FS. This translates into strong distortions of the source distribution at high frequency. The sidelobes are again significantly mitigated with all the continuous-scan methodologies of this work. Notice how the CSMC and PFD overperfom the CSSM technique.

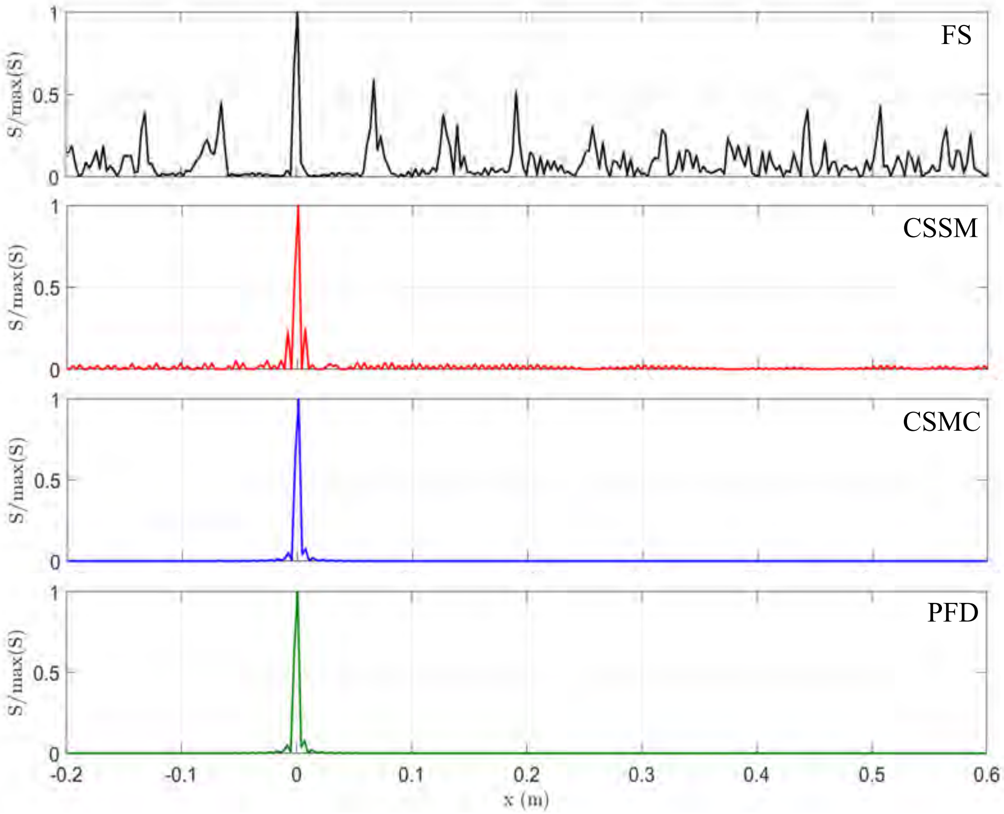

Figure 5.5: Normalized point spread function at $x = 0$ at 85 kHz for FS, CSSM, CSMC and PFD.

The figures displayed in this section demonstrate the ability of the continuous-scan methods combined with the optimized signal processing to suppress the sidelobes that are inherent to the PSF, which result in noise source maps with a spatial resolution that is significantly improved compared to utilizing FS. However, the signal segmentation chosen has consequential effects on the quality of the noise source maps.

5.1.1 Effect of the Signal Processing

The effects of the signal processing (i.e., the block schedule) on the spatial resolution of the noise source maps is studied next. The images shown in this section are analogous to Figs. 5.3, 5.4, and 5.5 but have been obtained with the coarse block schedule ($\text{CS}_{K=120}$).

Figure 5.6 shows the PSF at $f = 15$ kHz obtained with $\text{CS}_{K=120}$. It can be seen how it is almost identical to that obtained with the variable block distribution (CSV). The sidelobes are always more prominent at high frequency and the combination of the continuous-scan methods and the coarse block schedule already does a good work at suppressing them.

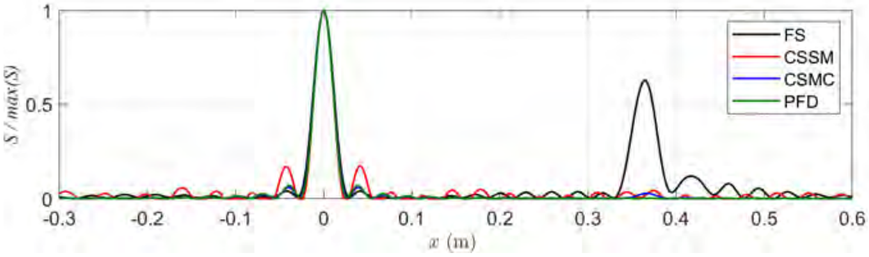

Figure 5.6: Normalized point spread function at $x = 0$ at 15 kHz with $\text{CS}_{K=120}$.

A certain degree of sidelobe contamination arises for CSSM, CSMC and PDF near $x = 0.5$ m at a frequency of $f = 50$ kHz (Fig. 5.7). This was not observed when using the CSV block schedule and is related to the lower number of closely-space microphones, which produces a spatial aliasing. In other words, the microphones are not spaced at, at least, 0.5λ.

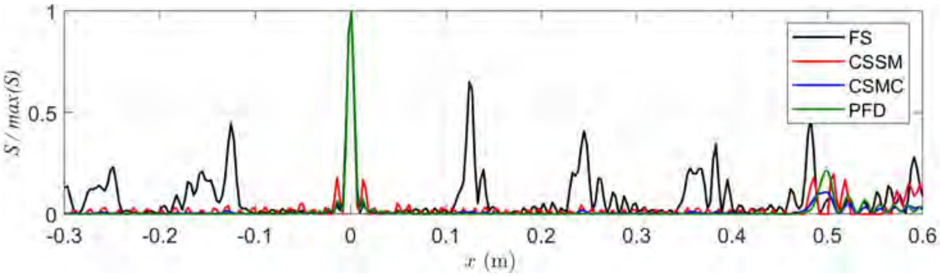

Figure 5.7: Normalized point spread function at $x = 0$ at 50 kHz with $\text{CS}_{K=120}$.

Sidelobes become more prominent at a frequency of $f = 85$ kHz. Similarly as in the previous section, the plots have been divided in four sub-figures to aid the visualization of the results. Relatively strong sidelobes near 0.4 and 0.5 m can be observed for CSSM. The sidelobes appear suppressed with CSMC and PFD when compared to CSSM. Nevertheless, notice that the coarse block schedule still over performs when compared to the use of FS.

The previous figures demonstrate the vital role of the signal processing in increasing the

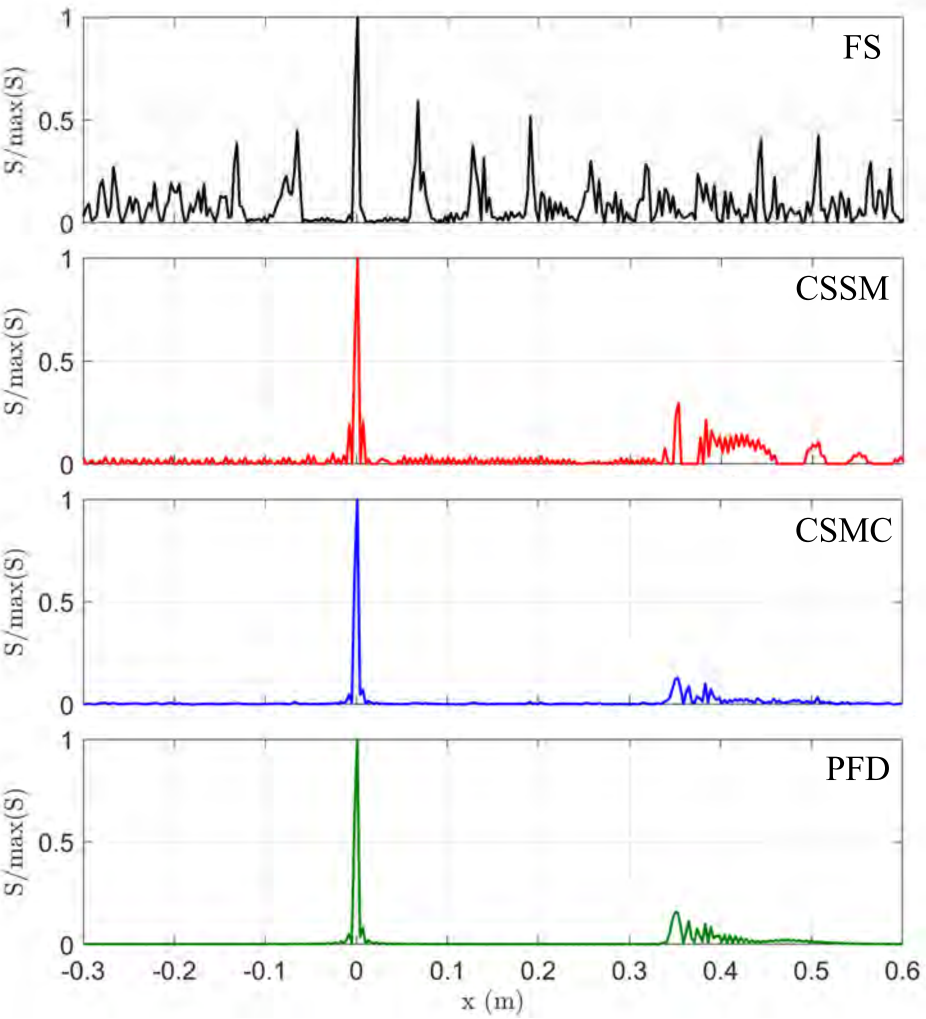

Figure 5.8: Normalized point spread function at $x = 0$ at 85 kHz with $\mathrm{CS}_{K=120}$ for FS, CSSM, CSMC and PFD.

number of closely-space microphones to prevent spatial aliasing [60]. Thus, the noise source maps presented in this work have been obtained by exploiting the full potential of the continuous-scan technique (i.e., using the block schedule of Table 4.1).

5.2 Impinging Jets Source

The impinging jets source is studied next, and the exact performance of the distinct continuous-scan approaches and deconvolution methods is evaluated experimentally. In addition, the precision of the PFD technique is briefly analyzed by using information from the phase-referencing matrix.

5.2.1 Sound Pressure Level

Figure 5.9 shows the lossless narrowband SPL spectra for the impinging jets source, measured with the fixed microphones, at various polar angles. The acoustic field is broadband, peaking near 15 kHz. The emission is moderately directive, with the spectral peak being the highest near $\theta = 90°$.

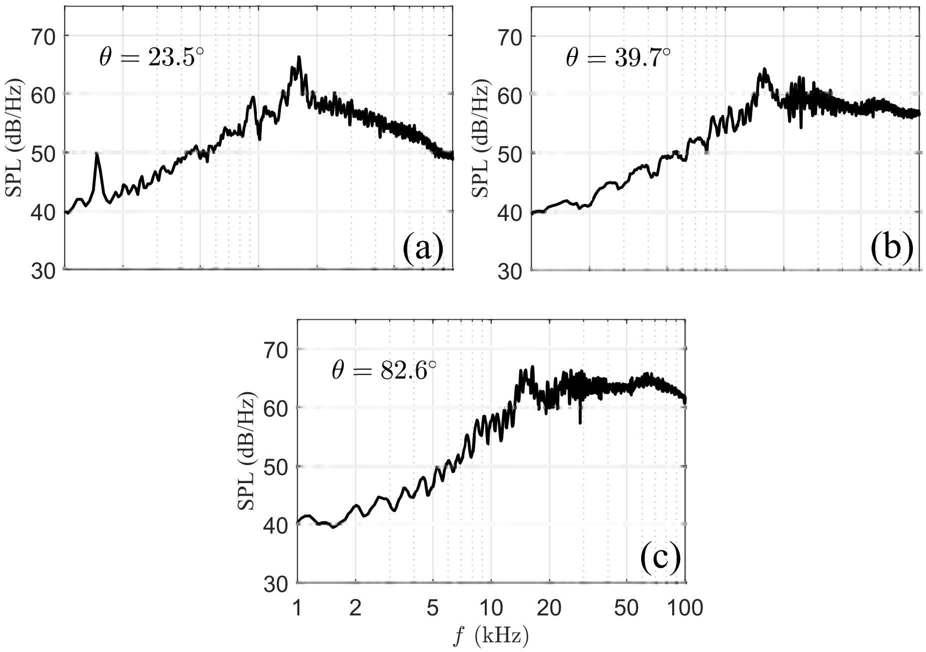

Figure 5.9: SPL spectra for the impinging jets source at polar angles $\theta =$ (a) 23.5°; (b) 39.7°; and (c) 82.6°.

5.2.2 Noise Source Distribution

Figure 5.10 displays noise source maps computed with array layout P of Table 4.2, using the DAS algorithm and the optimized block schedule for the continuous-scan approaches. A dynamic range of 20 dB is used, with the local maximum set to 0 dB. The IJS is an approximation to a point source, as stated in the preceding section. As such, it is expected that the source becomes a vertical line centered near $x = 0$ m in the frequency-space plots. It is evident that the noise source map obtained with fixed references only (a) suffers from strong sidelobes and a low spatial resolution. Notice how there are strong artificial sources outside the vertical line at $x = 0$, becoming more prominent at high frequency, due to the spatial aliasing introduced by the measurement, as described previously. All continuous-scan approaches (CSSM, CSMC, and PFD) obtain noise source maps with a high degree of spatial resolution and without the presence of artificial sources caused by the sidelobes. Notice how the source appears slightly sharper when utilizing the CSSM approach when compared to CSMC and PFD. The figure evidences the potential of the continuous-scan techniques of this work at obtaining high-resolution noise source maps using an experimental point source.

Additional detail on the performance of all beamforming methods is shown in Fig. 5.11. The figure shows a slice of the noise source distributions obtained with DAS, normalized by their peak level, at several frequencies. Images a, b, and c have been obtained for a frequency of 15, 50 and 85 kHz, respectively. The sidelobes are evident in all the noise source distributions obtained with FS, being prominent at high frequency. The sidelobe levels appear to be comparable to the level of the source. The noise source distributions obtained using the continuous-scan approaches of this work are practically devoid of sidelobe contamination at all frequencies and are able to perfectly localize the source. In addition, note how the source distribution obtained with CSMC and PFD is virtually identical.

It is instructive to examine how precisely represented the source is when using the PFD

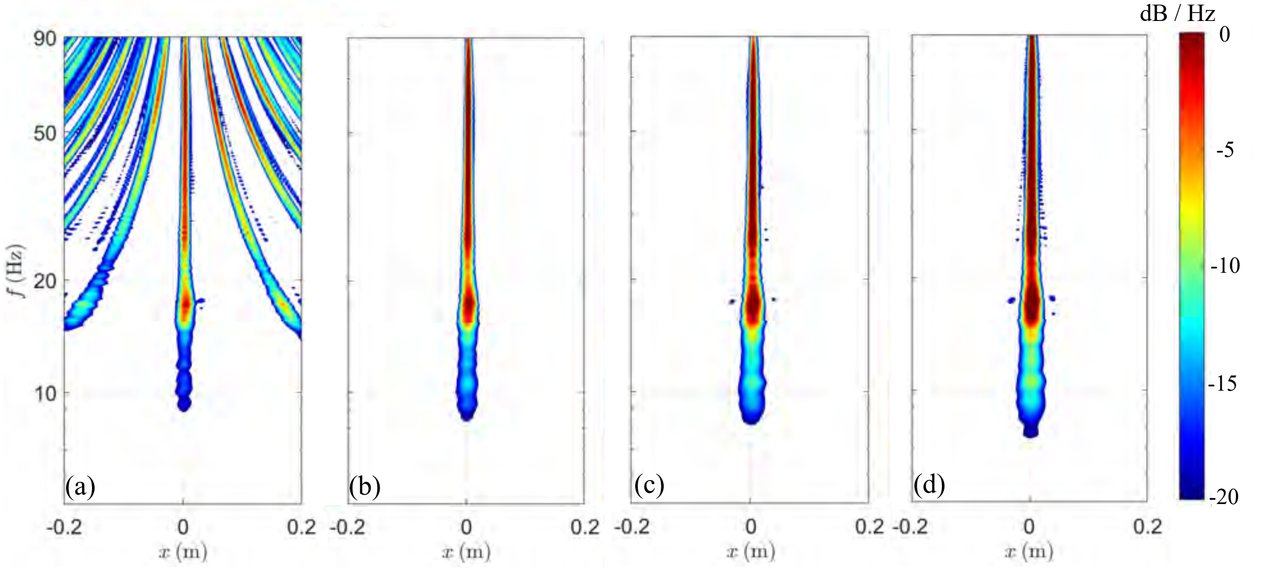

Figure 5.10: DAS noise source maps of the IJS obtained using different methods. (a) FS; (b) CSSM; (c) CSMC; and (d) PFD.

technique. The accuracy of the PFD relies on having a sufficient number of microphones in the far-field that are able to capture the number of independent acoustic sources at all instances. The number of sources needed to accurately represent the acoustic field can be inferred from the difference between the ranked singular values of the phase referencing matrix $\mathbf{\Sigma}_{ff,T}$ (Eq. 2.66) [79, 26, 28]. Figure 5.12 shows the ranked odd singular values (1, 3, 5, etc.) of the IJS experiment. It can be seen that there is a significant difference between the highest and the lowest singular values of the source for all frequencies of interest in this work. In particular, there is more than one order of magnitude difference between the first and the third highest singular value. As such, it is expected that the number of fixed sensors used for the IJS experiment is sufficient to fully characterize the acoustic source. The accuracy of the PFD technique could also be evaluated by employing an approach similar to that used by Lee and Bolton [79], in which the number of partial fields required to construct the total acoustic field, related to the number of fixed references, is analyzed utilizing the virtual coherence function. The performance of the CSMC is similar to that of PFD and will be further explored in the next sections by employing the far-field complex coherence

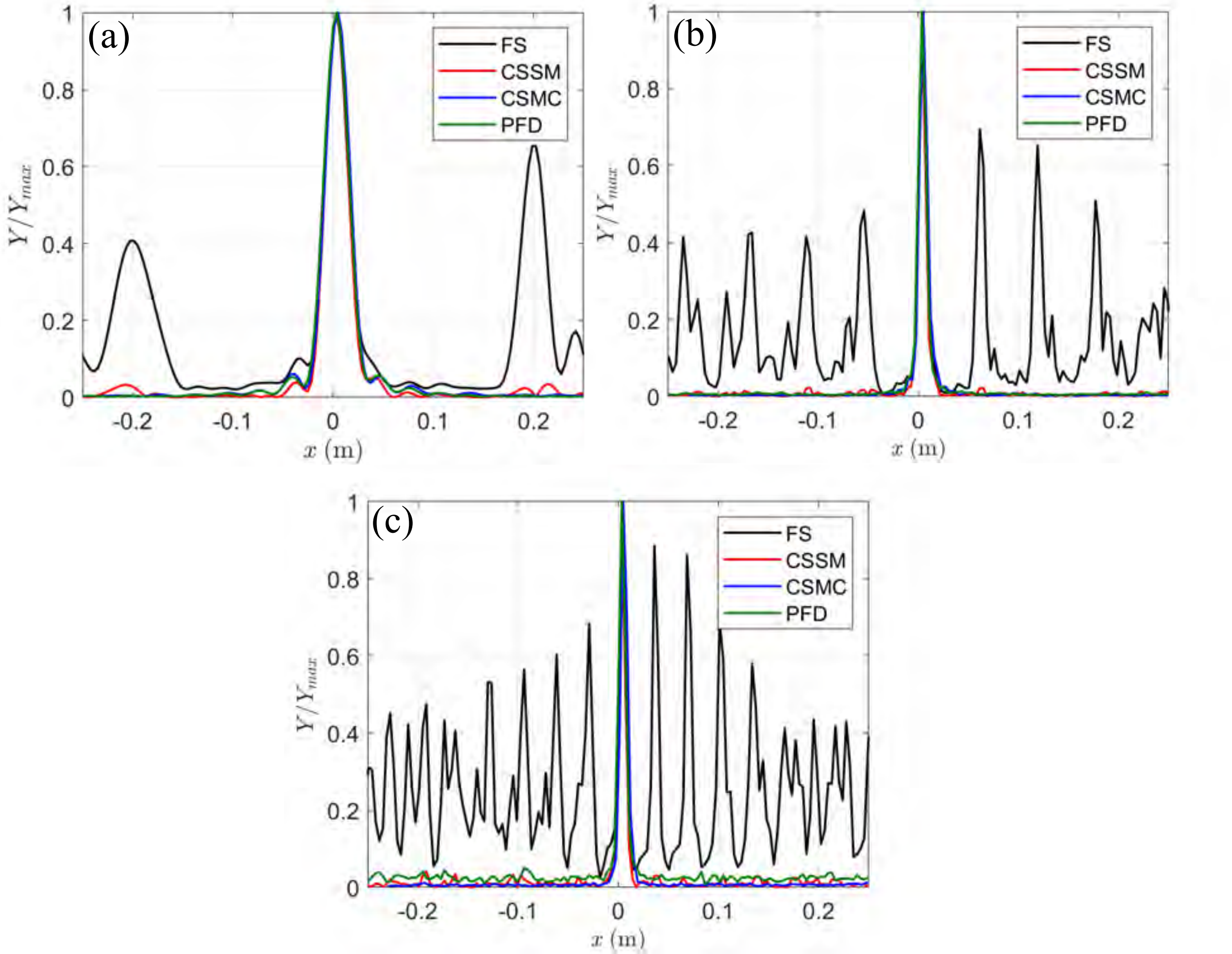

Figure 5.11: Normalized source distribution obtained with DAS at several frequencies: (a) 15 kHz; (b) 50 kHz; and (c) 85 kHz.

function.

The source distribution can be improved using deconvolution. This is first performed on the DAS map obtained using FS and is shown in Fig. 5.13. It is seen how deconvolution further sharpens the noise source distribution and mitigates the sidelobes to a certain extent. The DAMAS and R-L approaches show a moderate presence of the sidelobes at high frequency. They appear to be suppressed to a greater extent when using R-L over DAMAS, and the source appears to be more continuous when using the R-L approach. The DAMAS deconvolution creates a speckle-like distribution, which is an issue that has been

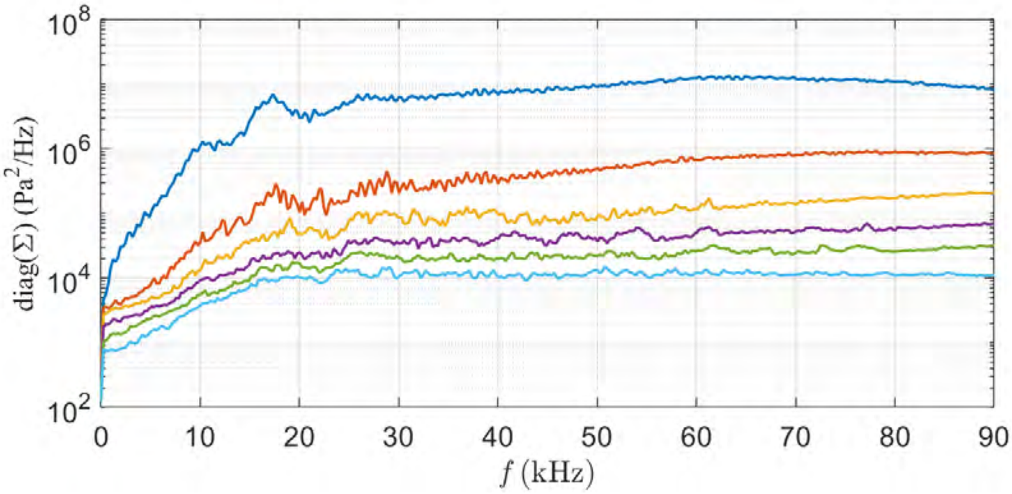

Figure 5.12: Ranked odd singular values (1, 3, 5, etc.) for the IJS.

seen in past experimental studies [28]. The highest sidelobe mitigation is obtained when using CLEAN-SC given that the relationship between the main lobe and the sidelobes is explicitly accounted for in its formulation. However, the map results in a source that is not as sharply localized. This is consistent with the trends seen in past works [28]. The source distribution at a frequency lower than 15 kHz is not well-defined using DAMAS or the R-L approach.

Deconvolution can also be performed for the continuous-scan approaches that obtain a full CSM (CSMC and PFD). Figure 5.14 shows the deconvolved DAS map obtained through CSMC. It is seen how the sidelobes are completely eliminated using all deconvolution approaches and the source is particularly sharp when using DAMAS and R-L.

Figure 5.15 is analogous to the previous one except that the CSM has been obtained with PFD. Similar trends to those described for the CSMC approach are observed for all the deconvolution methods.

The performance of the three distinct deconvolution methods that are utilized in this thesis is evaluated in Fig. 5.16. The figure shows a slice of the noise source distributions obtained

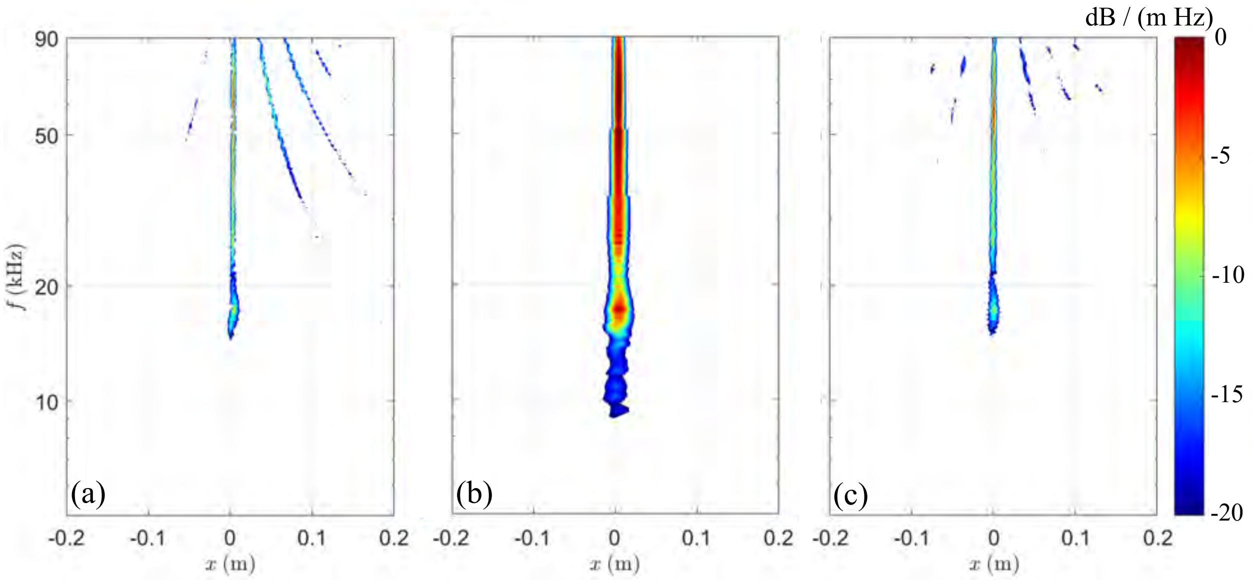

Figure 5.13: Deconvolved DAS noise source maps of the IJS obtained with FS using (a) DAMAS; (b) CLEAN-SC; and (c) R-L.

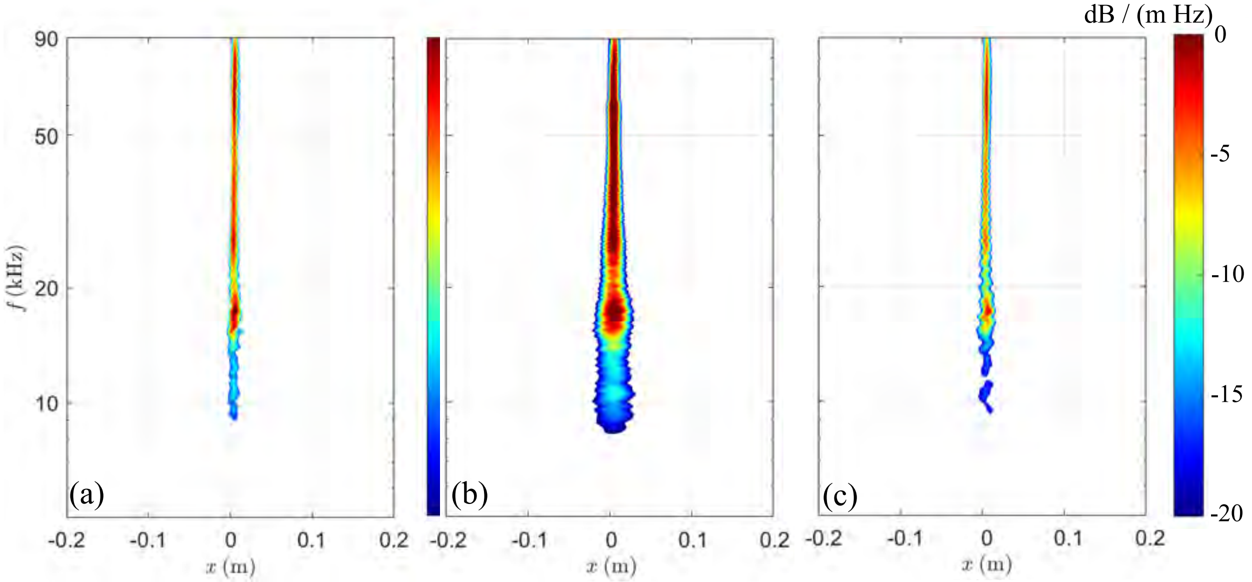

Figure 5.14: Deconvolved DAS noise source maps of the IJS obtained with CSMC using (a) DAMAS; (b) CLEAN-SC; and (c) R-L.

with PFD and deconvolution, normalized by their peak level, at several frequencies. The frequencies are the same as those shown in Fig. 5.11. The tendency of DAMAS to create a source with a speckle-like nature is seen for $f = 15$ kHz, and R-L appears to perform

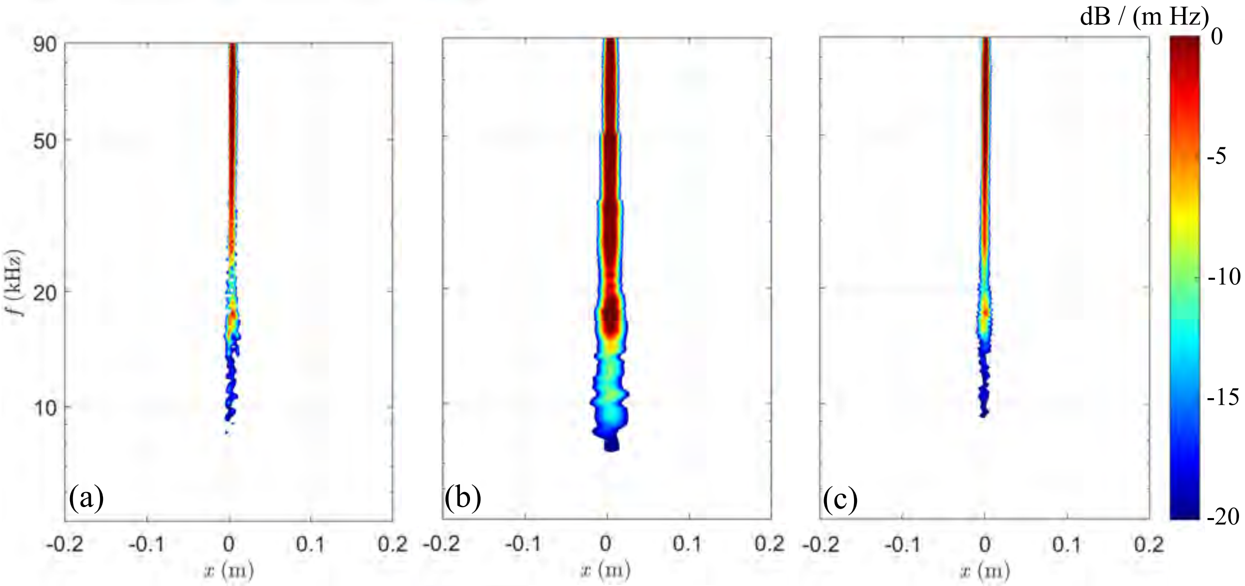

Figure 5.15: Deconvolved DAS noise source maps of the IJS obtained with PFD using (a) DAMAS; (b) CLEAN-SC; and (c) R-L.

better. CLEAN-SC results in a source that appears wider when compared to DAMAS and R-L for all the frequencies studied here. Finally, it is seen how DAMAS and R-L result in similar noise source distributions at high frequency. Similar trends were observed for the deconvolved noise source distributions obtained with CSMC and have not been included in this section for brevity.

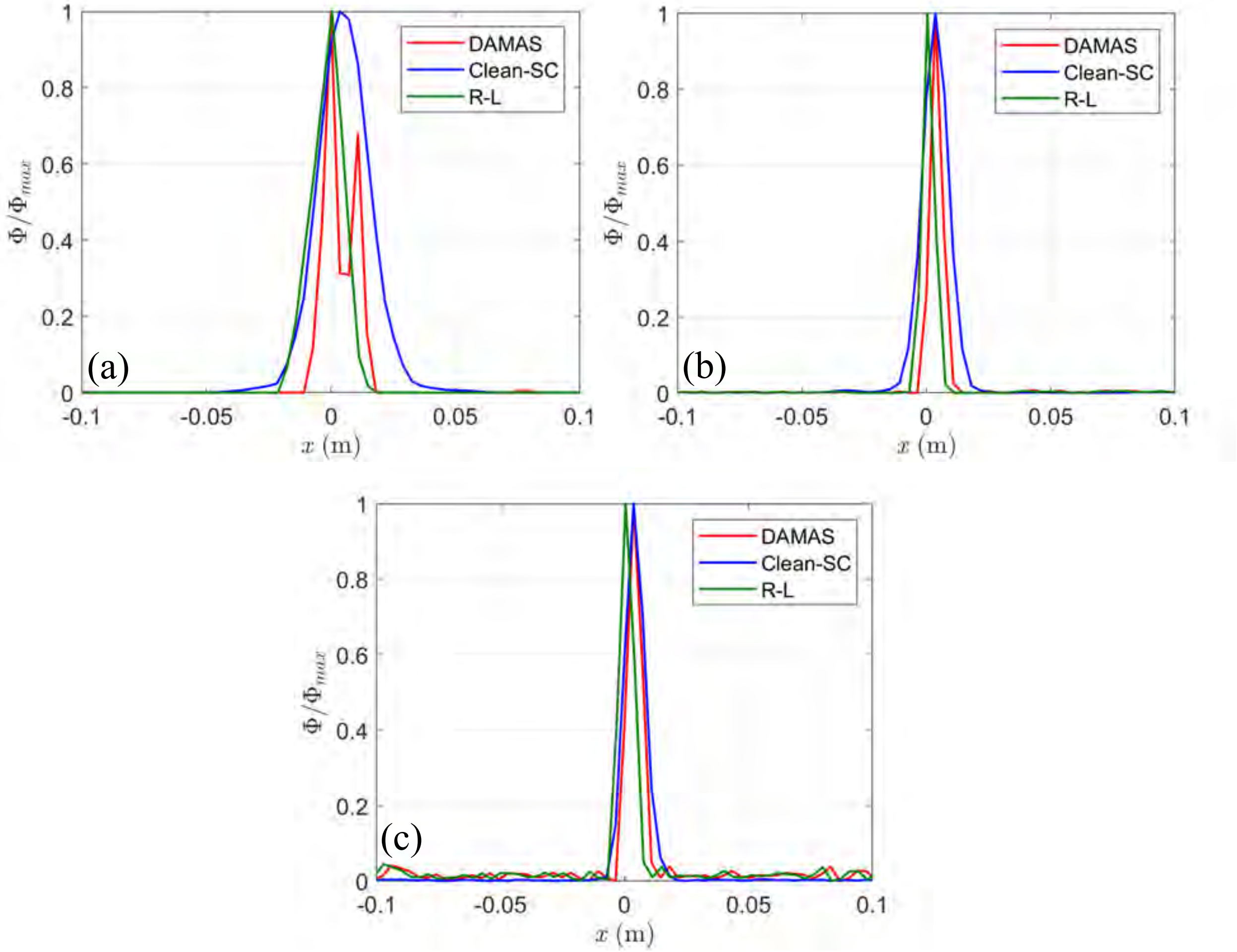

Figure 5.16: Normalized source distribution obtained with PFD and the distinct deconvolution algorithms at several frequencies: (a) 15 kHz; (b) 50 kHz; and (c) 85 kHz.

5.3 Subsonic Jet Flow

The subsonic jet flow issuing from a convergent nozzle is analyzed next. This section displays the corrected SPL together with the noise source distributions obtained with distinct methods for the isolated jet and the distinct shielding configurations. In addition, the performance of the CSMC and PFD is compared using the far-field coherence function.

5.3.1 Isolated Subsonic Jet

Sound Pressure Level

Figure 5.17 plots the lossless narrowband SPL spectra for the isolated jet, measured with the fixed microphones only, at various polar angles θ. The spectra are clearly directional with the turbulence mixing noise undergoing strong variations with polar angle, peaking between $\theta = 20°$ to $40°$ and decreasing significantly at the upstream polar stations, as seen in past experimental works [93, 27]. The low frequency noise of the figure is associated with the large-scale turbulence structures, which generate intense and directional acoustic waves that peak in the downstream-most positions, detailed in Chapter 1. Notice how the frequency of the peak of the SPL increases as the polar angle increases, suggesting a transition from the dominance of noise created by large-scale to small-scale turbulence structures [29].

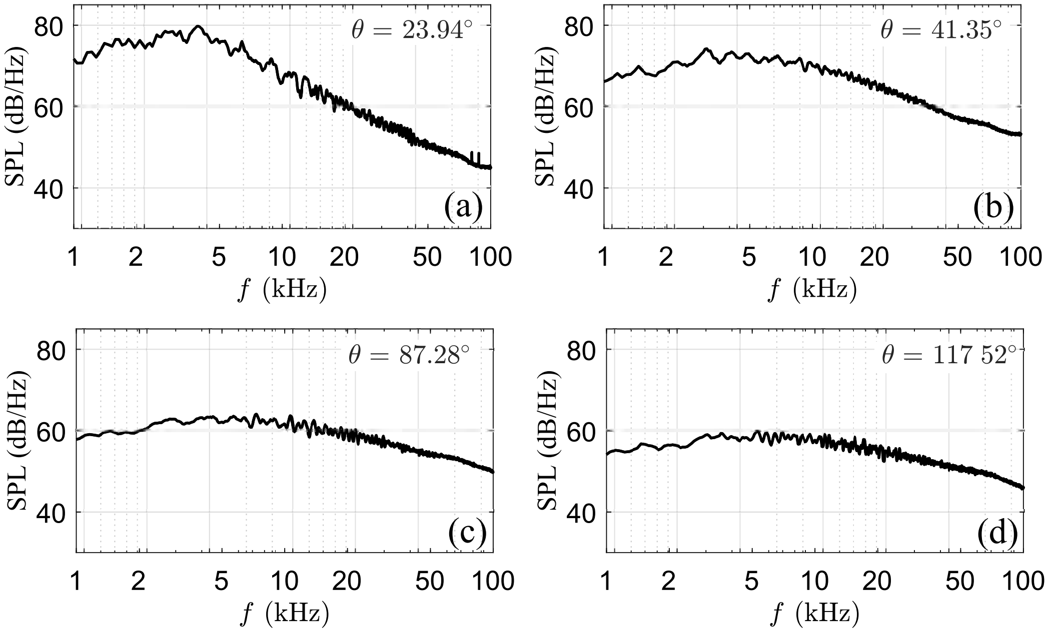

Figure 5.17: SPL spectra for the isolated jet at various polar angles. (a) $\theta = 23.94°$; (b) $\theta = 41.35°$; (c) $\theta = 87.28°$; and (d) $\theta = 117.52°$.

Noise Source Distribution

Figure 5.18 displays noise source maps computed with array layout P of Table 4.2, using the DAS algorithm and the optimized block schedule for the continuous-scan approaches. A dynamic range of 40 dB is used, with the local maximum set to 0 dB. This wide dynamic range is chosen in order to properly visualize the noise source distribution at high frequency. The noise source map computed with FS suffers from strong sidelobes. The source distribution is completely distorted for frequencies higher than 20 kHz and no information about the source can be extracted due to sidelobe contamination. The continuous-scan methods extend the highest frequency that is resolved to close to 90 kHz. The source appears to extend as far as $x = 0.4$ m downstream ($\sim 30D$) at low frequency and gets closer to the nozzle exit plane at high frequency. This behavior has been documented in past experimental works [93, 92] and responds to the physics of noise generation detailed in Chapter 1. Large-scale turbulence structures are correlated over wider spatial regions and are more effective at generating noise, which is demonstrated in the low frequency region of the noise source maps. An opposite behavior is noted for the high-frequency noise, with narrow regions of correlation near the nozzle exit. This behavior will be further explored next.

It is instructive to analyze the peak noise source location to study the potential effects of the shielding plate. This is done in Fig. 5.19, where the peak noise source has been obtained using the three continuous-scan methods. The peak noise location obtained with FS has been obviated in the figure given the lower spatial resolution attained with the approach. The peak low frequency noise producing region is located near $x = 0.12$ m ($\sim 9D$) and the high frequency region is near $x = 0.04$ m ($\sim 3D$). The initial instabilities of the shear layer which are being convected downstream due to the main flow keep growing as they move away from the nozzle exit [94]. These instabilities grow into large-scale turbulence structures that become efficient noise generators at a distance sufficiently far from the nozzle exit. As such, it is expected that low frequency noise is generated further downstream from the nozzle exit. The high-frequency noise producing region is associated with small-scale turbulence structures; with these eddies being already capable of generating noise near the nozzle exit. These short-lived turbulence structures generate uncorrelated broadband noise [95], as demonstrated by the flattening of the SPL seen in Fig. 5.17 at high polar angles [29] and discussed in Chapter 1. The spatial distribution of the small- and large-scale turbulence structures explain the above trends and why it is expected that the shielding surface will be more efficient at preventing high frequency acoustic waves from reaching the microphones, particularly at large polar angles. Additionally, this case is of particular importance since it displays the physics of turbulence mixing noise that were discussed in the first Chapter of this thesis.

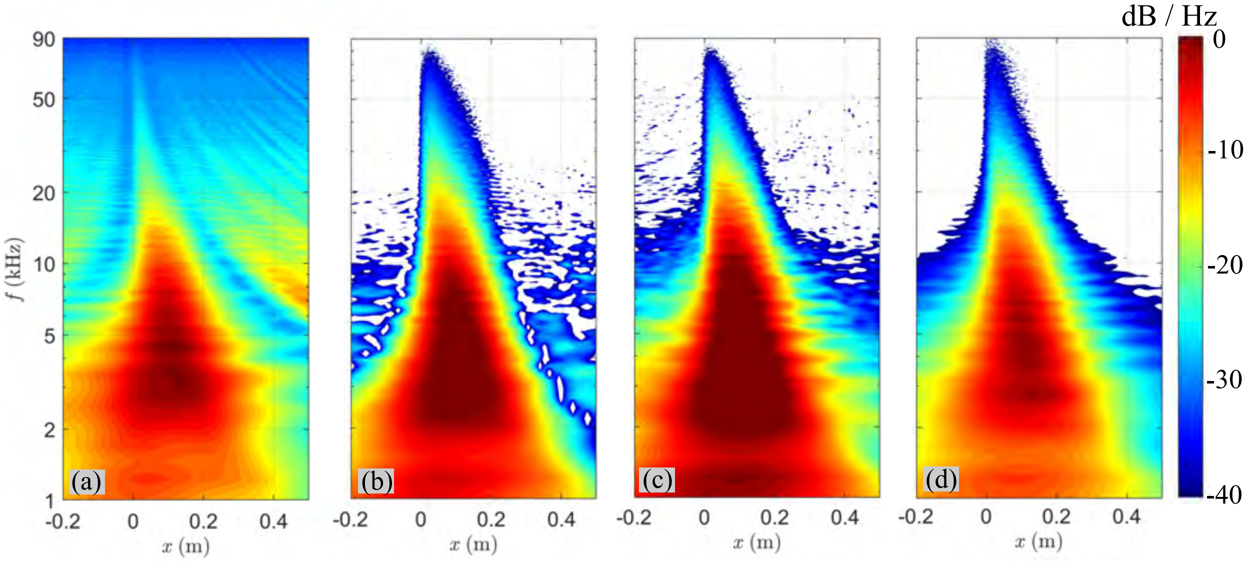

Figure 5.18: DAS noise source maps of the isolated subsonic jet obtained using different methods. (a) FS; (b) CSSM; (c) CSMC; and (d) PFD.

Figure 5.20 shows the deconvolved noise source distribution $\Phi(x, \omega)$ obtained using DAMAS (a), CLEAN-SC (b) and R-L (c) with the PFD technique. It is seen how the noise source map is slightly sharpened when using deconvolution. However, the effects are generally not very significant for this case. The DAMAS and R-L obtain a source distribution that is moderately sharper to that obtained with CLEAN-SC. The trends for the CSMC were

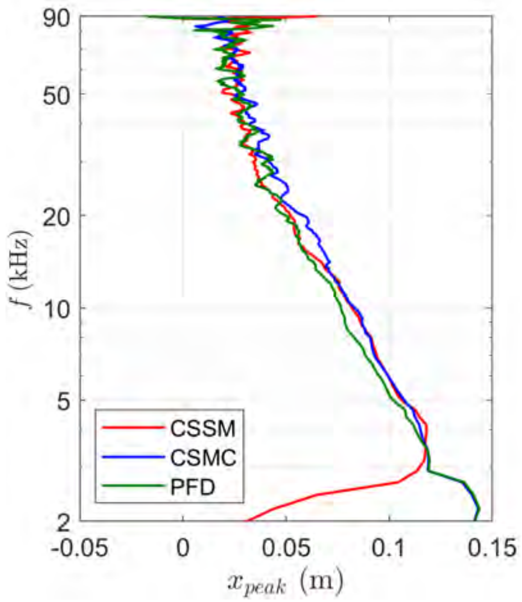

Figure 5.19: Location of the peak noise source for the isolated jet.

similar to those observed for PFD and have not been included in this work for brevity. The deconvolved peak noise source distribution as a function of frequency was similar for DAMAS, CLEAN-SC and R-L using CSMC and PFD, and similar to that shown in Fig. 5.19.

The accuracy of the PFD technique is examined in Fig. 5.21. The image shows the ranked odd singular values (1, 3, 5, etc.) of Eq. 2.66 for the isolated jet. It can be seen how the source appears to be well separated for $f \leq 30$ kHz. However, the difference between the distinct singular values reduces for $f > 30$ kHz and it is expected that the source will not be as precisely represented. This is a direct manifestation of the randomness of the noise generation for $f > 30$ kHz, and hints to the possibility of a high number of uncorrelated sources present for this case. A similar trend was detected in Refs. [79, 21] when using PFD in conjunction with NAH for a subsonic jet. Notice how the trends in Fig. 5.21 can be related to the SPL spectra seen in Fig. 5.17, with the large-scale turbulence structures being prominent noise generators at low frequency and the remaining structures creating

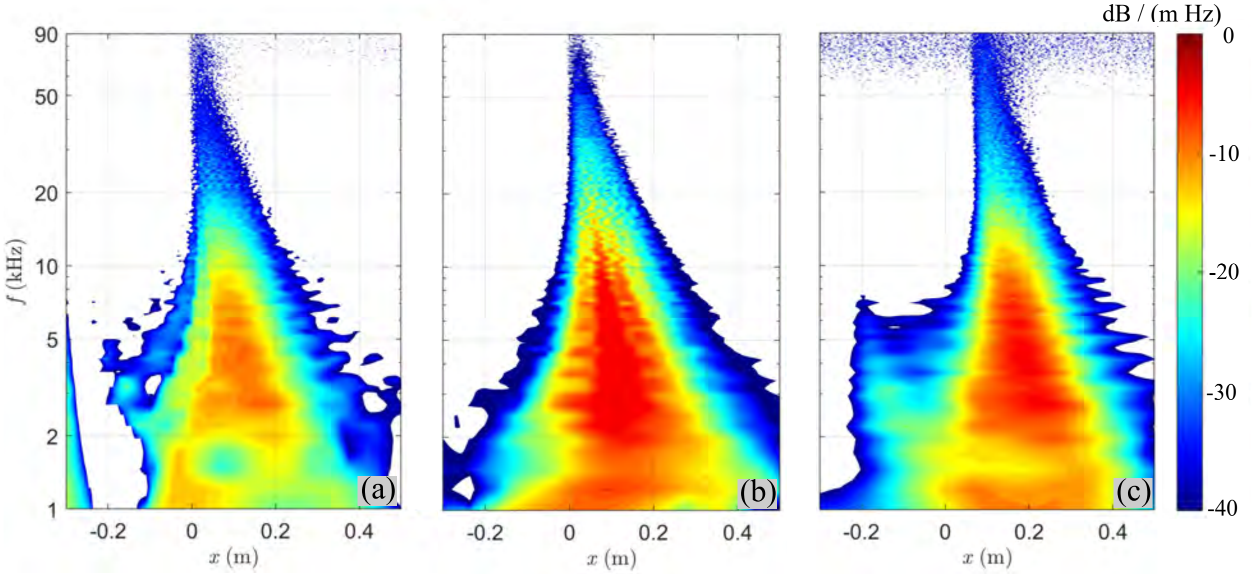

Figure 5.20: Deconvolved noise source maps of the isolated jet obtained with PFD using (a) DAMAS; (b) CLEAN-SC; and (c) R-L.

an approximately broadband acoustic field for $f > 30$ kHz, translating into difficulties in separating the distinct orthogonal sources.

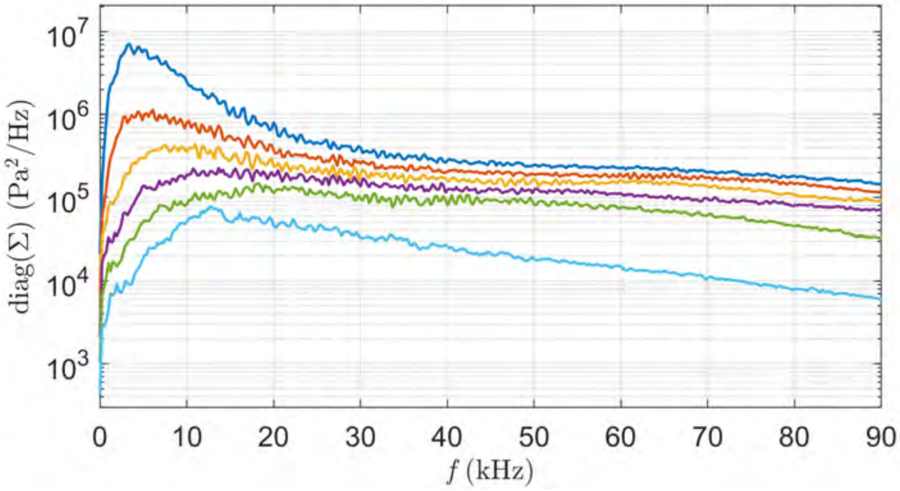

Figure 5.21: Ranked odd singular values (1, 3, 5, etc.) for the isolated subsonic jet.

The performance of the CSMC and PFD techniques can be compared using the far-field complex coherence function. This is done in Fig. 5.39. The real part of the complex coherence of the acoustic far-field for a frequency of 5 and 30 kHz between a fixed microphone, marked with a vertical blue line, and the scanning sensor (i.e., the distinct blocks) is shown in black. The same quantity is displayed in red color for CSMC and the PFD. The corresponding fixed microphone is removed in the computation of the CSMs for the CSMC and PFD technique. The left column uses a microphone near $\theta = 46.4°$ as reference. The right column uses a microphone near $\theta = 80.1°$. The frequency of 5 kHz is representative of the noise generation of the large-scale turbulence structures, as seen in Figs. 5.21 and 5.17 and peaks at shallow polar angles. At 30 kHz the noise emission appears to be produced by uncorrelated sources. The CSMC and PFD technique capture well the far-field complex coherence at 5 kHz, even when the corresponding microphones are removed, underscoring the potential of the continuous-scan techniques. Note the large oscillations of $Re(\gamma)$ present for $40° \leq \theta \leq 60°$. For $\theta > 60°$ the real part of the coherence function decays to almost 0, as broadband uncorrelated noise dominates. The far-field coherence function is not as precisely captured when analyzing a frequency of 30 kHz, linked to an uncorrelated noise generation. As stated earlier, this is due to the possibility of a high number of uncorrelated sources present generating the acoustic far-field at that frequency. Recall that the PFD uses the reference sensors to construct the matrix containing information about the number of sources. As such, if the number of references is low, the spatial resolution obtained in beamforming using PFD will decrease. On the other hand, the CSMC approach is formulated as a weakly sparse eigenvalue problem. This implies that the full CSM is of full rank but contains a small number of dominant eigenvalues. The number of dominant eigenvalues (or singular values) is alike in both CSMC and PFD, thus the results are relatively similar.

5.3.2 Subsonic Jet with Installation Effects

The effects of shielding the subsonic jet flow shown in the preceding section are presented next. The trailing edge of the shielding plate is placed at three different positions with

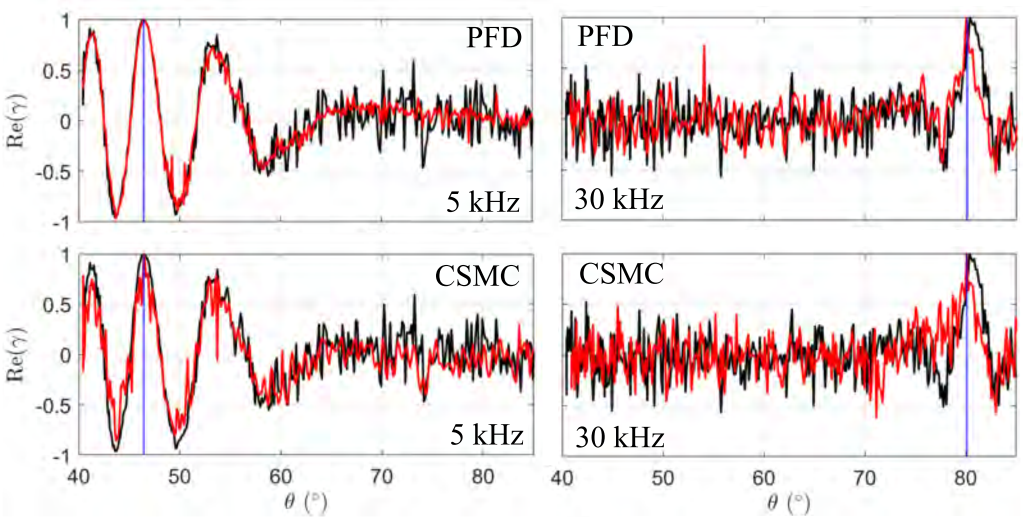

Figure 5.22: Real part of the complex coherence in the acoustic far-field for two frequencies using PFD and CSMC (in red), and using the raw data (in black).

respect to the nozzle exit to study its performance. The vertical offset between the surface and the nozzle axis is kept constant.

Sound Pressure Level

Figure 5.23 plots the SPL spectra of the isolated jet and the jet with the shielding plate at the different positions, measured with the fixed microphones only, for several polar angles θ. The plate in the shielding configuration suppresses sound at high frequency but amplifies the sound at low frequency, as noted in earlier works [91, 96]. If the shielding plate is sufficiently close to the jet flow, the near-field hydrodynamic pressure fluctuations near the trailing edge might be scattered into acoustic waves and create additional noise sources, which manifest at lower frequencies. It can be seen that as the trailing edge of the plate gets closer to the jet flow (Fig. 5.23), the low frequency bumps become more prominent at high polar angles, which is explained by the presence of additional scattering effects. Within the range of the measurements shown, a peak reduction of $\sim$ 12 dB is achieved at θ between 100° and 120° for $L = 8D$, and at a frequency of around 100 kHz. This is a consequence of a source that is more compact at high frequency (see Figs. 5.18 and 5.20), preventing the high frequency acoustic waves from reaching those polar stations.

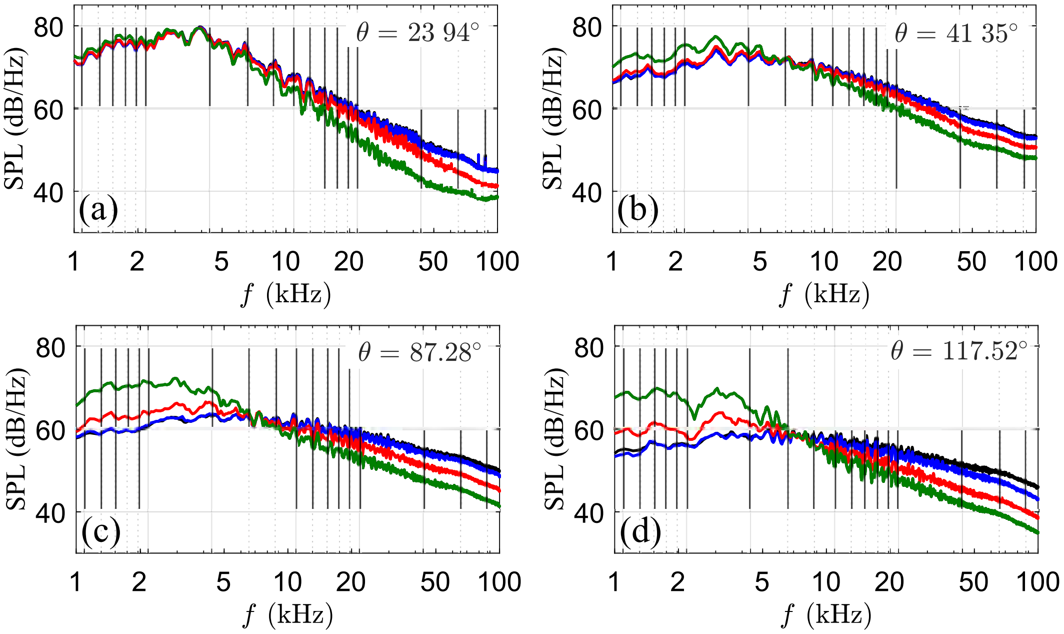

Figure 5.23: SPL spectra for the isolated (black lines) and with the shield at different positions. Blue: $L = 2D$; Red: $L = 5D$; and Green: $L = 8D$. (a) $\theta = 23.94°$; (b) $\theta = 41.35°$; (c) $\theta = 87.28°$; and (d) $\theta = 117.52°$.

Noise Source Distribution

Figure 5.24 displays noise source maps computed with array layout P of Table 4.2, using the DAS algorithm and the optimized block schedule. For the sake of brevity, only the noise source distributions obtained using the PFD technique have been included. In parallel with the isolated jet, a dynamic range of 40 dB is used, with the local maximum set to 0 dB. Image (a) corresponds to the isolated jet while image (b), (c), and (d) correspond to the shielding configuration with $L = 2D$, $5D$, and $8D$, respectively. The position of the trailing edge of the plate is marked with a vertical black line. The effect of the shielding surface is evident from the figure. High frequency noise is significantly suppressed for $L = 5D$ and $8D$. This translates into difficulties in localizing the noise source at that frequency range, as seen in image (c) and (d). Additionally, note how the low frequency noise is exacerbated for the same two cases, manifesting in the noise source map as a significant increase in the strength of the sources from $1 \leq f \leq 5$ kHz. This was seen in the SPL in Fig. 5.23.

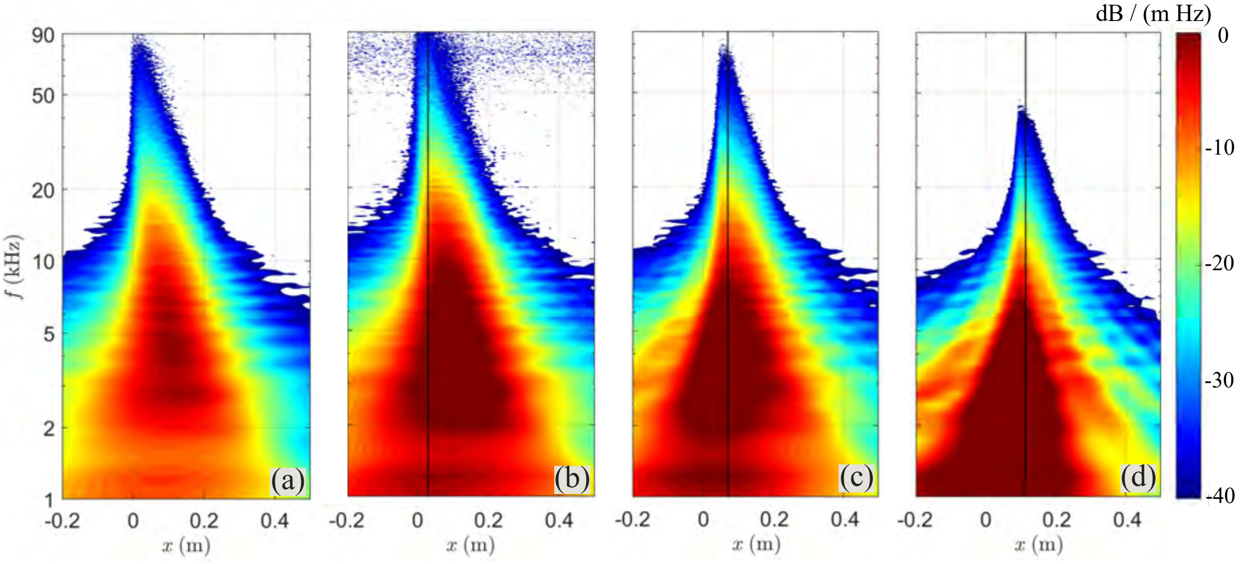

Figure 5.24: DAS noise source maps of the isolated jet and the shielding configuration obtained using PFD. (a) Isolated; (b) $L = 2D$; (c) $L = 5D$; and (d) $L = 8D$.

The effect of the reflector surfaces is further explored in Fig. 5.25. The image shows the location of the peak source for the isolated case and the shielding configurations as a function of frequency. It is seen how the shielding configuration with $L = 2D$ does not significantly change the position of peak noise generation when compared to the isolated case. However, the location of the peak source for $L = 5D$ and $8D$ displaces towards the trailing edge of the plate, which indicate efficient shielding and noise scattering from the edge of the plate at those frequencies.

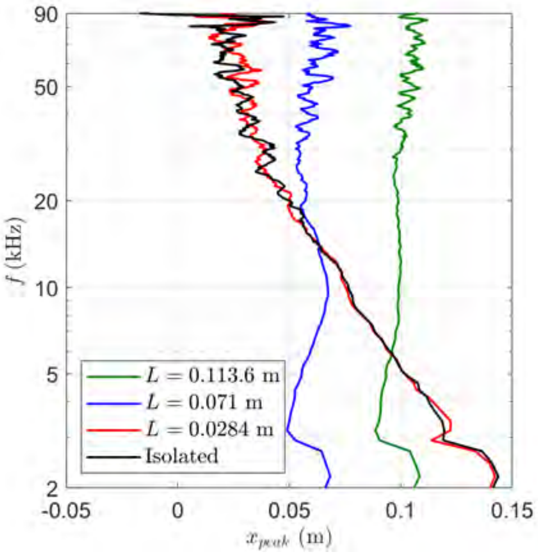

Figure 5.25: Location of the peak noise source for the isolated jet and the shielding configurations.

5.4 Supersonic Jet Flow

This section presents the results obtained for the supersonic jet flow and the reflector configurations featuring the planar and conical surfaces described in Chapter 4. The section shows the SPL of several fixed microphones and a study of the tone directivity performed using the continuously-scanning microphone. High-resolution noise source images are included and used to predict the screech frequency.

The study of screech tones is of vital importance in many aeroacoustic applications. These high amplitude tones are present in a multitude of situations that pose a risk to aircraft systems and human beings. For instance, sustained levels of exposure to high intensity noise that includes screech tones has been associated with hearing losses of military personnel on aircraft carriers. Additionally, these noise components might produce damage to aircraft structures due to sonic fatigue failure in the vicinity of the nozzle exit. A variation of these sustained and high-amplitude pressure oscillations, is found during rocket lift-off operations.

As such, the last decades have seen significant efforts to fully characterize the screech feedback loop, the tone diretivity and the location where these high-amplitude acoustic waves are generated [4]. In addition, researchers have invested significant resources attempting to mitigate tonal noise [97, 98, 28]. This work will present a way to modify tonal noise based on changing the geometry at the nozzle exit by adding conical reflector surfaces.

In the presentation of the results of this section, the notation $\mathrm{X}^{(n)}$ is used to designate a screech tone, where X is the mode and n is the harmonic. The mode notation of Ref. [99] is followed. Modes A1 and A2 denote toroidal oscillation. Modes B and C describe lateral and helical oscillations, respectively. Reference [99] also identified an "unknown" mode E as well as a mode that was not labeled. Inclusion of the 60° reflection surface gives rises to new tones that do not fall into any of the widely-known oscillations modes (A1, A2, B, C).

5.4.1 Isolated Supersonic Jet

Selection of the Pressure Setpoint

The isolated convergent nozzle was initially run at a wide range of total pressures, ranging from 239 to 335 kPa, in order to identify strong screech tones. Typically, the notation of fully-expanded jet Mach number is used over the total pressure ratio. The jet fully-expanded jet Mach number can be related to the ambient and total pressure as

$$\frac{p_0}{p_{amb}} = \left(1 + \frac{\gamma - 1}{2} M_j^2\right)^{\frac{\gamma}{\gamma-1}} \tag{5.2}$$

where p_0 is the total pressure, p_{amb} is the ambient pressure, M_j is the fully-expanded jet Mach number and γ is the heat capacity ratio ($\gamma_{air} \approx 1.4$). The corrected SPL spectra for the isolated nozzle at several fully-expanded jet Mach numbers is shown in Figs. 5.26 to 5.34.

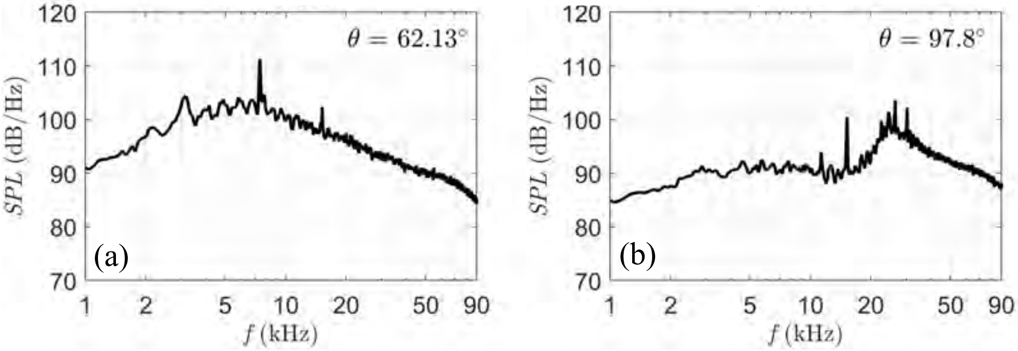

Figure 5.26: SPL spectra for the underexpanded jet at $M_j = 1.18$ various polar angles. (a) $\theta = 62.1°$; and (b) $\theta = 97.8°$.

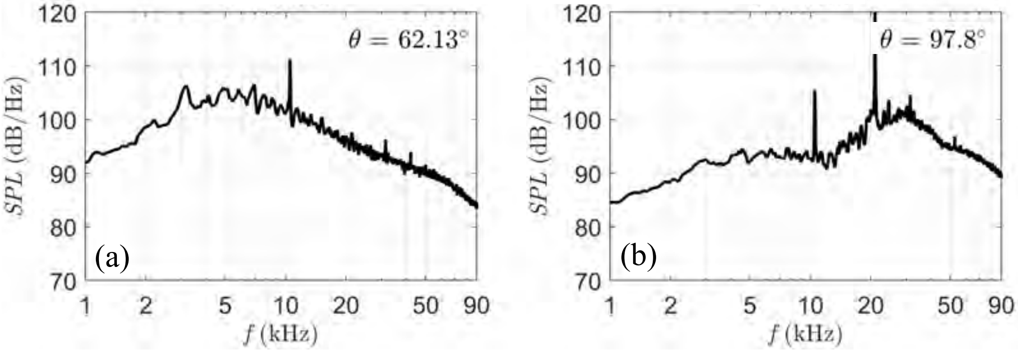

Figure 5.27: SPL spectra for the underexpanded jet at $M_j = 1.22$ various polar angles. (a) $\theta = 62.1°$; and (b) $\theta = 97.8°$.

Note how the intensity of the tones is relatively low at lower-valued fully-expanded jet Mach numbers. As the quantity p_0/p_{amb} increases, the intensity of the tones also increases. It can be seen that operation of the isolated nozzle at $M_j = 1.33$ and $M_j = 1.34$ produced very prominent tones near $\theta = 90°$ and a strong tone near 9 kHz for $\theta = 62.13°$. Operation at $M_j = 1.34$ produces a myriad of harmonics of the fundamental tone at the highest polar station. As such, the total pressure corresponding to $M_j = 1.34$ was selected to perform the subsequent experiments. It is important to mention that the tones for the cases presented

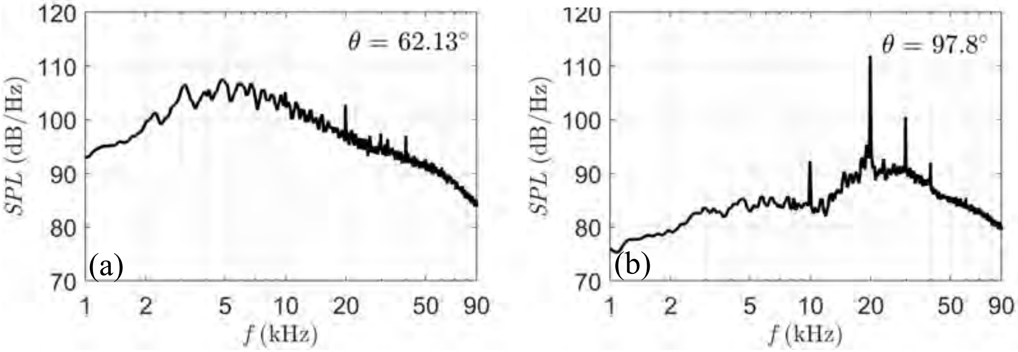

Figure 5.28: SPL spectra for the underexpanded jet at $M_j = 1.26$ various polar angles. (a) $\theta = 62.1°$; and (b) $\theta = 97.8°$.

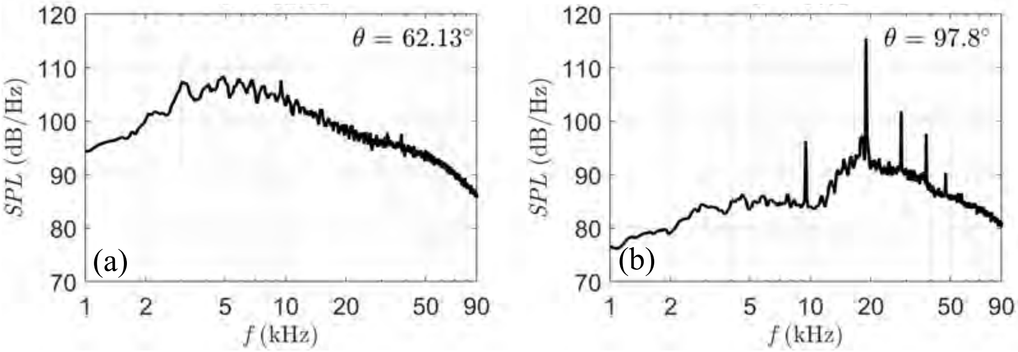

Figure 5.29: SPL spectra for the underexpanded jet at $M_j = 1.30$ various polar angles. (a) $\theta = 62.1°$; and (b) $\theta = 97.8°$.

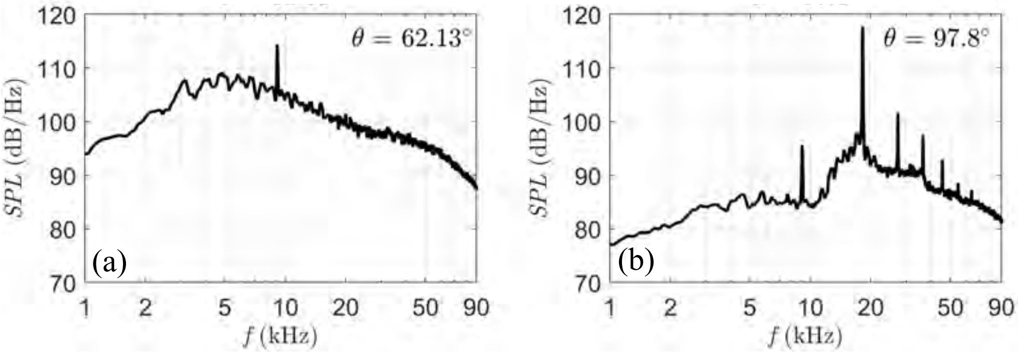

Figure 5.30: SPL spectra for the underexpanded jet at $M_j = 1.33$ various polar angles. (a) $\theta = 62.1°$; and (b) $\theta = 97.8°$.

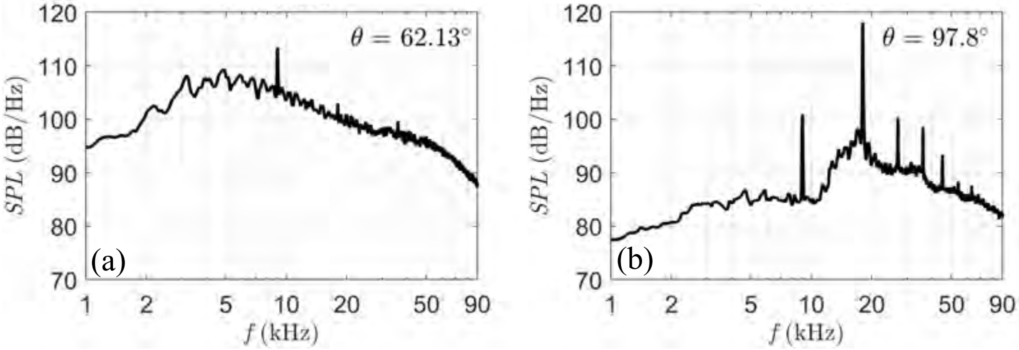

Figure 5.31: SPL spectra for the underexpanded jet at $M_j = 1.34$ various polar angles. (a) $\theta = 62.1°$; and (b) $\theta = 97.8°$.

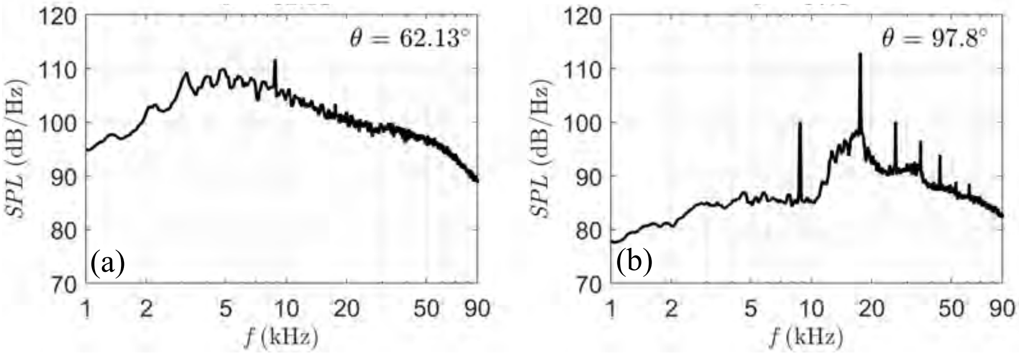

Figure 5.32: SPL spectra for the underexpanded jet at $M_j = 1.36$ various polar angles. (a) $\theta = 62.1°$; and (b) $\theta = 97.8°$.

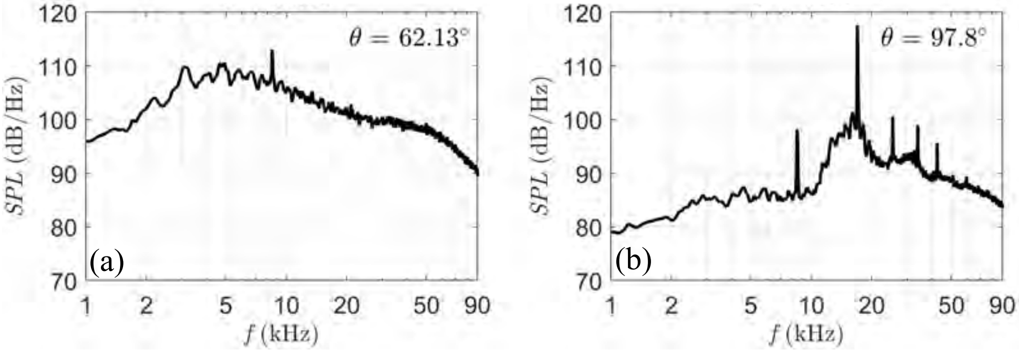

Figure 5.33: SPL spectra for the underexpanded jet at $M_j = 1.40$ various polar angles. (a) $\theta = 62.1°$; and (b) $\theta = 97.8°$.

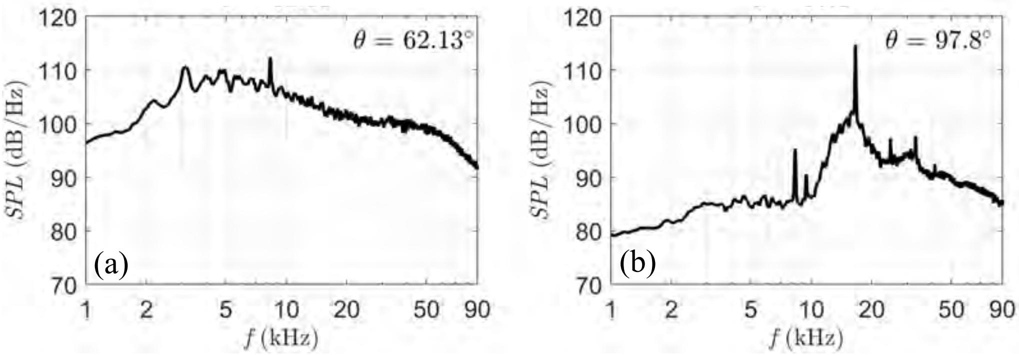

Figure 5.34: SPL spectra for the underexpanded jet at $M_j = 1.43$ various polar angles. (a) $\theta = 62.1°$; and (b) $\theta = 97.8°$.

here were pertaining to jet oscillation mode B, implying the jet flow field was oscillating in a lateral fashion.

Sound Pressure Level

This section presents the SPL spectra for the isolated supersonic jet configuration. This case constitutes the basis for comparison with the supersonic jet flows with the reflector surfaces placed at the nozzle exit. SPL spectra are presented based on the full record of the microphone signals. They are plotted for several polar angles, at which one encounters a richness of tones.

Figure 5.35 displays the lossless SPL spectra for the isolated jet. Tones $B^{(1)}$, $B^{(2)}$, $B^{(3)}$ and $B^{(4)}$ appear very prominently. Their directivity is not uniform, hence their levels vary depending on the polar station [2, 100]. The fundamental frequency of tone $B^{(1)}$ is approximately 9200 Hz. Notice how tone $B^{(1)}$ appears in most of the surveyed stations. Tone $B^{(2)}$ peaks near $\theta = 90°$, overtaking in amplitude tones $B^{(1)}$ and $B^{(3)}$. The tone is more than 20 dB higher than the broadband noise near the peak emission region. The broadband shock-associated noise appears to increase with polar angle, as seen in other works [2, 97]. The screech tone and its harmonics, up to $B^{(4)}$, are marked in the figure.

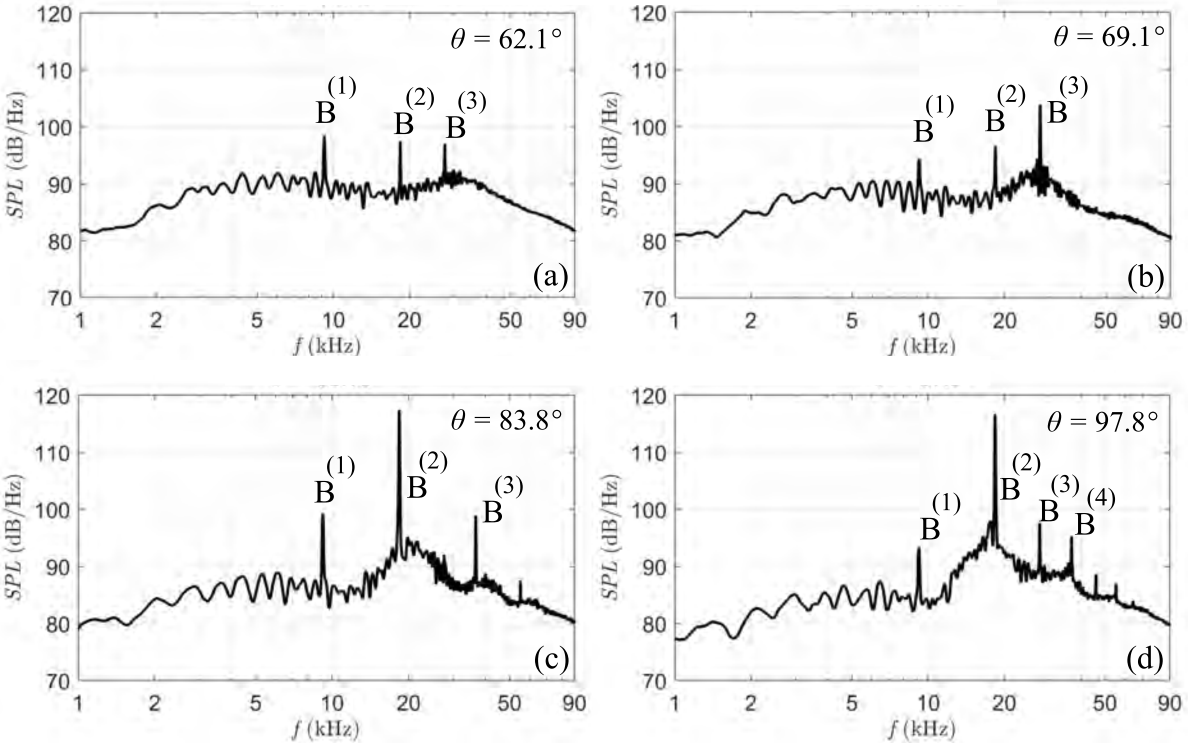

Figure 5.35: SPL spectra for the underexpanded jet at various polar angles. (a) $\theta = 62.1°$; (b) $\theta = 69.1°$; (c) $\theta = 83.8°$; and (d) $\theta = 97.8°$.

Tone Directivity

The directivity of the screech tones was investigated using the continuously-scanning sensor. The "instantaneous" SPL spectra were used to infer the variation of tone levels versus polar angle with high spatial resolution. The signal of the scanning sensor was divided into 299 blocks with 50% overlap. Each block contained 20000 samples, corresponding to a duration of 0.08 seconds. During this time, the sensor traversed 6.1 mm, yielding an angular resolution $\Delta\theta \approx 0.3°$ for the polar sector covered. A Fast Fourier Transform with size 4096 was used to calculate the SPL spectra. This space-time procedure for producing highly resolved SPL(θ) can be affected by the time intermittency of the tones. It is thus expected that the polar directivity may contain spurious variations due to the tone unsteadiness. Results are presented as waterfall plots of SPL versus f and θ. The spectra have been corrected for atmospheric absorption, microphone actuator response and free-field response, and are referenced to a 1-foot arc (0.33 m). Only the frequency range containing tone $B^{(1)}$ and $B^{(2)}$ is shown for clarity.

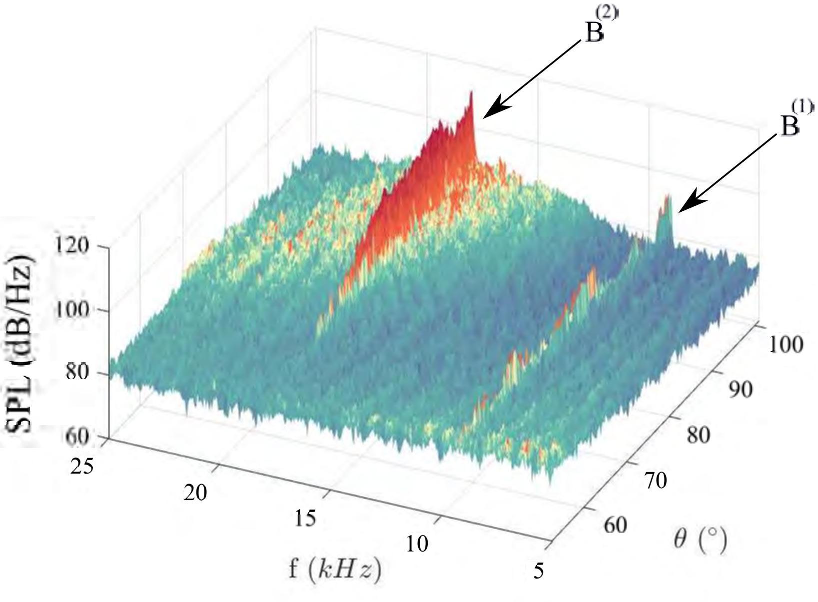

Figure 5.36: Directivity of SPL for the isolated supersonic jet.

Figure 5.36 shows how tone $B^{(2)}$ peaks at the nozzle exit plane and slowly decays as the polar angle decreases until disappearing for $\theta \leq 70°$. Note how tone $B^{(1)}$ appears to be present throughout the scanned region. Its amplitude does not smoothly increase or decrease and appears rather chaotic in the plot. This might be related to the unsteadiness of $B^{(1)}$ [28].

Noise Source Distribution

The beamforming results are obtained using the fixed sensors and the three continuous-scan methodologies, analogous to the previous sections. Beamforming results are shown in Fig. 5.37, and have been obtained using DAS. In the presentation of the noise source maps, a dynamic range of 20 dB is used, with the local maximum set to 0 dB. The noise source map obtained with fixed sensors only lacks of the spatial resolution needed for aeroacoustic applications. The source distribution at high frequency is greatly contaminated by the sidelobes and no useful information can be extracted. This pattern has been seen consistently in this work. The continuous-scan paradigm greatly increases the resolution of the beamformed maps, also demonstrated by earlier works [1, 25, 26, 101]. It is seen how the CSSM, CSMC and PFD techniques produce DAS noise source maps that attain a high spatial resolution and are practically devoid of any sidelobe contamination.

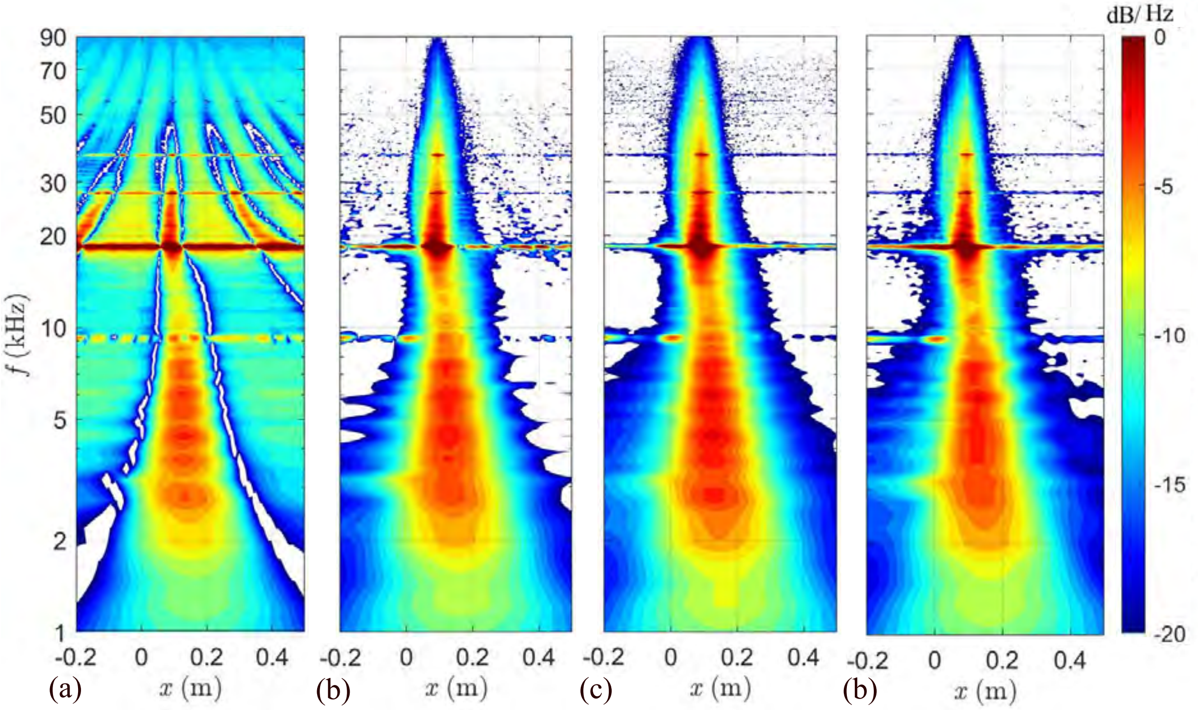

Figure 5.37: DAS noise source maps of the isolated supersonic jet obtained using different methods. (a) FS; (b) CSSM; (c) CSMC; (d) PFD.

The source appears to cover many nozzle diameters (up to $x = 0.3$ m $\approx 20D$) at low frequency, whereas it is closer to the nozzle exit at high frequency. This behavior has been seen in past works [1, 25, 101], and has also been observed for the subsonic jet shown in the preceding section. The jet nozzle exit is located at $x = 0$ m. The horizontal thin layers containing periodic-like patterns represent the location of screech tones $B^{(1)}$, $B^{(2)}$, $B^{(3)}$, and $B^{(4)}$. A weak source at $x = 0$ m is seen near 9 kHz in the continuous-scan maps, indicating the interaction of the upstream-propagating waves of tone $B^{(1)}$ with the nozzle lip that close the feedback loop that is necessary to sustain jet screech. This effect is impossible to discern using the fixed sensors only. At a frequency range of $30 \leq f \leq 50$ kHz, periodic vertical streaks can be seen with the three continuous-scan methods, and will be further studied next. They are discernible to about $x = 0.1$ m $\approx 7D$. These "shock sources" are associated with the turbulence structures that are being convected downstream due to the main flow velocity and their interaction with the shock-cell pattern of the jet. They are approximately aligned with the shock-cells of the jet flow [92, 28]. Similarly to previous sections, it is demonstrated how the continuous-scan approach reduces the need for deconvolution as the DAS maps are already free of ghost sources. However, deconvolution approaches might still be applied to further sharpen the noise source distributions.

The efficiency of the PFD technique at describing the supersonic jet flow is studied next. Figure 5.38 shows the singular values of the diagonal of $\mathbf{\Sigma}_{ff,T}$, calculated using Eq. 2.66, for the jet experiment. The values are plotted against the frequency range of interest. Only the odd-numbered entries of the diagonal are displayed in the figure. It can be seen that there is a relatively good separation between the largest and the smallest singular values for frequencies up to 50 kHz, suggesting that the majority of the energy for such frequency range can be described utilizing a reduced number of independent sources. The opposite behavior is observed for frequencies larger than 50 kHz. The screech tone and its harmonics appear to be well represented using one to three distinct sources. Thus, it is expected that the beamforming results presented in this work will be more accurate for $f \leq 50$ kHz, and start degrading for $f > 50$ kHz. Notice this behavior is in sharp contrast to that found for the isolated subsonic jet (see Fig. 5.21), where there was only good separation between the distinct singular values for frequencies up to 30 kHz.

In line with the preceding section, the performance of the CSMC and PFD decomposition techniques is evaluated in Fig. 5.39 for the supersonic jet case using the far-field complex coherence function. The real part of the complex coherence for tones $B^{(1)}$ and $B^{(2)}$ between a

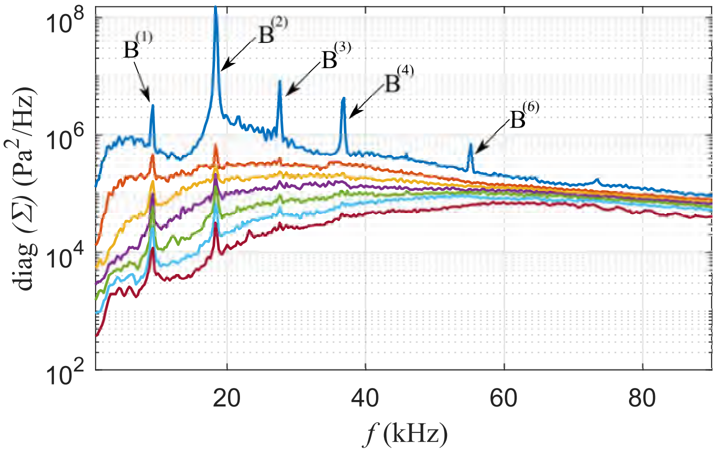

Figure 5.38: Ranked odd-numbered singular values from matrix $\mathbf{\Sigma}_{ff,T}$ for the isolated supersonic jet. Highest to lowest singular value plots are shown from top to bottom.

fixed microphone, marked with vertical blue line, and the scanning sensor is shown in black. The same quantity is displayed in red color for CSMC and the PFD. The corresponding fixed microphone is removed in the CSMC and PFD technique. The left column uses a microphone near $\theta = 90°$ as reference, where the emission for tone $B^{(2)}$ peaks. The right column uses a microphone near $\theta = 65°$, which is found in an area of intense activity of tone $B^{(1)}$ (Fig. 5.35). Both the CSMC and PFD technique capture well the far-field complex coherence, even when microphone the corresponding microphones are removed. The plots appear to be smoother for CSMC than PFD decomposition, but no significant differences between the raw data (the black line) and the two methods are appreciated.

Figure 5.40 presents the results for DAMAS, CLEAN-SC, and R-L deconvolution algorithms of the DAS noise source maps obtained with PFD. The CSMC deconvolution results were of similar quality and will be only used in assessing the shock sources. The source becomes highly localized and the small-scale spatial features of the jet flow are very well-resolved. It is instructive to examine the source distribution around tones $B^{(1)}$, $B^{(2)}$, $B^{(3)}$ and $B^{(4)}$, marked with horizontal lines in the DAMAS map. The source distribution near the $B^{(1)}$ frequency appears to have some periodicity when deconvolved using DAMAS. However, this

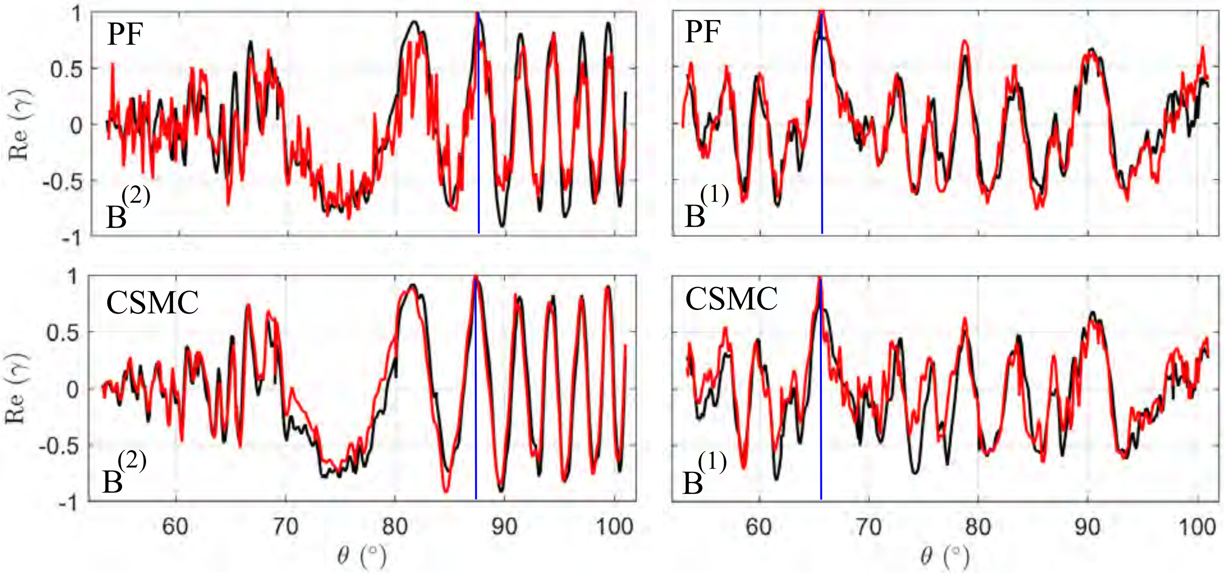

Figure 5.39: Real part of the complex coherence in the acoustic far-field for tones $B^{(1)}$ and $B^{(2)}$ using PF decomposition and CSMC (in red), and using the raw data (in black).

effect is not seen when using the R-L deconvolution or CLEAN-SC. The periodicity might be an artifact of the DAMAS approach which tends to create a speckle-like source distribution. The strong reflection from the nozzle lip near $x = 0$ m, associated with the upstream-propagating waves of tone $B^{(1)}$ is clearly visible. Reflections from the nozzle lip can also be seen for tone $B^{(2)}$. The location of the source peak for tones $B^{(2)}$, $B^{(3)}$ and $B^{(4)}$ is between $0.084 \leq x \leq 0.088$ m, corresponding to $5.9 \leq x/D \leq 6.25$. This apparent location is $1D$ downstream of the location from which the upstream-travelling waves were identified to be originated from for mode B by Powell *et al.* [102], and Mercier *et al.* [103], but is in line with previous experimental beamforming results (Ref. [101]).

The spatial pattern associated with the shock-cell structures near $30 \leq f \leq 50$ kHz is further explored in Fig. 5.41. A dynamic range of 12 dB is used, and the local maximum is set to 0 dB. The image displays a detail of the noise source map obtained with PFD (left column) and CSMC (right column) using the R-L deconvolution (first row), DAMAS (second row) and CLEAN-SC (third row). Moderate averaging in frequency, with a window of ~ 1 kHz,

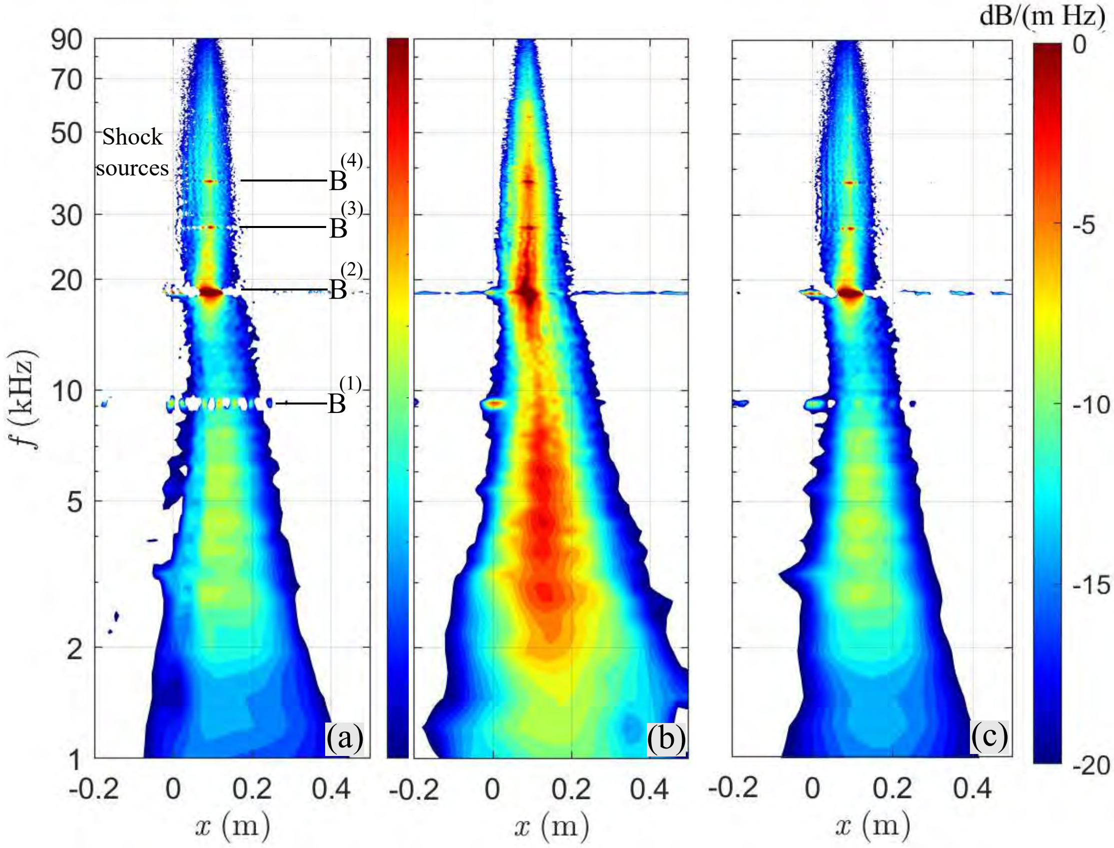

Figure 5.40: Deconvolved noise source maps of the supersonic jet flow obtained with PFD using different algorithms: (a) DAMAS; (b) CLEAN-SC; (c) R-L.

was used in obtaining the contour maps to remove the effects of spurious wiggles in the source distribution. The black dashed vertical lines display the approximate location of the peak source, obtained by finding the local maxima near $35 \leq f \leq 45$ kHz. It is inferred from the figure that the shock cell spacing, which is approximately the same as the spacing of the shock sources, is between $1.17D$ and $1.20D$. This shock cell spacing, obtained only from the beamforming results, is close to that measured by Mercier *et al.* [103] for a jet at a similar fully-expanded Mach number, obtained through Schlieren visualization analysis. In their study, the shock spacing was $s = 1.20D$, approximately. A similar shock spacing is inferred from the *coherence-based* noise source maps of Ref. [101]. This demonstrates the potential of the continuous-scan approach at illuminating the fine details of the supersonic jet flow field. The images deconvolved with CLEAN-SC are not able to perfectly delimit the shock sources due to the low performance of the method at separating closely-spaced sources [82].

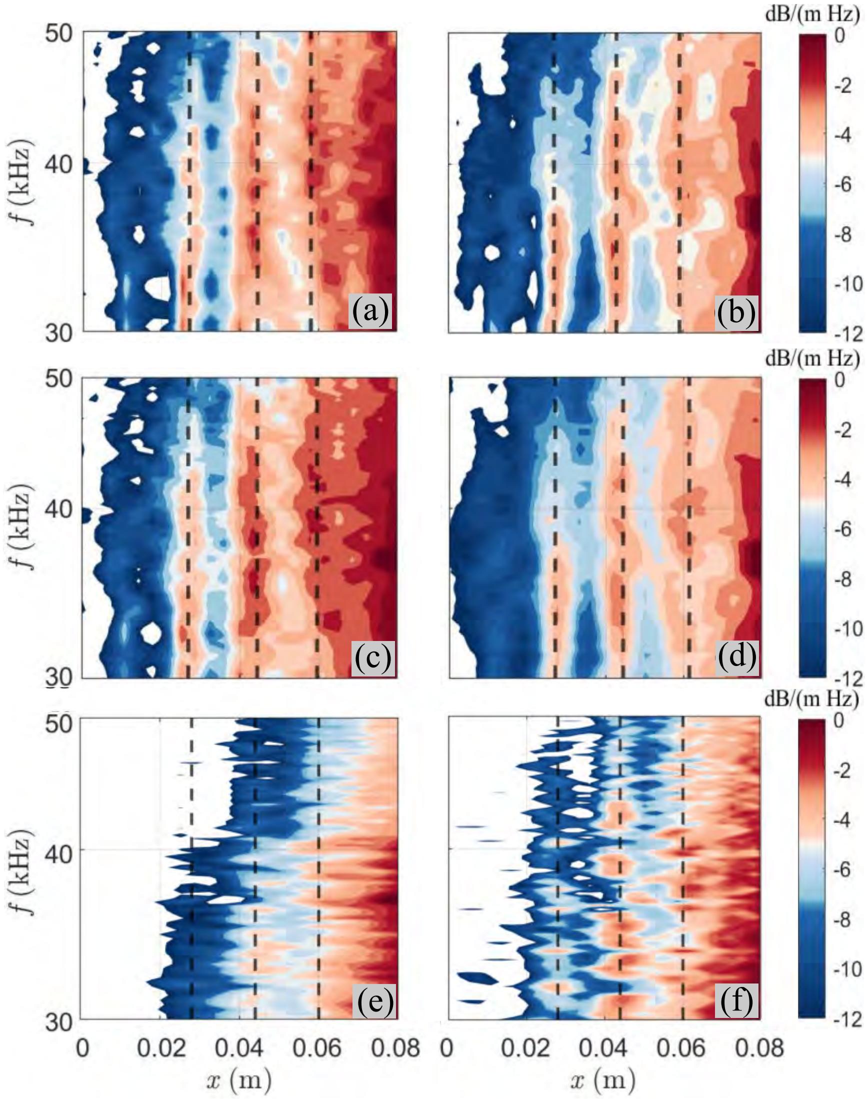

Figure 5.41: Detail of the shock cell pattern around tone $B^{(4)}$ obtained through deconvolution of the PFD (left column) and CSMC (right column) using R-L (first row), DAMAS (second row) and CLEAN-SC (third row).

The information drawn from Fig. 5.41 can be used to predict the screech frequency and determine whether the shock source spacing is physical. In his pioneering work, Powell [39, 38] identified a gain and a phase criteria that must be fulfilled for screech to become self-sustaining. With regards to the gain criterion, he established that the gain associated with all the feedback stages had to be such that amplitude of the new disturbances should at least match that of the previous ones. The phase criterion was formulated in terms of the noise source location x_{ns}, the speed of the downstream- and upstream-propagating disturbances (U_1 and U_2, respectively), the frequency $f_{X^{(n)}}$ at which the shear layer is naturally unstable, and the number of upstream and downstream propagating disturbances N as

$$\frac{N}{f_{X^{(n)}}} = \frac{x_{ns}}{U_1} + \frac{x_{ns}}{U_2} + \psi \tag{5.3}$$

where ψ accounts for any delay associated with the receptivity at the nozzle lip or near the reflection surface, or with the production of the upstream-propagating waves. Powell originally assumed that screech was generated at one or more of the shocks, and incorporated an additional observation related to the screech directivity to predict its frequency. He modeled the screech tone generation by using a series of phased stationary monopole sources located at the shock tips [38, 39, 4]. The screech frequency was predicted based on three monopole sources, connecting the shock spacing and convective Mach number of the downstream-travelling perturbations. By requiring maximum directivity towards the upstream direction ($\theta = 180°$) for the fundamental tone, Powell obtained the well-known relation for the screech frequency

$$f_{X^{(n)}} = \frac{U_c}{s(1 + M_c)} \tag{5.4}$$

where U_c is the convective velocity, s is the shock spacing, and M_c is the convective Mach number, defined as $M_c = U_c/a_\infty$. Although there are different theories explaining how screech is generated [4, 104], Powell's original relationship is still widely used and provides very accurate predictions of the screech frequency in many operation conditions, including for the lateral oscillation mode of the isolated supersonic jet and assuming the upstream-propagating waves move at the speed of sound a_∞. Jet screech has also been studied by performing high-fidelity computational simulations, with recent efforts on round [105, 106] and rectangular supersonic jets [107, 108, 109] aiming at studying the near acoustic field. Gao and Li [110] used their numerical simulations on free round jets to extract a screech frequency prediction formula that was based on the apparent location of the screech source. Their study extracted the integer N of concurrent upstream and downstream disturbances used in Powell's general feedback equation (Eq. 5.3). Based on this, they formulated an equation to predict the screech wavelength

$$\lambda_{X^{(n)}} = \frac{x_{ns}}{N}\frac{1+M_c}{M_c} \tag{5.5}$$

where $\lambda_{X^{(n)}}$ is the screech wavelength and x_{ns} is the effective position of the screech source, that they located at the fifth shock cell. The screech frequency is $f_{X^{(n)}} = a_\infty/\lambda_{X^{(n)}}$. Note that this is similar to Eq. 5.3 with a time delay or phase lag ψ equal to 0 and with a velocity for the upstream-propagating waves equal to the speed of sound. Gao and Li found that the number of concurrent disturbances N was 5 for jets presenting flapping oscillations (mode B), and 6 for supersonic jets oscillating in a helical fashion (mode C).

The screech frequency of tone $B^{(1)}$ is calculated using Eqs. 5.4 and 5.5, using two clearly distinct features of the jet flow extracted from the beamforming results: the spacing of the shock sources and the apparent location of the screech source. Using a convective velocity of $U_c = 0.7U_j$, and a shock spacing of $s \approx 1.18D = 0.0168$ m, obtained from the beamforming results, a screech frequency of $f_s = 9150$ Hz is predicted from Eq. 5.4. A cautionary note with regards to the convective velocity must be made. There have been disparate convective velocities reported for a supersonic jet at approximately the same fully-expanded Mach number of this work. For instance, Panda *et al.* [47] reported $U_c = 0.6U_j$; Castelain *et al.* [111] argue that U_c falls between $0.7U_j$ and $0.8U_j$; and Mercier *et al.* [103] calculate U_c to be between $0.6U_j$ to $0.67U_j$. As such, selecting $U_c = 0.7U_j$ appears reasonable with this regard. The screech frequency using $U_c = 0.6U_j$ is 8400 Hz, while that predicted using $U_c = 0.8U_j$ is

9800 Hz, accruing errors of around 8%.

Finally, using Eq. 5.5 with an approximate screech source location of $x = 6D$, a screech frequency of $f_s = 9000$ Hz is obtained, which deviates less than 2.5% from the measured screech frequency of 9200 Hz. The ability to predict the screech frequency based on far-field measurements alone demonstrates the high degree of spatial resolution that is obtained with the continuous-scan methods.

5.4.2 Supersonic Jet with an Upstream Reflector

The influence of upstream reflector surfaces on jet screech is studied next. It is widely accepted that the phenomenon of jet resonance is highly dependent on the boundary conditions of the experiment (lip thickness, screech reflection point, etc.). For instance, changes in the lip thickness are associated with a reduction of the screech frequency for mode B, and also associated with higher tone amplitudes when using nozzles with larger lip thicknesses. The modification of the nozzle lip produces changes in the receptivity process, and can even reactivate the screech feedback loop after its cessation [97]. It has also been reported that the jet might be oscillating in a lateral (mode B) or helical fashion (mode C) depending on the nozzle lip thickness at a given fully-expanded jet Mach number (see Fig. 1.4), and the tones might show a degree of intermittency depending on the laboratory facility [4]. The presence of upstream reflectors exacerbate this trend and might introduce new non-linearities, energizing the jet oscillation at lower nozzle total pressures. This highly nonlinear behavior is also manifested in the underexpanded jet experiments presented in this work. Here, a 90° reflector plate and a 60° conical reflection surface are used to modify the screech feedback loop and infer any changes in the spatial structure of the jet flow using the continuous-scan microphone array. It will be demonstrated how the presence of these two surfaces changes the emission dynamics, with new tones arising.

Sound Pressure Level

Figure 5.42 displays the lossless SPL spectra for the isolated jet (black) and the jet with the 90° reflector (red). Tones $B^{(1)}$, $B^{(2)}$, $B^{(3)}$ and $B^{(4)}$ are marked in the figure. It is seen how addition of the planar reflector surface turns into an enhanced tonal emission, with harmonics $B^{(1)}$ through $B^{(8)}$ arising. The frequencies of the tones are lower than those of the isolated jet, indicating an increase in the shock-cell spacing that increases the screech wavelength (thus reducing the frequency) [4]. The jet appears to be locked into oscillation mode B for both cases. Note that the broadband shock-associated noise source level is higher for the cases with the reflector, becoming especially evident at $\theta = 62.1°$ and $\theta = 69.1°$. The directivity of the tones is highly non uniform, with the highest harmonics only appearing at high polar angles. The intensity of tones $B^{(1)}$, $B^{(2)}$, and $B^{(3)}$ also undergoes significant variation with polar angle. The lower screech frequencies for mode B that appear with the 90° reflector have been associated in the past with a slight increase in the shock-cell spacing of the jet, increasing the screech wavelength. Thus, in order to meet the requirements of Eq. 5.3 with a larger shock spacing, the screech frequency must decrease.

Figure 5.43 displays the lossless SPL spectra for the isolated jet (black) and the jet with the 60° reflector (red). Tones $B^{(1)}$, $B^{(2)}$, $B^{(3)}$ and $B^{(4)}$, $E^{(1)}$ and $E^{(2)}$ are marked in the figure. The new tones that arise for this case are marked in red. Similar as in the previous case, the directivity of the tones is highly dependent on polar angle. It is seen how the addition of the 60° reflector changes the emission dynamics of the jet, with tones $E^{(1)}$ and $E^{(2)}$ appearing prominently. Tone $E^{(1)}$ dominates most of the surveyed region and its amplitude does not suffer strong oscillations with observation angle. Tone $E^{(1)}$ dominates most of the surveyed region. Tones $B^{(1)}$, $B^{(2)}$, $B^{(3)}$ and $B^{(4)}$ also appear for the 60° reflector case, but they are much weaker compared to their amplitudes for the isolated jet or the 90° reflector. It thus appears how there is an energy transfer from the unstable frequency of mode B to that of mode E. Notice how the tonal noise is reduced at the most upstream stations but is enhanced

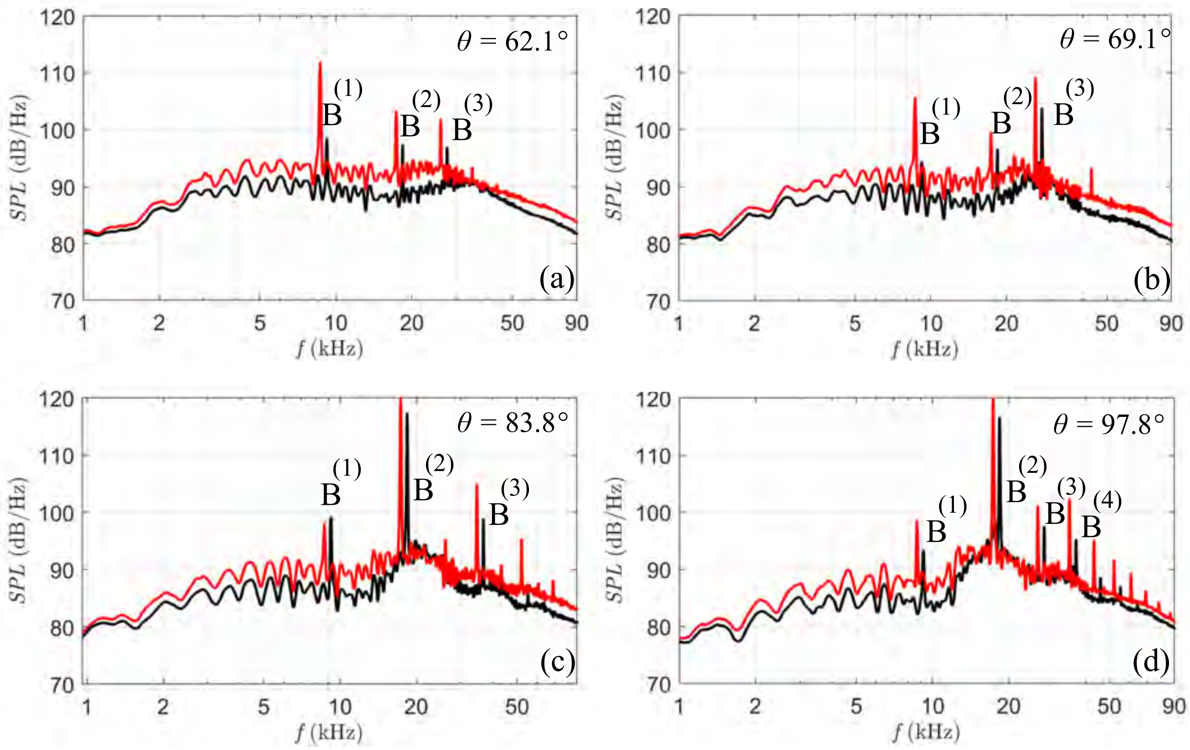

Figure 5.42: SPL spectra for the underexpanded jet with the 90° reflector at various polar angles. (a) $\theta = 62.1°$; (b) $\theta = 69.1°$; (c) $\theta = 83.8°$; and (d) $\theta = 97.8°$.

at shallow polar angles. It is important to remark that tone $E^{(1)}$ or $E^{(2)}$ do not fall into any of the widely-known jet oscillation mode categories (A1, A2, B, or C) and the jet oscillation dynamics for this mode are unknown. It could be an extension of a toroidal mode or a new unstable frequency of mode B which is reactivated due to the introduction of the reflector. In addition, an interaction tone which is the product of mode B and E appears at high polar angles, situated between the frequency of $B^{(2)}$ and $E^{(2)}$.

Tone Directivity

The directivity of the screech tones is investigated using the continuously-scanning sensor using the “instantaneous SPL spectra”, in parallel to the analysis performed for the isolated jet. The block size, number of blocks and polar angle resolution is kept the same. The

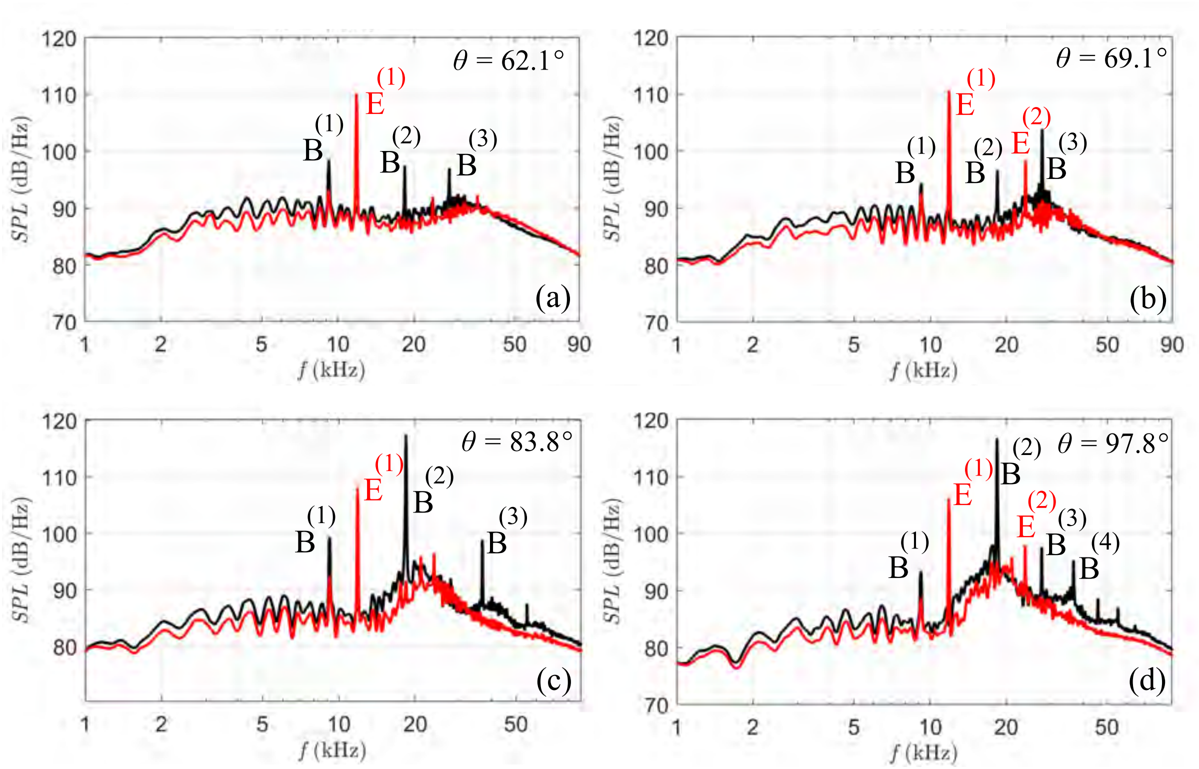

Figure 5.43: SPL spectra for the underexpanded jet with the 60° reflector at various polar angles. (a) $\theta = 62.1°$; (b) $\theta = 69.1°$; (c) $\theta = 83.8°$; and (d) $\theta = 97.8°$.

spectra have been corrected for atmospheric absorption, microphone actuator response and free-field response, and are referenced to a 1-foot arc (0.33 m).

Figure 5.44 has been obtained for the jet with the 90° reflector. It shows how the directivity patterns of tones $B^{(2)}$ and $B^{(1)}$ are relatively similar to those observed for the isolated supersonic jet. Tone $B^{(2)}$ peaks near $\theta = 90°$ and slowly decays as the polar angle decreases. Tone $B^{(1)}$ manifests more prominently throughout the scanned region, particularly at shallow polar angles.

Figure 5.45 is calculated for the jet with the 60° reflector and shows the directivity of tones $E^{(1)}$, $E^{(2)}$, $B^{(1)}$, $B^{(2)}$ and $F^{(1)}$. Tone $F^{(1)}$ appeared to be the complex interaction of tones $E^{(1)}$ and $B^{(1)}$ as mentioned previously, with its frequency following $f_{F^{(1)}} \approx f_{E^{(1)}} + f_{B^{(1)}}$. Notice how tone $E^{(1)}$ appears prominently throughout the scanned region and tones $B^{(1)}$

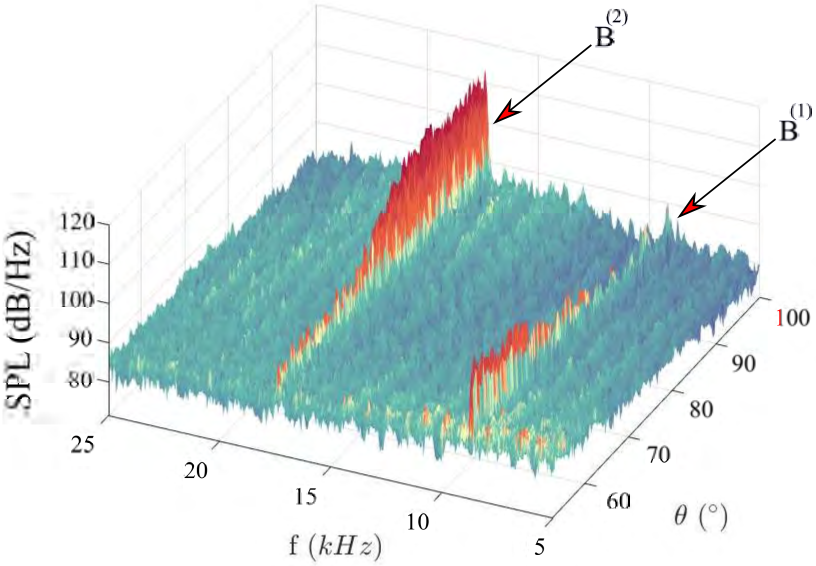

Figure 5.44: Directivity of SPL for the supersonic jet with the 90° reflector.

and $B^{(2)}$ appear relatively suppressed. Tone $F^{(1)}$ only appears at high polar angles while tone $E^{(2)}$ is present from 70° to 100°. The amplitude of tone $E^{(1)}$ appears rather chaotic, which might be a product of tone unsteadiness.

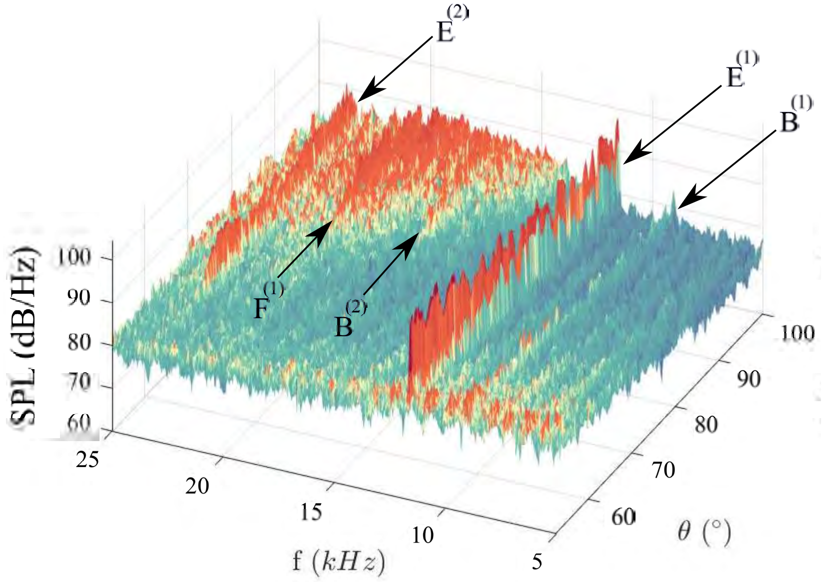

Figure 5.45: Directivity of SPL for the supersonic jet with the 60° reflector.

Noise Source Distribution

The noise source maps for the jet with the 90° reflector were similar to those obtained for the isolated jet and have not been included in this work for brevity. The only differences were the tonal noise and broadband shock-associated noise appeared more intense in the spatio-spectral plots, and the shock-cell spacing was slightly higher ($s \approx 1.19D$).

Figure 5.46 shows the deconvolved noisse source maps for the jet with the 60° reflector obtained with DAMAS (a), CLEAN-SC (b), and R-L (c) using PFD. The overall trends are similar to those of the isolated supersonic jet, with the sources extending further downstream at low frequency and becoming more compact at high frequency. However, some significant differences on the source distributions associated with the screech tones are noted. Similarly as in the previous case, the nozzle exit is located at $x = 0$ m. Screech tones $B^{(1)}$, $B^{(2)}$, $E^{(1)}$, $E^{(2)}$ and $F^{(1)}$, marked in the DAMAS contour plot, can be clearly seen in all the noise source distributions, corresponding to the thin horizontal layers presenting periodic-like patterns for the frequencies between 9 and 25 kHz. Strong reflection sources for tones $B^{(1)}$ and $E^{(1)}$ are seen for x between -0.0216 and -0.018 m, corresponding to $-1.52 \leq x/D \leq -1.25$. This corresponds approximately to the axial position of the edges of the reflector, which are strong scattering noise sources. This clearly indicates the presence of upstream-propagating types of waves for mode E, implying there is a feedback loop process associated with the frequency of tone $E^{(1)}$ that must be present in order to sustain the high amplitude tonal emission. The figure clearly indicates that installation of the 60° surface changes the point from which the upstream propagating waves reflect back to the flow and scatter, producing changes in the feedback loop length and introducing new unstable frequencies (mode E). In addition, it appears that additional upstream-propagating components appear near the frequency range of 12 to 16 kHz when using the reflector surface, a behavior also seen in Ref. [101], and not seen for the isolated supersonic jet.

A certain degree of source periodicity is noted near tones $B^{(1)}$ and $E^{(1)}$. However, the periodicity might be an artifact of the deconvolution process, for which DAMAS is especially prone to. Finally, note how the CLEAN-SC deconvolution results in a noise source that does not appear to be as sharly localized as that obtained with DAMAS and R-L. This is especially clear near the screech frequencies at the nozzle exit, where the reflections and scattering from the reflector surfaces appears to extend significantly compared to the other methods.

The apparent location from which the upstream-traveling waves emanate is not easy to discern and appears to be different for each mode. Tone $E^{(2)}$ is generated near $x = 0.1049$ m $\approx 7.4D$, and tone $F^{(1)}$ near $x = 0.1012$ m $\approx 7.1D$. It is difficult to extract the location of tone $B^{(1)}$ or $B^{(2)}$ from the noise source maps. This is in contrast with the source distribution for the isolated jet (Fig. 5.40), where the location of the apparent screech source was clearly seen for tones $B^{(2)}$, $B^{(3)}$ and $B^{(4)}$, and a direct manifestation of substantial changes in the jet flow field produced by the upstream reflector. The intensity of tones $B^{(2)}$, $B^{(3)}$, and $B^{(4)}$ is much lower for the reflector case (Fig 5.43), which is also reflected in the noise source distribution by making the assessment of the generation of these tones cumbersome.

In parallel to the previous analysis, the spatial pattern of the shock-cell structures near $30 \leq f \leq 50$ kHz is explored in Fig. 5.47. The figure has been obtained in an analogous manner as Fig. 5.41. The shock sources appear to be spaced an average distance between $s = 1.16D$ to $1.19D$, which is in line with the isolated jet. The shock spacing was expected to be similar given that it is only a function of the fully-expanded jet Mach number (or the nozzle pressure ratio). Powell's formula for the screech frequency (Eq. 5.4) can be used to predict a screech frequency of tone $B^{(1)}$ near 9100 Hz, similar to the measured frequency, using $U_c = 0.7U_j$. The cautionary note with regard to the convective velocity that was stated for the isolated jet is again reminded for this case.

The frequency of tone $E^{(1)}$ cannot be predicted using the same equation. In addition, it is difficult to use Eq. 5.5 to predict the screech frequency of tone $B^{(1)}$ due to the inability to

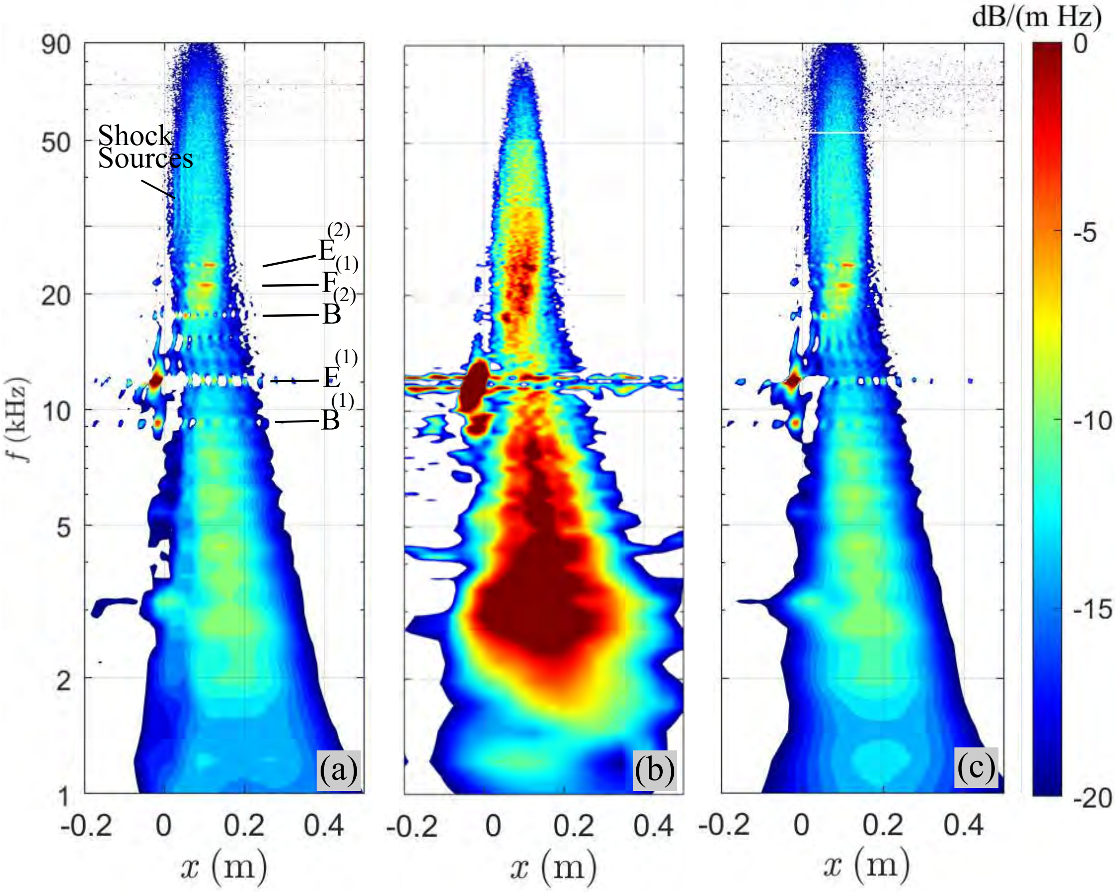

Figure 5.46: Deconvolved noise source maps of the supersonic jet flow with the 60° reflector obtained with PFD using different algorithms: (a) DAMAS; (b) CLEAN-SC; and (c) R-L.

extract the approximate position of the screech source from the beamformed maps. This issue also manifests in the coherence-based noise source maps of Ref. [101]. Regarding tone $E^{(1)}$, Gao and Li's formula does not correctly predict its frequency if one uses that the number of concurrent upstream and downstream disturbances in the jet flow is 5 (i.e. $N = 5$), which is what is found for mode B. However, the predicted screech frequency is remarkably close to the measured value (within 1%) if one uses $N = 8$. This might be the case for mode E or might just be a coincidence. Nevertheless, it is reasonable to believe that high screech frequencies are associated with a higher number of concurrent upstream- and downstream-propagating disturbances. For instance, it has been found [110] that jets oscillating in a helical mode are associated with $N = 6$. Thus, given that it is true that $f_{E^{(1)}} > f_{C^{(1)}}$, it is expected that $N_{E^{(1)}} > N_{C^{(1)}}$.

The fact that mode B and mode E have different numbers of concurrent upstream- and downstream-propagating waves might also hint at different mechanisms of screech generation. The presence of the upstream reflector appears to produce changes to the jet flow, and the screech modes appear to be very sensitive to such differences. It is possible that two mechanisms are at work, exciting the shear layer near $f_{B^{(1)}}$ and $f_{E^{(1)}}$ at the same time, even if the jet is oscillating in a lateral fashion. Shen and Tam [50] suggested that neutral acoustic modes of the jet might also play an important role in the screech process. Similar observation were made by Singh and Chaterjee [112] with regards to oscillation modes A1 and A2. Whether mode E is supported by these neutral acoustic modes cannot be determined from this results alone and was outside of the scope of the current work.

This section demonstrates the true potential of the continuous-scan paradigm at resolving the very fine details of the jet flow field. Empirical and theoretical formulas have been used to predict the screech frequencies of the supersonic jet, based on distinct features of the jet flow field. The three continuous-scan methods (CSSM, CSMC, PFD) show a remarkable higher level of spatial resolution when compared to the same array using fixed sensors only.

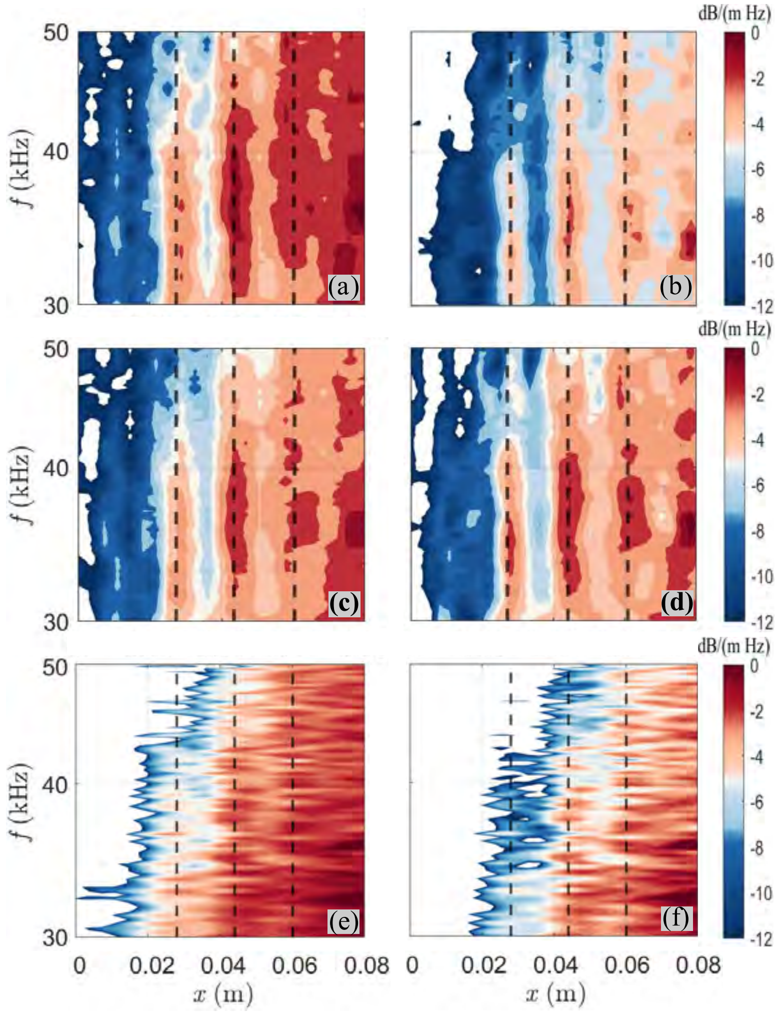

Figure 5.47: Detail of the shock cell pattern around tone $B^{(4)}$ for the 60° reflector case obtained through deconvolution of the PFD (left column) and CSMC (right column) using R-L (first row), DAMAS (second row) and CLEAN-SC (third row).

Chapter 6

Conclusions and Future Considerations

6.1 Conclusions

The purpose of this work was to improve the state-of-the-art of the current beamforming techniques that are widely used in noise source localization studies. Even though these methodologies are used in a myriad of industries, an special emphasis is made within the context of noise generated by propulsion-related devices. The improvement of the current beamforming techniques required working with novel experimental setups that comprised fixed and continuously-scanning sensors. This is in contrast with traditional techniques, where only fixed sensors are utilized. The introduction of a continuously-scanning sensor required special spectral estimation techniques [1] and division of the signal into quasi-stationary blocks to suppress the non-stationarity in the correlations of sensors that had a relative velocity. The Wigner-Ville Spectral estimator was used to quantify the non-stationarity and find ways to suppress it.

The signal segmentation process is key to fully exploit the benefits of the continuous-scan paradigm and might introduce variability in the noise source localization process if it is not done systematically. Chapter 3 analyzed the signal processing in terms of geometric effects, spatial resolution, spectral accuracy, and adequacy of samples within each block. Criteria for optimal block size, number of blocks, and block overlap within distinct frequency ranges was formulated. Implementation of the method entailed discrete reductions in block size and FFT size with increasing frequency. The end result consisted in patching the noise source maps obtained with the variable-sized blocks. The role of the signal processing was analyzed using the point spread function in Chapter 5. It was demonstrated how the proposed block schedules suppressed the sidelobes to a great extent when compared to other, non-optimal block configurations, and incurred into a high-resolution noise source localization process.

This work has presented three distinct methodologies to construct the noise source maps utilizing phased arrays that contain continuously-scanning sensors. The first is a natural extension of the traditional delay-and-sum algorithm and uses information of the distinct cross-spectral submatrices (CSSM). The noise source map is obtained by combining the non-repeated elements of the CSSMs for each block. This resulted in highly suppressed sidelobes and an increased spatial resolution when compared to an array that utilized fixed sensors only. A main drawback of the approach, however, is the lack of a global CSM that is representative of the complete experimental run. This means that advanced beamforming processes such as orthogonal or functional beamforming and deconvolution are impossible. Two additional approaches were introduced to obtain a global CSM. The first consisted of a cross-spectral matrix completion (CSMC) and partial fields decomposition (PFD) method was the second. The first technique was originally proposed as a tool to extend the array resolution from non-synchronous microphone measurements or replace faulty microphones, and has been applied to synthetic and industrial noise sources in the past. This thesis extended the method to the continuous-scan paradigm. The second method, PFD, has been used in the past in near-field acoustic holography studies and beamforming and has been described in this work within the continuous-scan context. The CSMC and PFD yield noise source maps with very high spatial resolution, and suppress the sidelobes to a greater extent when compared to the CSSM approach.

The Partial Fields Decomposition technique can be used to develop low order models. The technique decomposes the acoustic field into a number $\mathcal{M}_f$ of coherent and orthogonal partial fields, where $\mathcal{M}_f$ is the number of fixed microphones. The leading partial fields can be studied by displaying the singular values of the reference CSM. As such, this allows for the possibility of describing complex acoustic fields utilizing a reduced number of partial fields depending on the difference in the order of magnitude of the singular values. This technique can be employed in the acoustic near-field, at a distance that is sufficiently close to the acoustic source, in order to find the leading partial fields which can later be used in conjunction with Boundary Element Methods (BEM) to propagate the radiation in the far-field. This allows the detailed study of scattering and shielding effects for aeroacoustically-relevant noise sources and enable further research in rapid noise assessment.

This thesis presented and briefly described three widely-used deconvolution approaches: DAMAS, CLEAN-SC, and Richardson-Lucy (R-L). The details and assumptions of each of the methods have been outlined, and their performance has been assessed on distinct sources. They have been used in conjunction with the CSMC and PFD techniques and improved the spatial resolution of the noise source maps a step further.

All the methodologies have been successfully applied to the imaging of an impinging jets source. The impinging jets source is an approximation to a point source and provides an ideal experimental background to disseminate the potential of the continuous-scan approach. It has been demonstrated how imaging of the source with an array that contained fixed sensors only resulted in a poor spatial resolution, with the noise source map being completely dominated by the sidelobes. Addition of the continuously-scanning sensor improved the spatial resolution significantly. The three continuous-scan approaches of this work resulted in a highly localized source. The localization of the noise source was improved using deconvolution in conjunction with CSMC and PFD. It was demonstrated the superior ability of the R-L over DAMAS and CLEAN-SC at obtaining a high-fidelity noise source maps. DAMAS created a speckle-like source distribution while CLEAN-SC obtained a wider source.

A subsonic jet source in different shielding configurations was also analyzed. The continuous-scan technique was used to discern the spatio-spectral distribution of the subsonic jet flow. The location of the peak noise source as a function of frequency was discussed and the potential effects of shielding were argued. Three shielding cases were presented, with the jet flow not scrubbing on the plate for any of them. It was found that when the plate is sufficiently close to the edge of the jet, additional noise is scattered from the trailing edge. This is attributed to an energy conversion from near-field hydrodynamic disturbances into acoustic wave scattering. The plate proved to be an efficient means of blocking high-frequency noise at the highest polar stations. Its efficiency was more limited at the lower polar stations, with a raise in the low frequency noise.

This work culminated with the analysis of a supersonic jet flow with several reflector configurations. Again, the distinct continuous-scan approaches were used to obtain high-fidelity noise source distributions. It was experimentally found that operation of the jet in isolation gave rise to strong screech tones pertaining to jet oscillation mode B (lateral oscillation). Deconvolution used in conjunction with CSMC and PFD allowed resolution of the very fine features of the jet flow field that have been discerned in past research works using optical techniques or near-field experiments. This is a clear testament of the high degree of spatial resolution that can be attained with the methods presented in this work. The location of the screech source was used to predict the screech frequency with high accuracy. The shock-cell spacing, obtained from beamforming, was also used to predict a similar screech frequency. Reflector plates at the nozzle exit were used to illuminate the high-degree of non-linearity of resonant supersonic flows. To that end, a 90° and a 60° degree reflectors were placed at the nozzle exit. It was found that addition of the 90° reflector reinforced tonal noise, with more harmonics appearing and with the intensity of the tones becoming more prominent. However, this did not produce a shift in the jet oscillation dynamics. Addition of the 60° gave rise to new tonal components that we categorized as mode E, coexisting with the tones of mode B. Note that the frequency of these new tones does not appear to match any of the known modes (A1, A2, B, C). It was demonstrated how the directivity of mode E was completely different to that of mode B. Additionally, the 60° was capable of mitigating broad-band shock associated noise and tonal noise at high polar angles, which might be beneficial in terms of avoiding sonic fatigue failure of aircraft surfaces. The continuous-scan approach was also used to find the location of the screech sources and to visualize the shock-cell pattern. The latter was found to be similar to that of the isolated jet, enabling to predict a screech frequency close to that of mode B. However, the screech frequency of mode E could not be predicted, indicating that mode E might have a different oscillation behavior.

6.2 Future Considerations

A next step of this work that arises naturally is its extension to two-dimensional and three-dimensional noise source mapping. The extension to two-dimensional sources will require design and implementation of two-dimensional scanning microphone arrays. Some progress has been made in that direction in the recent years [25, 26, 113] with the use of 2-dimensional rotating arrays. Obviously, the extension the continuous-scan phased array setup to two-dimensional source mapping requires careful tracking of the moving sensor(s) and synchronization of the signals. In addition, the geometrical approximations of Eq. 2.17 must be reevaluated. This requires reconsideration of signal division and potential modifications on the optimal block schedule. The same considerations apply to the extension of the methodology to three-dimensional source mappings. Efficient deconvolution algorithms for 3-D inversion must yet be investigated, as calculation of the spatially-variant point spread function might be cumbersome depending on the grid size that is used and DAMAS, R-L and CLEAN-SC could be significantly more expensive.

Another consideration and guidance for future studies relies on the aeroacoustic sources that have been studied. This work has demonstrated that shielding surfaces in the vicinity of a subsonic jet flow might convert hydrodynamic disturbances into acoustic waves that scatter from the trailing edge of a flat plate, provided the plate is sufficiently close to the jet boundary. Additional experiments could be performed using serrated surfaces with the ultimate goal of minimizing such energy transfer.

Finally, a significant contribution of this work has been the study of supersonic jet flows. This work demonstrated that the presence of angled surfaces upstream of the nozzle exit give rise to new tonal components that do not fall into any of the known jet oscillation categories (i.e., mode A1, A2, B, C, or D). The presence of a 60° reflector is particularly important, as it contributes to the appearance of new tones from an unknown mode, categorized in this work as mode E. The oscillation dynamics of mode E remain unknown. There exists a possibility that the mode is an extension of one of the symmetric modes (A1, A2) but additional near-field azimuthal data is required to validate this hypothesis. It could also be possible that the jet was oscillating in a lateral fashion but had more unstable frequencies with the addition of the reflectors. Future studies might explore the oscillation dynamics of mode E and attempt at its complete categorization. To that end, sophisticated tools to separate tonal components such as the Vold-Kalman filter will be required given that mode B and E appear to be coexisting.

The ability of the continuous-scan methods at obtaining orthogonal partial fields could be further exploited. Near-field acoustic experiments might be performed in an attempt to find the partial fields that has to be imposed on a virtual radiating surface. The surface and the partial fields could later be used to generate the acoustic far-field using a Boundary

Element Method (BEM) approach and to compare with distinct source models and far-field experimental data. The continuous-scan approach and the proposed signal processing provides a very high spatial resolution when constructing the partial fields, which will be useful at comparing the modeled and the measured pressure statistics at the radiating surface.

Bibliography

[1] Dimitri Papamoschou, David Morata, and Parthiv Shah. Inverse acoustic methodology for continuous-scan phased arrays. *AIAA Journal*, 57(12):5126–5141, 2019.

[2] Christopher K. Tam, Sarah A. Parrish, and Krishna Viswanathan. The harmonics of jet screech tones. *AIAA Paper 2013-2091*, 2013.

[3] Yoshikuni Umeda and Ryuji Ishii. Sound sources of screech tone radiated from circular supersonic jet oscillating in the helical mode. *International Journal of Aeroacoustics*, 1(4):355–384, 2002.

[4] Daniel Edgington-Mitchell. Aeroacoustic resonance and self-excitation in screeching and impinging supersonic jets – a review. *International Journal of Aeroacoustics*, 18(2-3):118–188, 2019.

[5] Zhihai Xu, Pengzhao Ye, Guangmang Cui, Huajun Feng, Qi Li, and Yueting Chen. Image restoration for large-motion blurred lunar remote sensing image. *Selected Papers of the Chinese Society for Optical Engineering*, 10255:836 – 843, 2017.

[6] M.J. Fisher, M. Harper-Bourne, and S.A.L. Glegg. Jet engine noise source location: The polar correlation technique. *Journal of Sound and Vibration*, 51(1):23 – 54, 1977.

[7] Marianne Mosher. Phased arrays for aeroacoustic testing - theoretical development. 1996.

[8] Jr. William Humphreys, Thomas Brooks, Jr. William Hunter, and Kristine Meadows. Design and use of microphone directional arrays for aeroacoustic measurements. 1998.

[9] Thomas Padois, Olivier Doutres, Franck Sgard, and Alain Berry. Optimization of a spherical microphone array geometry for localizing acoustic sources using the generalized cross-correlation technique. *Mechanical Systems and Signal Processing*, 132:546–559, 2019.

[10] Elias J.G. Arcondoulis, Yu Liu, Pengwei Xu, and Nanshu Chen. Application of the adaptive array reduction method for offset acoustic source localisation. *Journal of Sound and Vibration*, 478:115358, 2020.

[11] Xi Chen, Chao Pan, Jingdong Chen, and Jacob Benesty. Planar array geometry optimization for region sound acquisition. *ICASSP 2021 - 2021 IEEE International Conference on Acoustics, Speech and Signal Processing (ICASSP)*, pages 756–760, 2021.

[12] Thomas Brooks and William Humphreys. A deconvolution approach for the mapping of acoustic sources (damas) determined from phased microphone arrays. *AIAA Paper 2004-2954*, 2004.

[13] Robert Dougherty. Extensions of damas and benefits and limitations of deconvolution in beamforming. *AIAA Paper 2005-2961*, 2005.

[14] Pieter Sijtsma. Clean based on spatial source coherence. *International Journal of Aeroacoustics*, 6(4):357–374, 2007.

[15] William Hadley Richardson. Bayesian-based iterative method of image restoration. *J. Opt. Soc. Am.*, 62(1):55–59, Jan 1972.

[16] L.B. Lucy. An iterative technique for the rectification of observed distributions. *Astronomical Journal*, 79:745, 1974.

[17] D. Papamoschou. Imaging of distributed directional noise sources. *Journal of Sound and Vibration*, 330(10):2265–2280, 2011.

[18] D.F. Shanno and K.H. Phua. Minimization of Unconstrained Multivariate Functions. *ACM Transactions on Mathematical Software*, pages 618–622, 1976.

[19] Q. Leclère, A. Pereira, C. Bailly, J. Antoni, and C. Picard. A unified formalism for acoustic imaging based on microphone array measurements. *International Journal of Aeroacoustics*, 16(4-5):431–456, 2017.

[20] A. Pereira, J. Antoni, and Q. Leclère. Empirical Bayesian regularization of the inverse acoustic problem. *Applied Acoustics*, 97:11–29, 2015.

[21] Moohyung Lee and J. Stuart Bolton. Source characterization of a subsonic jet by using near-field acoustical holography. *The Journal of the Acoustical Society of America*, 121(2):967–977, 2007.

[22] François Nicolas and Maxime Rey. S1mawind tunnel new aeroacoustic capability: a traversing microphone array. *AIAA Paper 2018-3137*, 2018.

[23] Havard Vold, Parthiv Shah, Joshua Davis, Paul Bremner, Dennis McLaughlin, Philip Morris, Jeremy Veltin, and Richard McKinley. High resolution continuous scan acoustical holography applied to high-speed jet noise. *AIAA Paper 2010-3754*, 2010.

[24] Parthiv Shah, Havard Vold, and Michael Yang. Reconstruction of Far-Field Noise Using Multireference Acoustical Holography Measurements of High-Speed Jets. Technical report, AIAA Paper, 2011.

[25] Parthiv N. Shah, Andrew White, Dan Hensley, Dimitri Papamoschou, and Håvard Vold. Continuous-Scan Phased Array Measurement Methods for Turbofan Engine Acoustic Testing. *Journal of Engineering for Gas Turbines and Power*, 141(8), 02 2019.

[26] Parthiv N. Shah and Dimitri Papamoschou. Characterization of high speed jet acoustics using high-resolution multi-reference continuous-scan acoustic measurements on a linear array. *AIAA Paper 2020-0005*, 2020.

[27] David Morata and Dimitri Papamoschou. Advances in the direct spectral estimation of aeroacoustic sources using continuous-scan phased arrays. *AIAA Paper 2021-0215*, 2021.

[28] David Morata and Dimitri Papamoschou. Extension of traditional beamforming methods to the continuous-scan paradigm. *AIAA Paper 2022-1154*.

[29] Christopher K. W. Tam, K. Viswanathan, K. K. Ahuja, and J. Panda. The sources of jet noise: experimental evidence. *Journal of Fluid Mechanics*, 615:253–292, 2008.

[30] K. VISWANATHAN. Aeroacoustics of hot jets. *Journal of Fluid Mechanics*, 516:39–82, 2004.

[31] C K W Tam. Supersonic jet noise. *Annual Review of Fluid Mechanics*, 27(1):17–43, 1995.

[32] Dimitri Papamoschou. Wavepacket modeling of the jet noise source. *International Journal of Aeroacoustics*, 17(1-2):52–69, 2018.

[33] Michael James Lighthill and Maxwell Herman Alexander Newman. On sound generated aerodynamically i. general theory. *Proceedings of the Royal Society of London. Series A. Mathematical and Physical Sciences*, 211(1107):564–587, 1952.

[34] D. Papamoschou. Imaging of directional distributed noise sources. *Journal of Sound and Vibration*, 330(10):2265–2280, 2011.

[35] Alan Powell. The noise of choked jets. *The Journal of the Acoustical Society of America*, 25(3):385–389, 1953.

[36] Daniel Edgington-Mitchell, Joel Weightman, Samuel Lock, Rhiannon Kirby, Vineeth Nair, Julio Soria, and Damon Honnery. The generation of screech tones by shock leakage. *Journal of Fluid Mechanics*, 908, 2020.

[37] Ganesh Raman. Advances in Understanding Supersonic Jet Screech : Review and Perspective. *Progress in Aerospace Sciences*, 34(1-2):45–106, 1998.

[38] Alan Powell. On the mechanism of choked jet noise. *Proceedings of the Physical Society. Section B*, 66(12):1039–1056, 1953.

[39] Alan Powell. The noise of choked jets. *The Journal of the Acoustical Society of America*, 25(3):385–389, 1953.

[40] Michael James Lighthill. On sound generated aerodynamically ii. turbulence as a source of sound. *Proceedings of the Royal Society of London. Series A. Mathematical and Physical Sciences*, 222(1148):1–32, 1954.

[41] J. E. Ffowcs Williams and Michael James Lighthill. The noise from turbulence convected at high speed. *Philosophical Transactions of the Royal Society of London. Series A, Mathematical and Physical Sciences*, 255(1061):469–503, 1963.

[42] Victor Chobotov and Allan Powell. On the prediction of acoustic environments from rockets. *Rama-Wooldridge Corporate Report EM-7-7*, 1957.

[43] Max Kandula and Bruce Vu. On the scaling laws for jet noise in subsonic and supersonic flow. *AIAA Paper 2003-3288*, 2003.

[44] K. Viswanathan. Mechanisms of jet noise generation: Classical theories and recent developments. *International Journal of Aeroacoustics*, 8(4):355–407, 2009.

[45] Christopher K. W. Tam and K. K. Ahuja. Theoretical model of discrete tone generation by impinging jets. *Journal of Fluid Mechanics*, 214:67–87, 1990.

[46] Daniel Edgington-Mitchell, Tianye Wang, Petronio Nogueira, Oliver Schmidt, Vincent Jaunet, Daniel Duke, Peter Jordan, and Aaron Towne. Waves in screeching jets. *Journal of Fluid Mechanics*, 913:A7, 2021.

[47] J. Panda, G. Raman, K. Zaman, J. Panda, G. Raman, and K. Zaman. Underexpanded screeching jets from circular, rectangular and elliptic nozzles. *AIAA Paper 1997-1623*, 1997.

[48] Christopher K. W. Tam and Fang Q. Hu. On the three families of instability waves of high-speed jets. *Journal of Fluid Mechanics*, 201:447–483, 1989.

[49] Oliver T. Schmidt, Aaron Towne, Tim Colonius, André V. G. Cavalieri, Peter Jordan, and Guillaume A. Brès. Wavepackets and trapped acoustic modes in a turbulent jet: coherent structure eduction and global stability. *Journal of Fluid Mechanics*, 825:1153–1181, 2017.

[50] Hao Shen and Christopher K. W. Tam. Three-dimensional numerical simulation of the jet screech phenomenon. *AIAA Journal*, 40(1):33–41, 2002.

[51] Patricio Ravetta, Ricardo Burdisso, and Wing Ng. Noise source localization and optimization of phased array results (lore). *AIAA Paper 2006-2713*, 2006.

[52] Blaine M. Harker, Kent L. Gee, Tracianne B. Neilsen, Alan T. Wall, and Michael M. James. Beamforming-based wavepacket model for noise environment predictions of tactical aircraft. *AIAA Paper 2017-4048*, 2017.

[53] R.K. Amiet. Refraction of sound by a shear layer. *Journal of Sound and Vibration*, 58(4):467–482, 1978.

[54] Jorgen Hald. Cross-spectral matrix diagonal reconstruction. *Inter-Noise and Noise-Con Conference*, 253(5):3766–3777, 2016.

[55] Robert Dougherty. Cross-spectral matrix diagonal optimization. *Berlin Beamforming Conference (BeBeC)*, 2016.

[56] Michael Grant and Stephen Boyd. Graph implementations for nonsmooth convex programs. In V. Blondel, S. Boyd, and H. Kimura, editors, *Recent Advances in Learning and Control*, Lecture Notes in Control and Information Sciences, pages 95–110. Springer-Verlag Limited, 2008. `http://stanford.edu/~boyd/graph_dcp.html`.

[57] Michael Grant and Stephen Boyd. CVX: Matlab software for disciplined convex programming, version 2.1. `http://cvxr.com/cvx`, March 2014.

[58] Colin VanDercreek, Roberto Merino-Martínez, Pieter Sijtsma, and Mirjam Snellen. Evaluation of the effect of microphone cavity geometries on acoustic imaging in wind tunnels. *Applied Acoustics*, 181:108154, 2021.

[59] Thomas Ahlefeldt. Microphone array measurement in european transonic wind tunnel at flight reynolds numbers. *AIAA Journal*, 55(1):36–48, 2017.

[60] C. S. Allen, W. K. Blake, R. P. Dougherty, D. Lynch, and P. T. Soderman. *Aeroacoustic Measurements*. Springer, 2002.

[61] Jingjing Yu and Kevin D. Donohue. Optimal irregular microphone distributions with enhanced beamforming performance in immersive environments. *The Journal of the Acoustical Society of America*, 134(3):2066–2077, 2013.

[62] Miloš Bjelić, Miodrag Stanojević, Dragana Šumarac Pavlović, and Miomir Mijić. Microphone array geometry optimization for traffic noise analysis. *The Journal of the Acoustical Society of America*, 141(5):3101–3104, 2017.

[63] Thomas F. Brooks and William M. Humphreys. A deconvolution approach for the mapping of acoustic sources (damas) determined from phased microphone arrays. *Journal of Sound and Vibration*, 294(4):856 – 879, 2006.

[64] Elisabet Tiana-Roig and Finn Jacobsen. Deconvolution for the localization of sound sources using a circular microphone array. *The Journal of the Acoustical Society of America*, 134(3):2078–2089, 2013.

[65] J.L. Starck, E. Pantin, and F. Murtagh. Deconvolution in astronomy: A review. *Publications of the Astronomical Society of the Pacific*, 144(800), 2002.

[66] David B. Stephens and Håvard Vold. Order tracking signal processing for open rotor acoustics. *Journal of Sound and Vibration*, 333(16):3818 – 3830, 2014.

[67] Liang Yu, Jerome Antoni, and Quentin Leclere. Spectral matrix completion by cyclic projection and application to sound source reconstruction from non-synchronous measurements. *Journal of Sound and Vibration*, 372:31–49, 2016.

[68] Caleb B. Goates, Blaine M. Harker, Tracianne B. Neilsen, and Kent L. Gee. Extending the bandwidth of an acoustic beamforming array esing phase unwrapping and array interpolation. *The Journal of the Acoustical Society of America*, 141(4):407–412, 2017.

[69] Gerhard Doblinger. Beamforming with optimized interpolated microphone arrays. *IEEE Hands-Free Speech Communication and Microphone Arrays*, pages 33–36, 2008.

[70] D.N. Swingler and R.S. Walker. Line-array beamforming using linear prediction for aperture interpolation and extrapolation. *IEEE Transactions on Acoustics, Speech, and Signal Processing*, 37(1):16–30, 1989.

[71] Liang Yu, Jerome Antoni, Haijun Wu, Quentin Leclere, and Weikang Jiang. Fast iteration algorithms for implementing the acoustic beamforming of non-synchronous measurements. *Mechanical Systems and Signal Processing*, 134:106309, 2019.

[72] Liang Yu, Qixin Guo, Ning Chu, and Rui Wang. Achieving 3d beamforming by non-synchronous microphone array measurements. *Sensors*, 20(24), 2020.

[73] Fangli Ning, Jiahao Song, Jinglong Hu, and Juan Wei. Sound source localization of non-synchronous measurements beamforming with block hermitian matrix completion. *Mechanical Systems and Signal Processing*, 147:107118, 2021.

[74] Dingyu Hu, Jinjin Ding, Han Zhao, and Liang Yu. Spatial basis interpretation for implementing the acoustic imaging of non-synchronous measurements. *Applied Acoustics*, 182:108198, 2021.

[75] Lourenço Tércio Lima Pereira, Roberto Merino-Martínez, Daniele Ragni, David Gómez-Ariza, and Mirjam Snellen. Combining asynchronous microphone array measurements for enhanced acoustic imaging and volumetric source mapping. *Applied Acoustics*, 182:108247, 2021.

[76] Q. Leclère. Multi-channel spectral analysis of multi-pass acquisition measurements. *Mechanical Systems and Signal Processing*, 23(5):1415–1422, 2009.

[77] Liang Yu, Jerome Antoni, Quentin Leclere, and Weikang Jiang. Acoustical source reconstruction from non-synchronous sequential measurements by fast iterative shrinkage thresholding algorithm. *Journal of Sound and Vibration*, 408:351–367, 2017.

[78] Kyoung-Uk Nam and Yang-Hann Kim. A partial field decomposition algorithm and its examples for near-field acoustic holography. *The Journal of the Acoustical Society of America*, 116(1):172–185, 2004.

[79] Moohyung Lee and J. Stuart Bolton. Scan-based near-field acoustical holography and partial field decomposition in the presence of noise and source level variation. *The Journal of the Acoustical Society of America*, 119(1):382–393, 2006.

[80] David Morata, Kyle A. Miller, and Dimitri Papamoschou. Experimental study of underexpanded screeching jet and its interaction with upstream reflector. *AIAA Paper 2022-2868.*

[81] Salil Luesutthiviboon, Anwar MN Malgoezar, Roberto Merino-Martinez, Mirjam Snellen, Pieter Sijtsma, and Dick G Simons. Enhanced hr-clean-sc for resolving multiple closely spaced sound sources. *International Journal of Aeroacoustics*, 18(4-5):392–413, 2019.

[82] Leandro de Santana. Fundamentals of acoustic beamforming. *NATO Educational Notes EN-AVT-287-04*, 2017.

[83] Klaus Ehrenfried and Lars Koop. Comparison of iterative deconvolution algorithms for the mapping of acoustic sources. *AIAA Journal*, 45(7):1584–1595, 2007.

[84] S.M. Anisheh and H. Hassanpour. Designing an adaptive approach for segmenting non-stationary signals. *International Journal of Electronics*, 98(8):1091–1102, 2011.

[85] R. Agarwal and J. Gotman. Adaptive segmentation of electroencephalographic data using a nonlinear energy operator. *1999 IEEE International Symposium on Circuits and Systems (ISCAS)*, 1999.

[86] D. Wang, R. Vogt, M. Mason, and S. Sridharan. Automatic audio segmentation using the generalized likelihood ratio. *2008 2nd International Conference on Signal Processing and Communication Systems*, 2008.

[87] Pierre Lanchantin, Jérôme Lapuyade-Lahorgue, and Wojciech Pieczynski. Unsupervised segmentation of randomly switching data hidden with non-gaussian correlated noise. *Signal Processing*, 91(2):163–175, 2011.

[88] Hamed Azami, Hamid Hassanpour, Javier Escudero, and Saeid Sanei. An intelligent approach for variable size segmentation of non-stationary signals. *Journal of Advanced Research*, 6(5):687–698, 2015.

[89] Hamed Azami, Saeid Sanei, Karim Mohammadi, and Hamid Hassanpour. A hybrid evolutionary approach to segmentation of non-stationary signals. *Digital Signal Processing*, 23(4):1103–1114, 2013.

[90] Carl Gerhold, Lorenzo Clark, Mark Dunn, and John Tweed. Investigation of acoustical shielding by a wedge-shaped airframe. *Journal of Sound and Vibration*, 294:49–63, 2006.

[91] D. Papamoschou and S. Rostamimonjezi. Effect of velocity ratio on noise source distribution of coaxial jets. *AIAA Journal*, 48(7):1504–1512, 2010.

[92] Nick P. Breen and Krishan K. Ahuja. Limitations of acoustic beamforming for accurate jet noise source location. *AIAA Paper 2020-2603*, 2020.

[93] CHRISTOPHER K. W. Tam, K. Viswanathan, K. K. Ahuja, and J. Panda. The sources of jet noise: experimental evidence. *Journal of Fluid Mechanics*, 615:253–292, 2008.

[94] Garry L. Brown and Anatol Roshko. On density effects and large structure in turbulent mixing layers. *Journal of Fluid Mechanics*, 64(4):775–816, 1974.

[95] Christophe Bogey and Christophe Bailly. Investigation of subsonic jet noise using les: Mach and reynolds number effects. *AIAA Paper 2004-3023*, 2004.

[96] Gary Podboy. Jet-surface interaction test: Phased array noise source localization results. *Proceedings of the ASME Turbo Expo*, 1, 06 2012.

[97] Ganesh Raman. Cessation of screech in underexpanded jets. *Journal of Fluid Mechanics*, 336:69–90, 1997.

[98] Md. Tawhidul Khan Islam and Kunisato Seto. Control of supersonic jet noise with a spherical reflector. *The Journal of the Acoustical Society of America*, 116(4):2539–2540, 2004.

[99] John M. Seiner, James C. Manning, and Michael K. Ponton. Dynamic pressure loads associated with twin supersonic plume resonance. *AIAA Journal*, 26(8):954–960, 1988.

[100] T. D. Norum. Screech suppression in supersonic jets. *AIAA Journal*, 21(2):235–240, 1983.

[101] David Morata and Dimitri Papamoschou. Effect of nozzle geometry on the space-time emission of screech tones. *AIAA Paper 2021-2306*, 2021.

[102] Alan Powell, Yoshikuni Umeda, and Ryuji Ishii. Observations of the oscillation modes of choked circular jets. *The Journal of the Acoustical Society of America*, 92(5):2823–2836, 1992.

[103] Bertrand Mercier, Thomas Castelain, and Christophe Bailly. Experimental characterisation of the screech feedback loop in underexpanded round jets. *Journal of Fluid Mechanics*, 824:202–229, 2017.

[104] C.K.W. Tam, J.M. Seiner, and J.C. Yu. Proposed relationship between broadband shock associated noise and screech tones. *Journal of Sound and Vibration*, 110(2):309–321, 1986.

[105] Xiang-Ru Li, Xi-Wen Zhang, Peng-Fei Hao, and Feng He. Acoustic feedback loops for screech tones of underexpanded free round jets at different modes. *Journal of Fluid Mechanics*, 902, 2020.

[106] Romain Gojon and Christophe Bogey. Numerical study of th flow and the near acoustic fields of an underexpanded round free jet generating two screech tones. *International Journal of Aeroacoustics*, 16(7-8):603–625, 2017.

[107] Romain Gojon, Ephraim Gutmark, and Mihai Mihaescu. Antisymmetric oscillation modes in rectangular screeching jets. *AIAA Journal*, 57(8):3422–3441, 2019.

[108] Surya Chakrabarti, Datta Gaitonde, and S. Unnikrishnan. Representing rectangular jet dynamics through azimuthal fourier modes. *Phys. Rev. Fluids*, 6:074605, 2021.

[109] Surya Chakrabarti, Datta V. Gaitonde, and S. Unnikrishnan. Wavepacket dynamics in rectangular jets. *AIAA Paper 2022-2403*, 2022.

[110] J. H. Gao and X. D. Li. A multi-mode screech frequency prediction formula for circular supersonic jets. *The Journal of the Acoustical Society of America*, 127(3):1251–1257, 2010.

[111] Thomas Castelain, Romain Gojon, Bertrand Mercier, and Christophe Bogey. Estimation of convection speed in underexpanded jets from schlieren pictures. *AIAA Paper 2016-2984*, 2016.

[112] A. Singh and A. Chaterjee. Numerical prediction of supersonic jet screech frequency. *Shock Waves*, 17:263–272, 2007.

[113] Abe Lee, Parthiv Shah, Andrew White, Dan Hensley, and Laura Schweizer. Continuous-scan beamforming for identification of highly varying amplitude sources with low sensor budgets. *Berlin Beamforming Conference (BeBeC-2020-S10*, 2020.